POLITECNICO DI TORINO

M.Sc. in Electronic Engineering

Master’s thesis

Microwave shielding effectiveness study of composite materials and coating based on MWGNP and biochar

Advisors:
Prof. Patrizia Savi
Prof. Paolo Gronchi

Candidate:
Damiano Cirielli

Academic Year 2018-2019

Summary

In this thesis work the shielding properties of composite materials are studied in the C and X bands. An examination of all the methods developed for measuring the shielding effectiveness of materials was primarily done. The purpose was to choose the best method for measuring the shielding effectiveness of two different composites: epoxy resin-based composites with biochar, and graphene nanoplates (GNP) with polyaniline. This latter was used for the deposition of conductive coating on epoxy resin specimens. The purpose of the conducted study is to know if these materials could be used as efficient electromagnetic field instead of metallic shields.

The rectangular waveguide was chosen to be the most suitable test fixture for the shielding effectiveness measurement of all the realized composites. Measurements were carried out with an Agilent programmable network analyzer (PNA) and two waveguide calibration kits: a WR90 (X band) kit and a WR137 (C band) calibration kit.

A procedure is described for the preparation of the specimens, whose physical dimensions fits the inner walls of the used waveguides with a 6.6% maximum tolerance.

The dispersion of biochar in epoxy resin was obtained with a novel method based on a mechanical paddles mixer, driven by an unipolar stepper motor. The realization and the design of the electric circuit, controlling the stepper motor, are also detailed.

Epoxy resin composites were realized with different biochar types; the highest measured shielding effectiveness value was $6\ \mathrm{dB}$. A very similar result was obtained with the tested coating polyaniline composites, whose maximum shielding effectiveness was measured to be $5\ \mathrm{dB}$. Since an electromagnetic shield must exhibit a shielding effectiveness of at least $30\ \mathrm{dB}$, all the composites cannot be used as efficient shields, instead of metals, in the measured frequency range.

However, all the measured specimens show an increasing shielding effectiveness with decreasing frequency; hence it is advisable to measure this figure of merit for frequencies lower than the minimum measured frequency, which is $5.38\ \mathrm{GHz}$.

This thesis is organized as follows: in Chapter 1 the shielding effectiveness definition and the basic concepts of the electromagnetic field shielding are described, since they are often recalled in the Chapter 2, where all the most important shielding effectiveness measurement methods are reported. The tested materials are described in Chapter 3, where the specimens realization procedures are also are detailed. The realized measurement setups are described in Chapter 4, together with the shielding effectiveness of the tested composites. Finally, in Chapter 5, the conclusions about the presented work are reported, and also its future developments.

List of figures

List of tables

Contents

Chapter 1

Electromagnetic field shielding

The electric circuit of any electronic device, especially the ones including for instance oscillators, switches and motors, radiates an electromagnetic field. The density of this radiation can be high enough to cause mal-functioning to other parts of the same device, or to other nearby electronic circuits. To avoid these problems there are specific regulations, that fixes the limit of the electromagnetic field maximum value any device can radiate. When an electronic circuit is not compliant with these regulations, the density of the radiated field can be reduced with some techniques implemented on the printed circuit board (PCB) design, using a proper components and traces disposition. If those techniques are not enough to properly reduce the radiated disturbances, the only solution is the use of a shield.

According to the technical literature, an electromagnetic shield is a metallic box that completely (or partly) encloses the electric circuit of an electronic device.

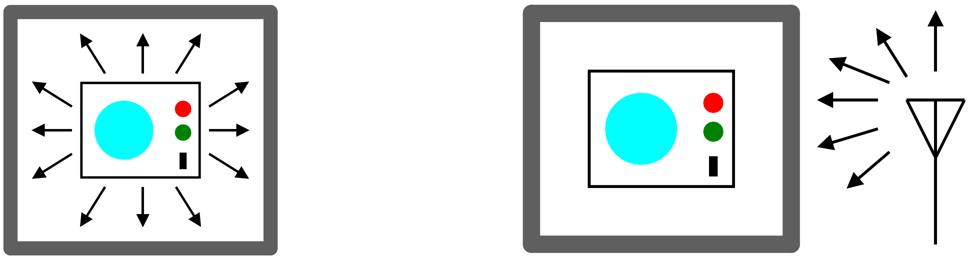

(a)

(b)

Figure 1.1: Electromagnetic waves (black arrows) shielded by a metallic enclosure (grey box) (a); the enclosure shields the electromagnetic waves the antenna radiates (b).

In Figure 1.1 (a) is represented the case of a metallic enclosure that confines the electromagnetic waves radiated by a generic electronic circuit. The Figure 1.1 (b), instead, shows the case of an electric circuit protected against the electromagnetic field radiated by another near device, here simulated with a transmitting antenna.

The best choice for a shield is a metal, having conductivity and thickness properly designed, as discussed in this chapter. However, the literature shows a rich research of other materials having shielding properties quite similar than (or eventually better than) metals. Some examples are textiles and composites materials, containing substances with the property to absorb the electromagnetic waves. Some of these materials are presented in chapter 0. The capability of any new material to shield the electromagnetic waves is measured, in order to classify them and to allow the user the best choice for any application. In particular, the efficiency of an enclosure to shield the electromagnetic waves, is measured in terms of *shielding effectiveness* (SE).

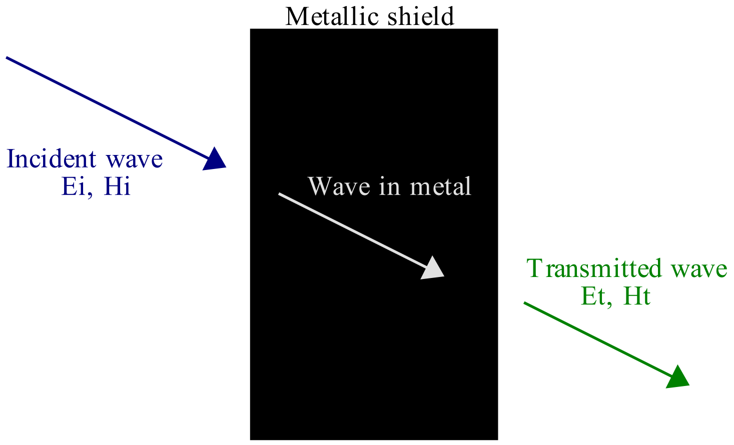

Figure 1.2: Example of the path of an electromagnetic wave ray through a metallic shield.

A general definition of the shielding effectiveness can be done with the aid of Figure 1.2, where an example of an electromagnetic field impinging a metallic shield (black rectangle) is illustrated. If the electric field only is considered, the wave impinging the shield is denoted as E_i, while the (unwanted) field transmitted through the shield is called E_t. If it is possible to measure both fields magnitude, the shielding effectiveness SE is defined as:

$$\mathrm{SE} = \frac{\text{electric field magnitude } \textit{incident} \text{ to the shield}}{\text{electric field magnitude } \textit{transmitted through} \text{ the shield}} \tag{1.1}$$

Another definition states that the shielding effectiveness is:

$$\mathrm{SE} = \frac{\text{electric field magnitude } \textit{withouth} \text{ the shield}}{\text{elecrtic field magnitude } \textit{with} \text{ the shield}} \tag{1.2}$$

In this case the shielding effectiveness is considered to be an insertion loss.
With the notation adopted in Figure 1.2, the electric field shielding effectiveness is:

$$SE_E = \left|\frac{E_i}{E_t}\right| \tag{1.3}$$

which is usually expressed in decibels:

$$SE_{E|dB} = 20Log\left|\frac{E_i}{E_t}\right| \tag{1.4}$$

The same definitions apply for the magnetic field:

$$SE_H = \left|\frac{H_i}{H_t}\right| \tag{1.5}$$

$$SE_{H|dB} = 20Log\left|\frac{H_i}{H_t}\right| \tag{1.6}$$

A third definition involves the ratio between the incident power of the electromagnetic field, P_i, and the transmitted power, P_t:

$$SE_p = \left|\frac{P_i}{P_t}\right| \tag{1.7}$$

$$SE_{p|dB} = 10Log\left|\frac{P_i}{P_t}\right| \tag{1.8}$$

The purpose of this chapter is to recall the principal definitions and concepts related to the shielding effectiveness; for this reason, the presented dissertation is not complete, because only approximate solutions are described for the shielding effectiveness computation of metallic plates. A more complete description including exact solutions can be found in [1].

1.1 Shielding of far-field electromagnetic sources

The incident wave illustrated in Figure 1.2 is considered to be the propagation direction of a plane wave, generated by a far-field source. This case is highlighted in Figure 1.3, where the impinging wave propagates along the z axes direction $\left(\widehat{\mathrm{k}_0} \parallel \hat{\mathrm{z}}\right)$ and the metallic shield has thickness th. The incident wave path is compared to an electromagnetic wave propagating into a transmission line: air is the principal media in which the wave propagates, and the metallic shield represents a discontinuity. In particular, the air-to-metal interface at the $\mathrm{z} = 0$ coordinate is the first discontinuity, generating a propagation media impedance mismatch. Due to this discontinuity, part of the electromagnetic field is transmitted inside the metal, (E_1, H_1), while the remaining part is reflected backward, generating the field E_r, H_r. The transmitted field is then partly propagating beyond the second discontinuity, located at $z = th$ interface (E_t, H_t), and partly reflected inside the shield itself, generating the field E_2, H_2.

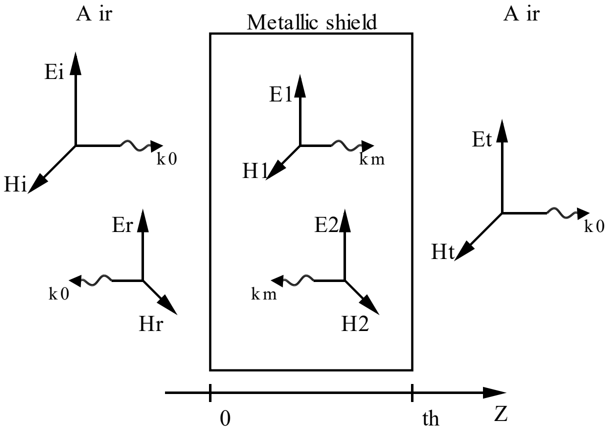

Figure 1.3: Propagation of a plane wave through a metallic shield.

In this analyzed case were done the following assumptions:

- The incident wave is a perfect plane wave, propagating in air; as an approximation, this media is considered like vacuum, with propagation constant k_0 and wave impedance Z_∞:

$$k_0 = \omega\sqrt{\mu_0 \cdot \epsilon_0} \tag{1.9}$$

$$Z_\infty = \sqrt{\frac{\mu_0}{\epsilon_0}} \tag{1.10}$$

- The wave vector k_m of the metallic shield (supposed to be homogeneous) and the wave impedance $Z_{\infty m}$ are:

$$k_m = \alpha_m + j\beta_m = \sqrt{j\omega\mu(\sigma + j\omega\epsilon)} \tag{1.11}$$

$$Z_{\infty m} = \sqrt{\frac{j\omega\mu}{\sigma + j\omega\epsilon}} \tag{1.12}$$

Where β_m is the metal propagation constant and $(\sigma + j\omega\epsilon)$ is its complex conductivity.
The electric field inside the metal, at the $z = 0^+$ coordinate, after the media mismatch, is [1]:

$$E_1|_{z=0^+} = 2E_i \frac{Z_{\infty m}}{Z_{\infty m} + Z_{\infty}} \tag{1.13}$$

at $z = \mathrm{th}^-$ coordinate it becomes:

$$E_1|_{z=th^-} = E_1 e^{-(\alpha+j\beta)z} = \ E_1 e^{-\alpha th} e^{-j\beta th} \tag{1.14}$$

Outside the metal, for $z = \mathrm{th}^+$, the electric field reads:

$$E_t = 2E_1|_{z=th^-} \frac{Z_{\infty}}{Z_{\infty} + Z_{\infty m}} \tag{1.15}$$

The transmitted field E_t can be related to the incident field E_i substituting the equation (1.15) in the (1.14); the obtained result must be than substituted in the (1.13) equation, considering $E_1 = E_1|_{z=0^+}$:

$$E_t = 4E_i \frac{Z_{\infty m} Z_{\infty a}}{(Z_{\infty m} + Z_{\infty a})^2} e^{-(\alpha+j\beta)th} \tag{1.16}$$

Since the definition (1.4) involves the ratio E_i/E_t, it was computed from (1.16):

$$\frac{E_i}{E_t} = \frac{(Z_{\infty m} + Z_{\infty})^2}{4 \cdot Z_{\infty m} \cdot Z_{\infty}} e^{(\alpha+j\beta)th} \tag{1.17}$$

The general expression (1.17) can be simplified introducing some considerations about the physic characteristics of the two propagation media in Figure 1.3.
Firstly, in a metal, the permittivity is smaller than conductivity, and this implies that:

$$\sigma \gg \omega\epsilon \tag{1.18}$$

The wave impedance $Z_{\infty m}$ (1.12) and the propagation constant k_m (1.11) could be simplified as follows:

$$Z_{\infty m} = \sqrt{\frac{j\omega\mu}{\sigma + j\omega\epsilon}} \ \simeq \sqrt{j\frac{\omega\mu}{\sigma}} \tag{1.19}$$

$$k_m = \sqrt{j\omega\mu(\sigma + j\omega\epsilon)} \ \simeq \ \sqrt{j\omega\mu\sigma} \tag{1.20}$$

hence:

$$Z_{\infty m} \ll Z_{\infty} \tag{1.21}$$

$$\alpha_m = \beta_m = \frac{1}{\delta} = \sqrt{\pi f \mu \sigma} \tag{1.22}$$

where:

$$\delta = \frac{1}{\sqrt{\pi f \mu \sigma}} \tag{1.23}$$

is the skin depth penetration.

The equation (1.17) can be now simplified considering the (1.21) and (1.23) relationships, obtaining the (1.24):

$$SE_{dB} = 20Log\left|\frac{Z_{\infty}}{4Z_{\infty m}}\right| + 20Log\ e^{th/\delta} \tag{1.24}$$

The ratio $\mathrm{Z}_{\infty}/(4\mathrm{Z}_{\infty\mathrm{m}})$ represents the impedance mismatch between the air and the metallic shield surface, hence the quantity of the incident field reflected in z=0 coordinate (E_r, H_r). For this reason, the first addendum of (1.24) expression is called Reflection Loss (R_{dB})

$$R_{dB} = 20Log\left|\frac{Z_{\infty}}{4Z_{\infty m}}\right| \tag{1.25}$$

Since the metal wave impedance is much smaller than the vacuum characteristic impedance (1.21), the reflection loss term shows that only a very small quantity of the electric field is transmitter through the shield.

The second term of (1.24) describes the propagation of the plane wave inside the metallic shield; since a shield is used to reduce the magnitude of the electromagnetic filed, the second addendum is a measure of the absorption loss (A_{dB}) of the shield itself:

$$A_{dB} = 20Log\ e^{th/\delta} \tag{1.26}$$

which can be simplified using the logarithm properties:

$$A_{dB} = \frac{th}{\delta} 20Log\ e \simeq 8.686\frac{th}{\delta} \tag{1.27}$$

In this way the importance of the shield thickness against the skin depth is highlighted: it is strongly advisable to have a metallic shield whose thickness is greater than its skin depth penetration.

Referring to the Figure 1.3, the electromagnetic field $\mathrm{E_2}$, $\mathrm{H_2}$ represents only the first reflection of the transmitted field $\mathrm{E_1}$, $\mathrm{H_1}$; in reality, multiple reflections are generated between the two shield walls, until the electromagnetic field is almost entirely attenuated. Usually, no more than ten reflections are considered. The expression of the attenuation due to multiple reflections inside the shield is called $\mathrm{M_{dB}}$ [1]:

$$M_{dB} = 20Log(1 - e^{-2t/\delta}) \tag{1.28}$$

It is usual to write the shielding effectiveness as the sum of the reflection loss, the absorption loss and the multiple reflections contributions, obtaining the well-known equation:

$$SE_{dB} = R_{dB} + A_{dB} + M_{dB} \tag{1.29}$$

The magnetic field sheilding effectiveness is now computed, starting from the reflection loss. Recalling the impedance relationship between electric field ($\mathrm{E_{me}}$) and magnetic field ($\mathrm{H_{me}}$) propagating in a generic media “me” with wave impedance $\mathrm{Z_{\infty,me}}$:

$$E_{me} = H_{me} \cdot Z_{\infty,me} \tag{1.30}$$

from the ratio $\mathrm{E_1/E_i}$, computed with the equation (1.13), the ratio $\mathrm{H_1/H_i}$ can be found:

$$\frac{H_1}{H_i} = \frac{2Z_\infty}{Z_\infty + Z_{\infty m}} \tag{1.31}$$

similarly, from the (1.15) equation, the ratio $\mathrm{H_t/H_1}$ results:

$$\frac{H_t}{H_1} = \frac{2Z_{\infty m}}{Z_\infty + Z_{\infty m}} \tag{1.32}$$

Dividing the (1.32) by the (1.31), the ratio between the transmitted magnetic field and the incident field is computed:

$$\frac{H_t}{H_i} = \frac{4Z_\infty Z_{\infty m}}{(Z_\infty + Z_{\infty m})^2} \tag{1.33}$$

Recalling the expression (1.21), the approximate reflection loss term becomes:

$$R_{dB} = 20Log\left|\frac{4Z_{\infty m}}{Z_{\infty}}\right| \tag{1.34}$$

This expression shows that the magnetic field tends to penetrate the shield, since the ratio $Z_{\infty m}/Z_{\infty}$ is a very small quantity. Hence the magnetic field shielding is principally due to the absorption loss and the multiple reflections, whose analytic expressions are identical to the ones already computed for the electric field.

From the theoretical analysis of the shielding effectiveness, some general considerations can be done about the material to be choose as shield:

- The shielding of electric field is primarily due to the impedance mismatch between the shield and the media in which the wave propagates: to have the maximum impedance mismatch, the shield wave impedance must be the highest possible. Recalling the expression (1.12), an high value of σ_r must be preferred for a metallic shield.
- The shielding of magnetic field is principally due to the absorption mechanism, hence the shield thickness must be greater than its skin depth penetration. In order to avoid the realization of very thick shields, referring to (1.23), a material having low skin depth penetration must be chosen, hence high σ_r and high μ_r.

The frequency dependence of the terms in equation (1.29) is showed in Figure 1.4, where the electric field shielding effectiveness measurements of a $1\ \mathrm{mm}$ thick copper plate are reported. Here the dashed blue line is computed as the sum of the reflection loss, the absorption loss and the multiple reflection loss. It can be notice that, for low frequencies, the reflection loss dominates, so the total shielding effectiveness is primarily due to the impedance mismatch between the air and the shield. For frequencies between 1 kHz and 1 MHz the incident wave in Figure 1.3 tends to penetrate the shield, hence the multiple reflection loss term is the major contribution to the shielding effectiveness. If the frequency is higher than 1 MHz the absorption loss term becomes comparable to the multiple reflection contribution, since the skin depth penetration is reduced.

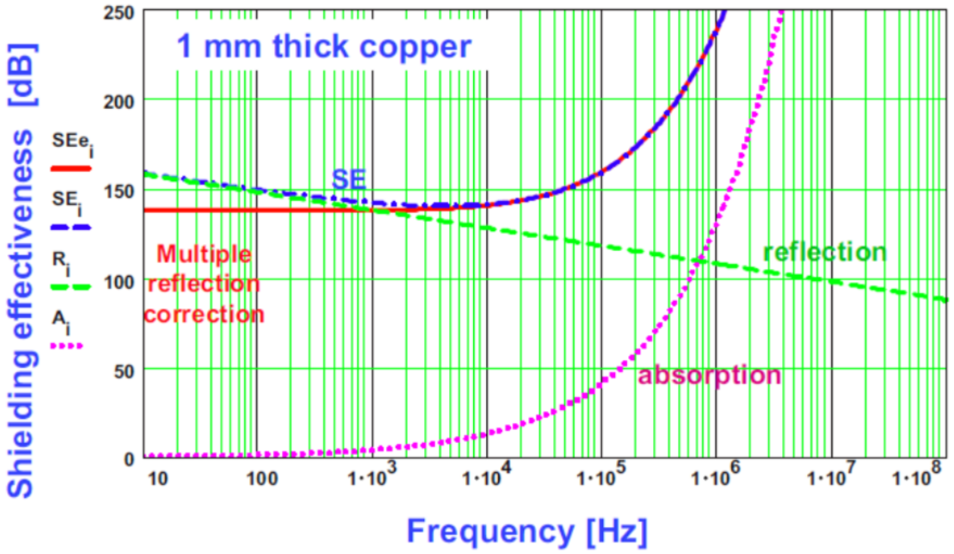

Figure 1.4: Decomposition of the shielding effectiveness of a copper plate, according to the equation (1.29). Plot taken from [2].

If the frequency (or the frequency band) of the field to be shielded is known, the shield material can be chosen as follows:

- For low frequencies, such that the shield thickness is lower than the skin depth, the shielding effectiveness is primarily due to the reflection mismatch between the air and the metal. According to the reflection loss relationship (1.25), it is required that the shield must have an high relative conductivity σ_r, hence a good conductor must be used. The shield thickness is not an important parameter: the metal thickness can be as small as possible.
- If the frequency is higher, the shield thickness must be chosen accordingly to the working frequency skin depth penetration. The equation (1.23) suggests the use of metals having high relative permeability μ_r and high conductivity σ_r. Unfortunately, these two conditions cannot be contemporaneously satisfied.
  The influence of the skin depth on the shielding effectiveness as function of frequency is highlighted in Figure 1.5, where two metals having different μ_r were considered.

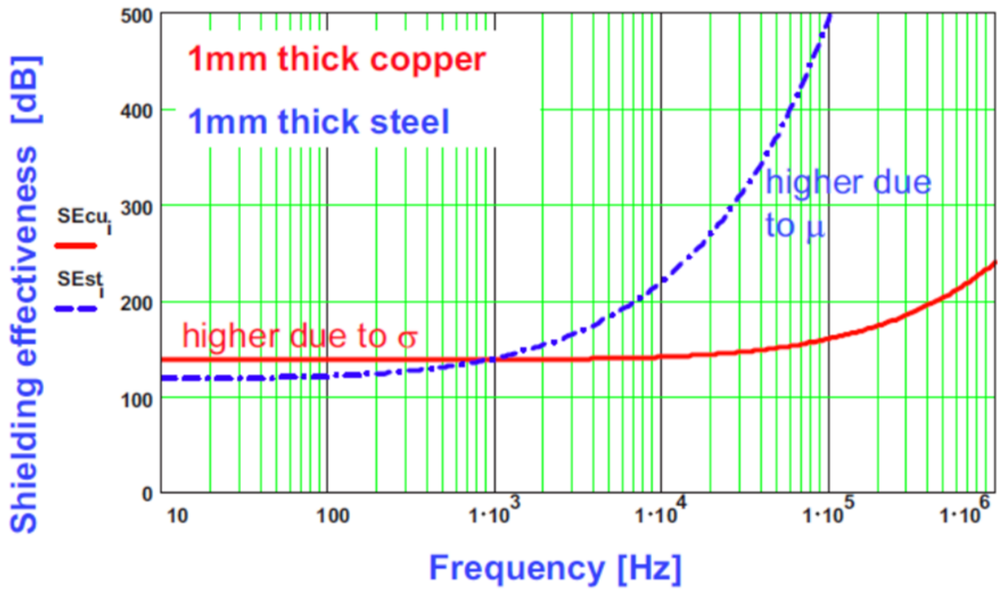

Figure 1.5: The influence of σ_r and μ_r on the shielding effectiveness. Plot taken from [2].

1.2 Shielding of near-field electromagnetic sources

The equation (1.17) represents the exact solution of the shielding effectiveness of a material against a plane wave. If the far-field conditions are not verified, the electromagnetic field has not a regular pattern, and the wave impedance are not constant; for this reason, in near-field zone, only approximate solutions can be studied.

The shielding effectiveness due to the absorption loss (1.27) and the multiple reflection loss (1.28) depends only on the material physic characteristics. The reflection loss term (1.25), instead, depends on the shield material and on the wave impedance; this parameter changes if the near-field condition is considered instead of the far-field one. To study the trend of the vacuum characteristic impedance either for the electric field and the magnetic field, a simplified method, which gives accurate results, is described in [1]. This method is based on two simplifying assumptions:

- PCB traces and the wires of electric circuits can be considered as short dipoles, if their length is smaller than ten times the wavelength of the current they lead.
- Transformers and coils can be compared to elementary magnetic dipoles, hence they are similar to small current loops.

The short electric dipole is then used as near-field electric source, while the small loop is considered as near magnetic field source. The results of the theoretic study done in [1] are reported in Figure 1.6, where the wave impedance of both sources are plotted with respect to the normalized distance r/λ_0. This figure shows that the short dipole electric field impedance is higher than 120π (η_0 in figure) in near-field zone, while the small loop magnetic field impedance is lower than η_0 in the same zone. Recalling the relationships (1.25) and (1.34), it can be concluded that:

- The shielding effectiveness due to reflection loss increases for electric field sources, if the wave to be shielded is in the near-field zone; the shield thickness can be reduced.
- Magnetic shielding is more difficult in near-field conditions, because of the lower reflection loss contribution. Transformers and coils must be shielded with higher thickness shields, independently on the working frequency.

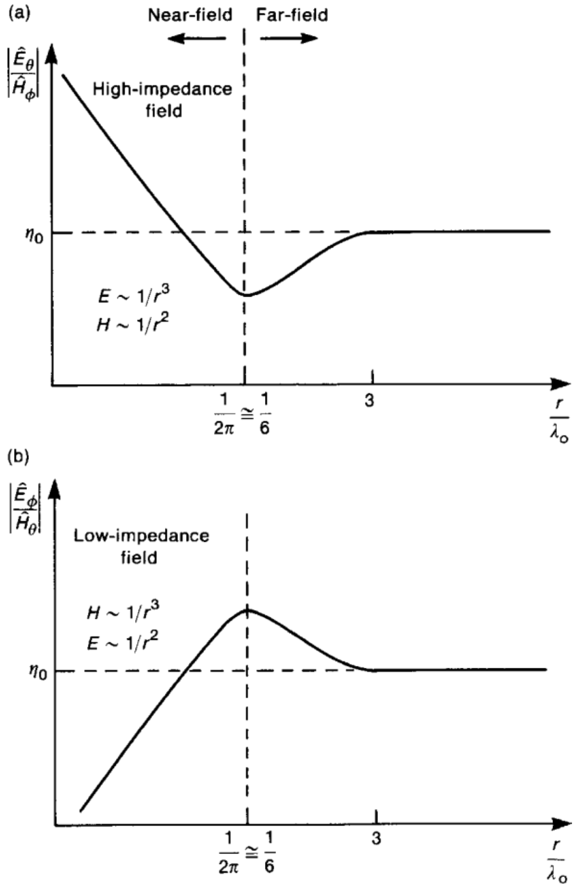

Figure 1.6: In vacuo wave impedance of electric field source (a) and magnetic field source (b) [1].

Chapter 2

Shielding effectiveness measurement methods

In this chapter the most important measurement setups for the shielding effectiveness evaluation of a generic material are described. They are substantially divided into two categories: the shielding effectiveness measurement methods for which the specimen must be tested with a plane wave are described in the 2.1 section. The measurement setups exciting the measured sample with an electric or magnetic field source are grouped in the 2.2 section instead. In this way, the chapter one division between near-field and far-field electromagnetic source is maintained also in this chapter. The first complete list of the measurement methods was done by Wilson *et al.* in [3] and [4]; for the most used methods they reported a very exhaustive description of the theoretical background and of the realized text fixture. Moreover, measurement examples ad a comparison between the test setups were also reported. Unfortunately, they published these two articles in the (relatively) far 1988, and until now none wrote a similar complete list of shielding effectiveness measurement methods.

Al the most important methods found by the candidate are reported in this chapter; it represents the state of the art of the varied choices an EMI researcher could make for measuring the shielding effectiveness of its novel material. For each measurement method a subsection is dedicated; its length is proportional to the importance it has in the EMI world. Its (eventual) standardization is highlighted; the old withdrawn standards (like the MIL STD-285) are not reported in this chapter. The only exception is done with the ASTM ES7-83 standard, which is described because it has recently reawakened the scientific research interest.

For each methods the most important parameters are highlighted. They are the measurement frequency range, the dynamic range (the maximum shielding effectiveness measurable value), and the physical sample shape and dimensions. The specimen thickness is also an important parameter, determined by its shielding properties and the dynamic range. For instance, if the specimen thickness is such that its shielding effectiveness is higher than the dynamic range, it must be reduced. To this aim, the specimen shielding effectiveness mast be predicted: if it is not possible, since some material properties are unknown, some specimens having different thickness must be tested.

As Tamburrano *et al.* stated in [5], at the state of art, there is not a unique SE test method that can be applied to whatever material type and at any frequency. Therefore, the characterization of new shielding materials in a wide frequency range, from a few kilohertz up to several gigahertz, requires the proper combination of multiple SE testing methods.

2.1 Far-field electromagnetic sources

2.1.1 Reverberation chamber

The reverberation chamber is one of the most affordable methods for measuring the shielding effectiveness of materials; measurements are repeatable in a wide frequency range, from few hundreds of megahertz up to tents gigahertz. These are only two of the many reasons why this method was standardized; a procedure describing how to use a reverberation chamber and how to validate it is described in the IEC 61000-4-21 norm. This standard does not describe how to build a test setup; as consequence, the reverberation chamber remains a specialized facility, although it is standard covered.

As briefly described in [3], the reverberation chamber is basically a shielded room working like a microwave oven. A transmitting antenna injects a signal inside the chamber whose frequency range is chosen in such a way that the room is large in terms of wavelength. Since the chamber cavity Q-factor is large (but not infinite), many propagation modes were excited, each one having its propagation direction and polarization. The result is a room having a multipath electromagnetic field inside, hose average power level is almost constant. Those are the reasons why with the reverberation chamber the specimens can be measured in a more realistic scenario than the other test methods based on a single plane wave excitation [6].

To obtain the described field distribution inside the shielded room there are two methods: the mode-tuning and the mode-stirring techniques. Since the mode-stirring is the most used, it is described first. In this method, some metallic paddles were rotated to continuously change the electrical dimensions of the shielded room, thus varying its Q-factor and allowing for the generation of an infinite number of modes. An example of a mode-stirred reverberation chamber setup is shown in Figure 2.1. The shielded room described in [7] is divided into two equal parts with a shielding wall placed in its center; the wall has an aperture used to hold the test specimen. The reverberation chamber is then the right side of the shielded room, while the left side (named receive side in Figure 2.1) is used to measure the electromagnetic wave that was not shielded by the tested specimen. In [7] is also highlighted the difference of the electromagnetic field power density with the stirrer paddle stopped (Figure 2.2-a) and rotating (Figure 2.2-

b); this last figure shows the typical uniform distribution of the electromagnetic field inside a reverberation chamber.

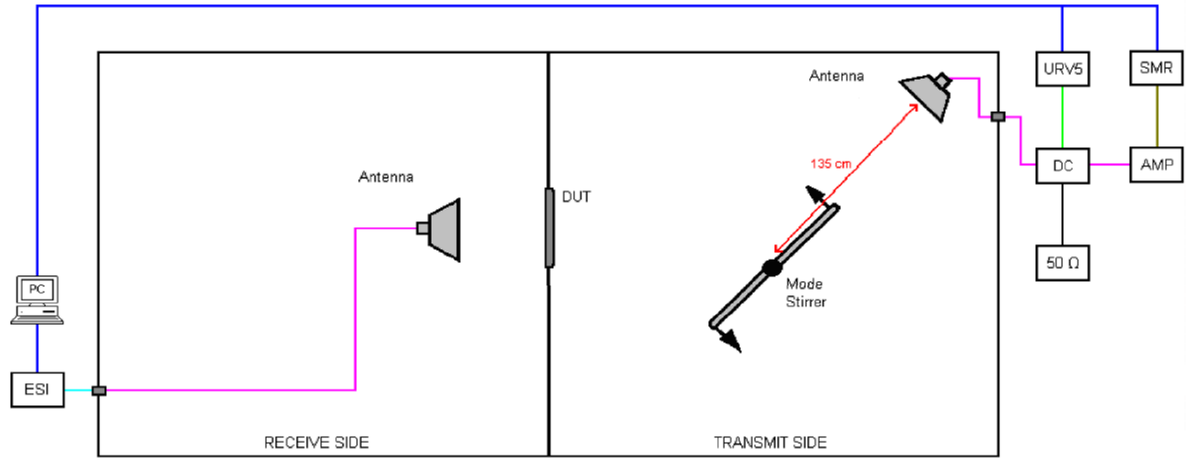

Figure 2.1: Mode-stirred reverberation chamber used in [7].

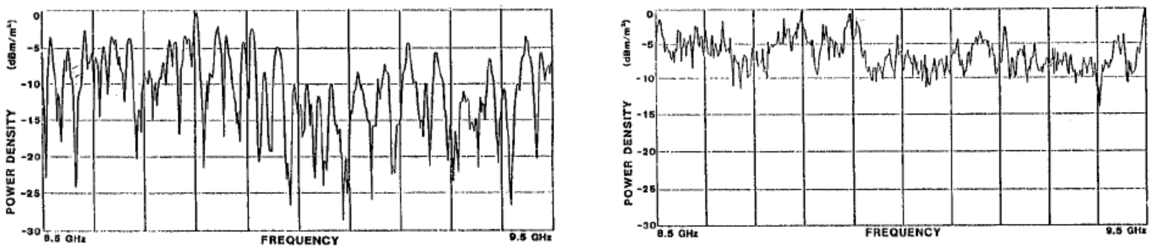

a b

Figure 2.2: Power density distribution measured in the reverberation chamber of Figure 2.1 with the stirrers stopped (a) and with the stirrer rotating (b). Plots taken from [7].

The test setup in Figure 2.1 is not the most used one because it requires too much space. Another solution is to substitute the receiving side of the shielded room with another chamber smaller than the reverberating one. This configuration is called **Nested reverberation chamber**. An example of this test setup is shown in Figure 2.3; here, $P_{oc,s}$ represents the power injected in the big chamber, while $P_{ic,s}$ is the power measured inside the inner chamber that is transmitted through the shield (test sample). As can be seen from this figure, a stirrer is placed also in the small chamber, in order to obtain a constant field distribution also in this enclosure. This is important because the directivity pattern of the antenna used for measuring the transmitted field can lead to incorrect results. The measurements accuracy is determined by the correction terms considered in the data elaboration method. An exhaustive study of the systematic errors and an effective correction formula is described in [8].

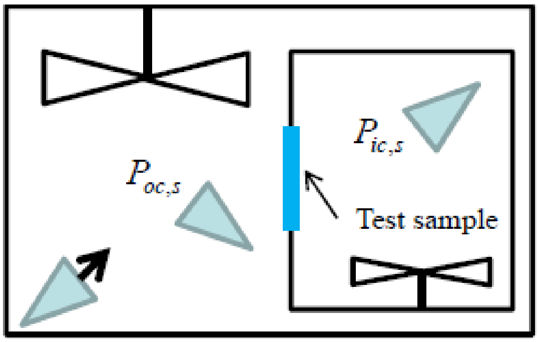

Figure 2.3: Basic nested reverberation chamber setup for measuring SE [6].

One of the first complete descriptions of the nested reverberation chamber setup is presented in [9]; the lower frequency limit is determined by the shielded room dimensions, which are $(10.82\text{x}5.18\text{x}3.96)\ \mathrm{m}$, giving a low frequency limit of 200 MHz. The high-frequency limit is determined by the amplifier band only. In this paper the choosing criteria for the stirrer velocity are also described.

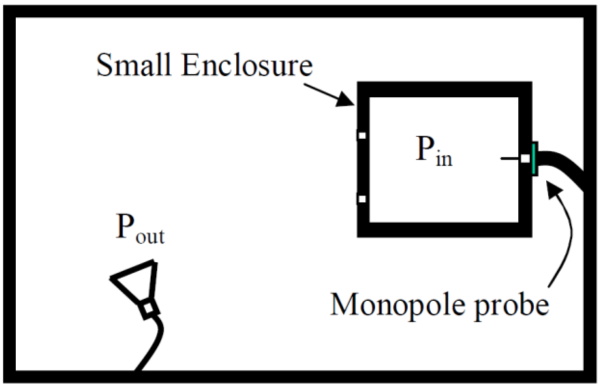

Figure 2.4: Mode tuned reverberation chamber setup described in [10].

The already mentioned IEC 61000-4-21 norm recommends that the small chamber dimensions must allow the placement of the receiving antenna and the paddles stirrer. If the shielding effectiveness of small enclosures must be tested, and either the receiving antenna and the paddle stirrer cannot be contained, nested reverberation chambers with the mode-tuning method could be used. In this approach, not only the shielded room must be large in terms of wavelength, but also the nested chamber. An example of the test setup described in [10] is reported in Figure

2.4: the transmitting antenna ($\mathrm{P_{out}}$) injects a signal having frequency equal to the desired measurement range. The unshielded signal will be coupled in the small enclosure, whose dimensions allows for a frequency stirring phenomena. Hence the unshielded power in the small enclosure has a uniform distribution, so the receiving antenna (a monopole in Figure 2.4) can be placed in any position inside the small enclosure. The major limitation of this method is the frequency range, which must allow for the frequency stirring of both chambers.

With any reverberation chamber it can be achieved a dynamic range up to $100 \mathrm{~dB}$, since the power impinging the tested shield is provided by a resonant cavity. This range is higher than the most part of the other described methods used for measuring the shielding effectiveness of materials. The maximum sample dimensions are limited by the aperture of the small enclosure or the shielding wall, which is about $(0.3 \mathrm{x} 0.3) \mathrm{~m}$. The only limitation of this method is the impossibility to measure dielectric materials, because, as the authors of the article [8] pointed out, bad electric contacts causes large measurement variations.

2.1.2 Measurement of shielding enclosures

To measure the shielding effectiveness of electromagnetic shielding enclosures the standards committee of the IEE electromagnetic compatibility society defined two standards according to the box dimensions: if the enclosure smallest linear dimension is larger than (or equal than) $2 \mathrm{~m}$, the IEEE 299™-2006 standard must be used [11]. If, instead, the smallest dimension of the measured enclosure is less than $2 \mathrm{~m}$, the IEEE 299.1™-2013 standard describes one measurement procedure for enclosures having dimensions between $2 \mathrm{~m}$ and $0.75 \mathrm{~m}$, and another completely different method for boxes smaller than $0.75 \mathrm{~m}$. In these standards the instrumentation to be used, the test setup and its validation, the detailed measurement procedure, the shielding effectiveness computation and the report details are described. The only not specified parameters are the measurement frequency points and the pass/fail requirement. The frequency range validity of this standard is $9 \mathrm{~kHz} \div 18 \mathrm{~GHz}$, (extendable down to $50 \mathrm{~Hz}$ and up to $100 \mathrm{~GHz}$) and is divided into three sub ranges:

1. Low frequency range, from $9 \mathrm{~kHz}$ to $20 \mathrm{~MHz}$;
2. Resonant range, from $20 \mathrm{~MHz}$ to $300 \mathrm{~MHz}$;
3. High-frequency range, from $300 \mathrm{~MHz}$ up to $18 \mathrm{~GHz}$;

For low frequency range both standards describes a measurement procedure in near-field conditions, hence it is not reported in this subsection.

The resonant range is covered only by the IEEE 299™-2006 standard. The enclosure fundamental resonance point could belong to this range, due to its physical dimensions; this is why this range is called resonant. In Figure 2.5 is showed the measurement setup for the $(20 \div$

100) MHz frequency range, for which biconical antennas must be used. The remaining frequency range setup is the same illustrated in Figure 2.5, with a $\lambda/2$ dipole used instead of a biconical antenna. The standard provides a formula to estimate the fundamental resonance frequency of the tested enclosure; once determined, measurements in both polarizations (horizontal and vertical) are required.

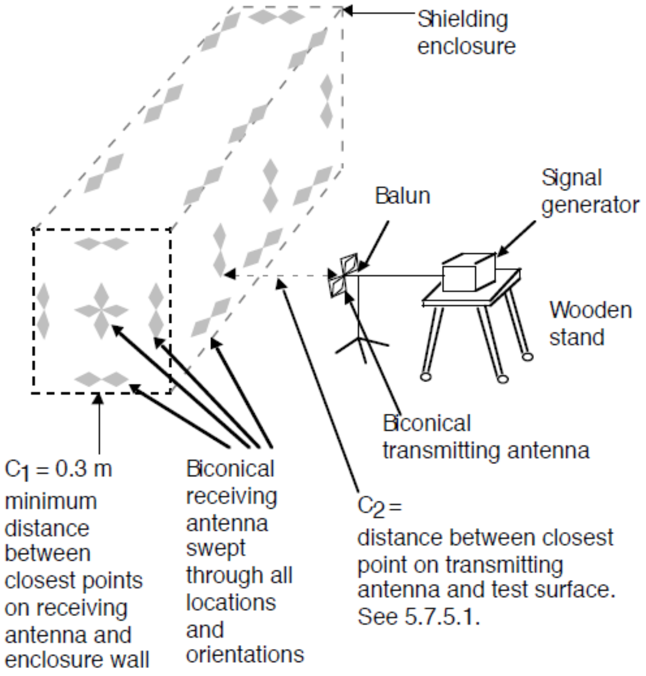

Figure 2.5: Resonant range measurement setup with transmitting biconical antenna [11].

The high-frequency measurement range also is divided into two sub-ranges: if the working frequency is in the $(0.3 \div 1)$ GHz sub-range, a $\lambda/2$ dipole antenna must be used both in transmission and in reception, as reported in Figure 2.6. For frequency higher than 1 GHz, instead, horn antennas must be used in a Figure 2.7 measurement test setup. Also with these setups the measurements must be done for both vertical and horizontal polarizations. Figure 2.6 and Figure 2.7 setups are described in the IEEE 299™-2006 standard, and are valid also for the testing of enclosures having smallest linear dimension greater than 0.75 m, as described in the IEEE 299.1™-2013 document.

If the enclosure to be tested has smallest linear dimension less than 0.75 m, a reverberation chamber must be used. The standard addresses to the IEC 61000-5-7 norm and to other articles cited in section 2.1.1, like [10] and [8], because the described measurement setups are the same. The mode stirring technique is recommended, because the dimensions of the considered enclosures does not allow for the installation of a paddle stirrer. In Figure 2.8 (a) the one port reverberation chamber is illustrated, while in Figure 2.8 (b) an alternative multiport setup is showed. The antenna placed inside the enclosure must be a monopole, while the source antenna must be a horn.

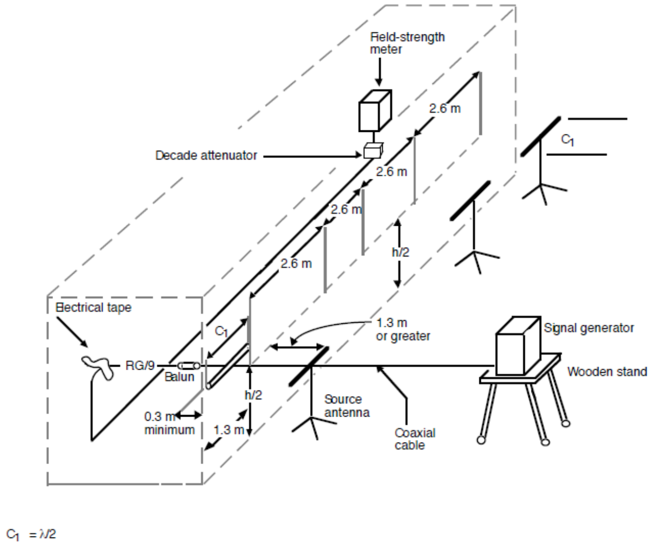

Figure 2.6: Measurement setup for frequencies ≤1000 MHz with dipole antenna [11].

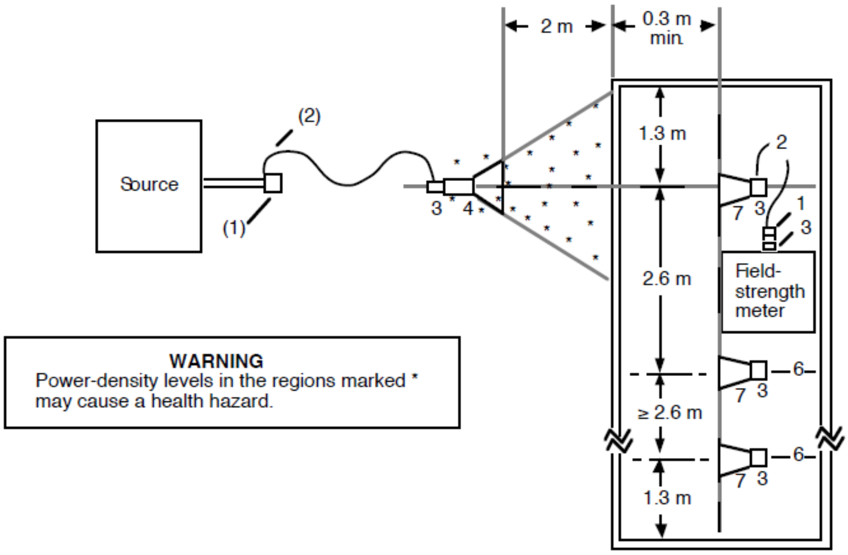

Figure 2.7: Measurement setup for frequencies >1 GHz [11].

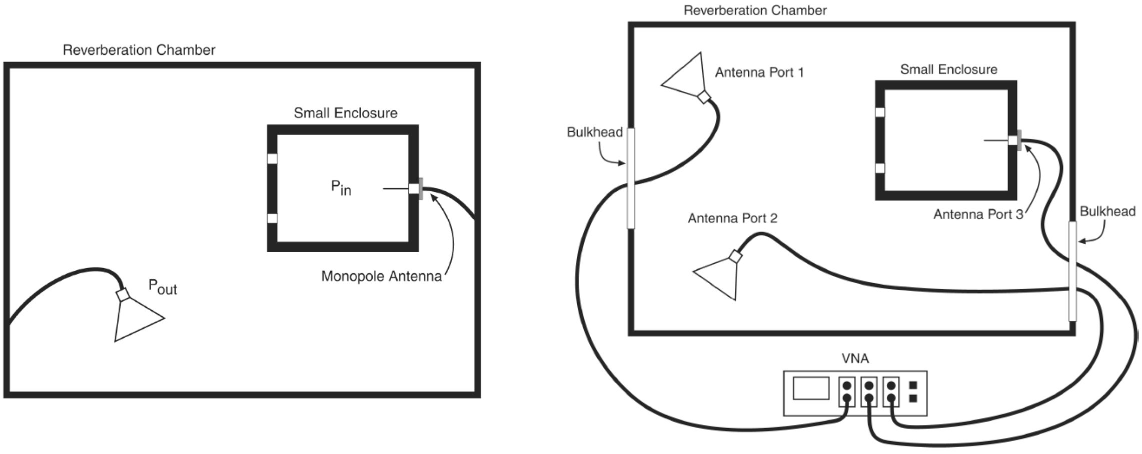

(a) (b)

Figure 2.8: One-port reverberation chamber for small enclosures (a), and Multiport measurement setup for determining SE of a small enclosure [12].

2.1.3 Gigahertz TEM (GTEM) cell

The GTEM cell is a test fixture generally used for precompliance measurements. A schematic view is reported in Figure 2.9; it is an enlarged coaxial transmission line having a pyramidal shape, with rectangular cross section, and a plane inner conductor not centered with respect to the b side (Figure 2.9 (b)). The feed is provided at the pyramid edge, while the GTEM cell end, which extends to some square meters, is terminated with an absorbing material. The device under test mast be located inside this “giant” coaxial line, and will be excited by an electromagnetic field distribution which is the same of a coaxial cable. Hence, the electric and magnetic field lines are orthogonal each other, exposing the tested device with a plane wave, having precise polarization and well-known amplitude. The TEM field power inside the cell could be very high, increasing the measurement dynamic range [13].

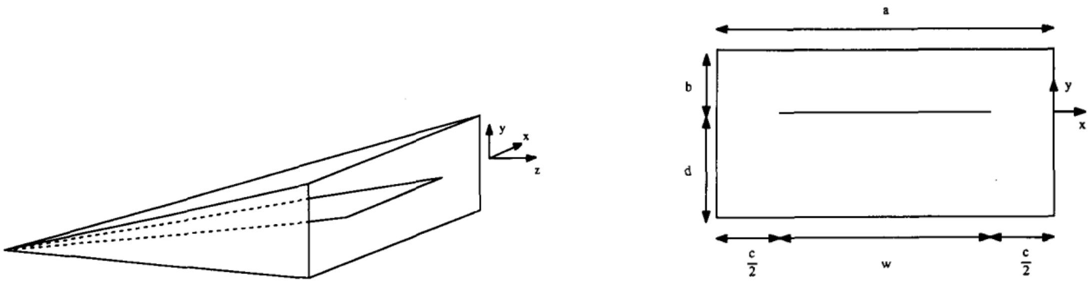

(a) (b)

Figure 2.9: Schematic view of a GTEM cell [14].

Small enclosures could be tested exciting them with a GTEM cell instead on a reverberation chamber. In particular, the shielding effectiveness of small enclosures, having linear dimension less than $0.75\ m$, described in the IEEE 299.1™-2013 standard, could be measured. A typical measurement setup is shown in Figure 2.10. The working frequency depends on the used GTEM cell; a typical range is DC to 8 GHz [15], with a dynamic range which is the same of a reverberation chamber, namely $(90 \div 100)$ dB. The enclosure dimensions are limited by the used GTEM cell maximum DUT size, which is determined by the requirement to have a uniform electromagnetic field; in [15] a $(0.45\text{x}0.45\text{x}0.23)$ m box is tested. Since the measured enclosures are typically resonating at the measurement frequency range, the mode-stirring technique is often unpractical. Mechanical frequency-stirring technique is used instead.

The results of a comparison of enclosures shielding effectiveness measurements done with the reverberation chamber and the GTEM cell is reported in [16]. Although this measurement setup is reliable and cost effective, it is not standardized.

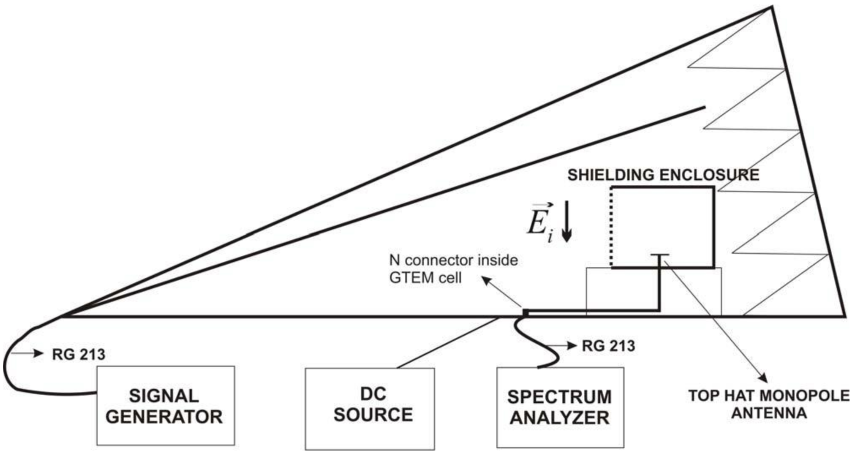

Figure 2.10: Schematic layout of the measurement setup in [15].

2.1.4 Continuous conductor coaxial holder (ASTM ES7-83)

The first standardized waveguide test fixture was an expended coaxial transmission line, whose dimensions and usage were described by the ASTM (American Society for Testing and Materials) committee. One example of the ES7-83 standard test fixture is reported in Figure 2.12, while a schematic view of its cross-section is showed in Figure 2.11. It is simply a coaxial conductor whose dimensions are expanded in such a way to maintain the 50 Ω characteristic impedance (same of its connectors). When excited, the TEM mode propagates inside the conductor from (theoretically) DC to approximately 1.4 GHz. The upper frequency limit is determined by the appearance of higher order modes, which depends on the transmission line physical dimensions. The TEM distribution of the electromagnetic field inside the coaxial holder is reported in Figure 2.13 and represents the reason why this standard becomes popular in shielding effectiveness measurements. Since the electric and magnetic field lines are orthogonal each other, the far-filed conditions are simulated in this coaxial transmission line. The test specimen is then excited with a planar wave impinging perpendicularly to the illuminated face. The shielding effectiveness is then computed as an insertion loss, measuring the transmitted wave with and without the test specimen.

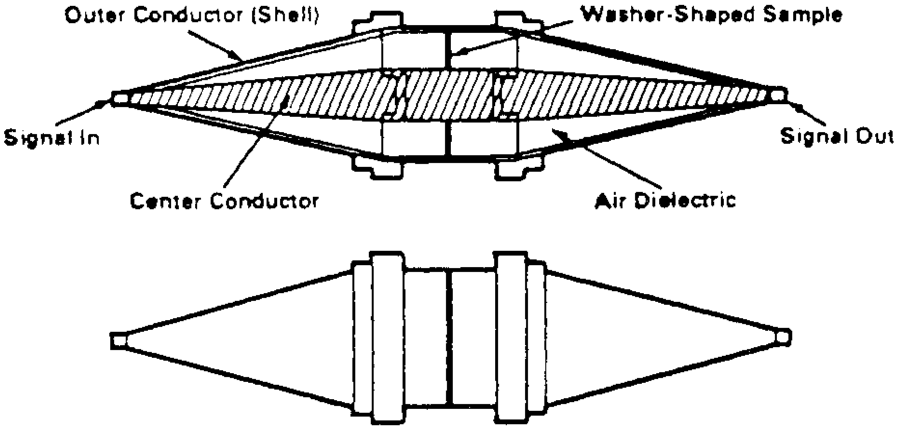

Figure 2.11: Continuous conductor coaxial transmission line holder parts draw [17].

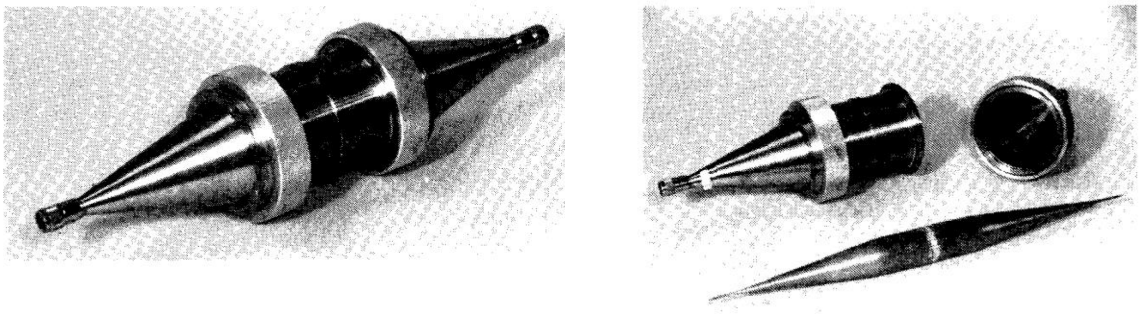

a b

Figure 2.12: The ASTM ES7-83 coaxial holder used in [17].

The material to be tested must be shaped as a thin annular disk fitting the air dielectric, and held with the outer conductor. The specimen thickness must be smaller than the skin depth penetration of the tested material, in order to avoid the measure of too high insertion losses; the dynamic range is, in fact, $(90 \div 100)$ dB [3].

Although the measurement and the sample preparation simplicity, this standard was withdrawn in 1988 [18], because of the leak in measurements repeatability. This problem was due to the requirement of a prefect electric contact between the specimen and the flange, as discussed in [3]. This problem was solved with another flanged coaxial holder, also standardized by the ASTM society, and described in the following 2.1.5 section.

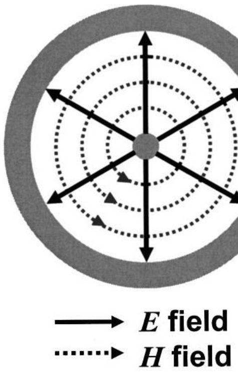

Figure 2.13: Electric (E) and magnetic field (H) lines distribution in the coaxial waveguide [19].

As already explained, this standard is described because, during the last decades, it was continuously further developed to increase its frequency range and to solve the contact problems.

2.1.5 Flanged coaxial waveguide (ASTM D4935)

According to the authors of [17], the National Bureau of Standards developed a coaxial transmission line based on the one described in the ASTM ES7 standard, but with a discontinuous central conductor. The result is a new test fixture having the same working principle of the old ES7 one, but very high measurements repeatability. A schematic view of this fixture is reported Figure 2.14, while an example of a commercial realization is reported in Figure 2.15. As can be seen from these figures, the coaxial transmission line is composed by two identical halves, terminating with an N-type conductor.

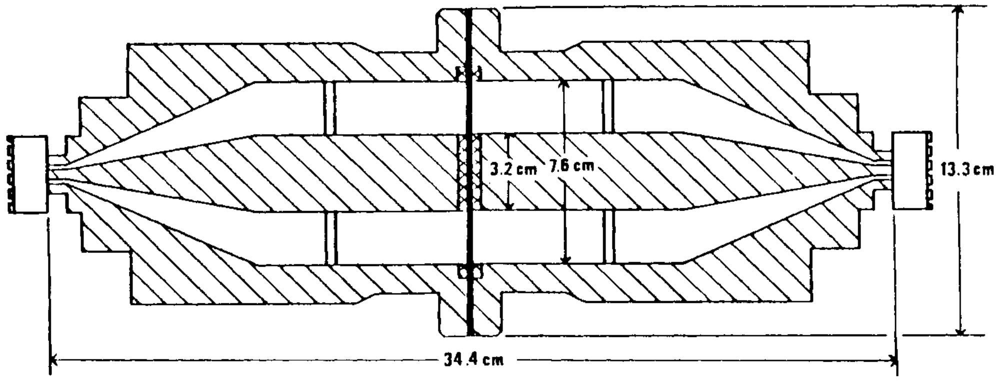

Figure 2.14: Cross section of a flanged coaxial transmission line holder [17].

The ASTM society standardized in the ASTM D4935 standard [20] this flanged coaxial waveguide and the measurement procedure. Both inner and outer conductor of this test fixture forms a flange, because they are interrupted and will be contacted only with the tested sample. For that reason, the measurement frequency range does not start from zero, but belongs to the $(30 \div 1500)$ MHz interval. The dynamic range is $(90 \div 100)$ dB. The measurement procedure is accurately described in [20]. Two specimens are required: a *reference specimen*, and the *load specimen* (Figure 2.16).

Figure 2.15: Electro-metrix coaxial waveguide realized according to the ASTM D4935 standard [21].

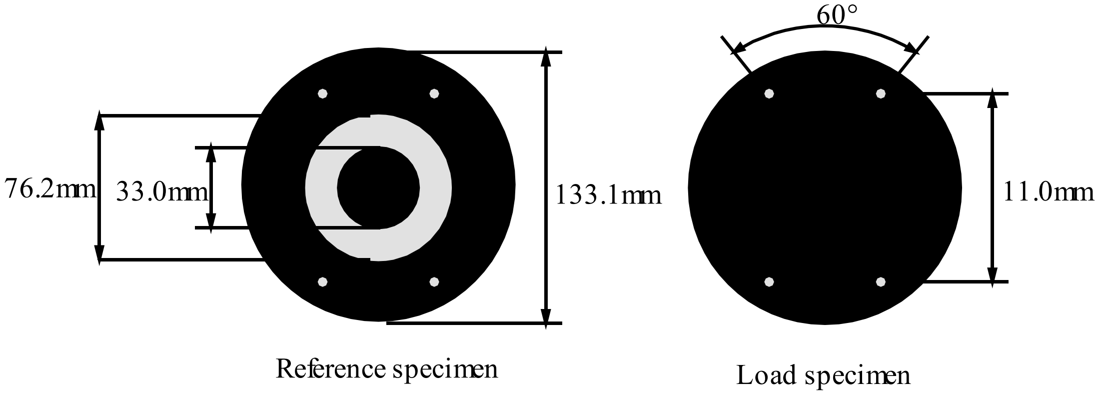

Figure 2.16: Reference and load specimen dimensions according to the ASTM D4935 standard [20].

Supposing to measure the shielding effectiveness of a thin conductor, the reference specimen is designed in such a way to put in contact the inner (outer) conductor of one half of the coaxial cable with the corresponding inner (outer) conductor of the other part of the fixture. The air dielectric is not interrupted. The aim of this specimen is to obtain a reference measurement of the transmitted power, named P_2. To obtain this result the two disks o this specimen must has identical thickness. The load specimen, instead, puts the inner and outer conductors in short circuit, in order to measure the transmitted power P_1. The shielding effectiveness is then identified as an insertion loss, according to the (1.2) definition [20]:

$$SE_{E|dB} = 10Log\left|\frac{P_1}{P_2}\right| \tag{2.1}$$

The very simple equation (2.1) is valid under some assumptions, which are very difficult to realize in practice. Firstly, both reference and load specimens must have the same thickness; according to the D4935 standard, this implies that the difference in average thickness must be less than $25\ \mu\mathrm{m}$, and the thickness variation within and between the specimens is less than $5\ \%$ in average. Secondly, the specimens thickness must be much smaller ($\ll 1/100$) than the tested material skin depth penetration. If this condition is not satisfied, no transmitted power can be measured, and P_2 is overlapped to the measurement setup noise. Moreover, if all the preceding conditions on thickness are satisfied, the measurement frequency range is reduced due to the appearance of higher order modes, for frequency smaller than the maximum declared by the ASTM standard. This phenomenon was exhaustively discussed in [22].

The electric contact problem of the ES7 coaxial waveguide is solved in the new D4935 standard with the insertion of insulating screws to tightly hold the two fixture halves. In this way, if the measured specimen is not conductive, the two conductor halves are capacitively coupled during the measurement phase of both reference and load specimens, leading a correct shielding effectiveness result. This is the advantage of this test method: there are no limitations about the material to be measured: it could be homogeneous or inhomogeneous, single or multi-layered, conductive or insulating. Moreover, the near-field shielding effectiveness can be evaluated starting from the measures of the S parameters, as described in the ASTM [20] standard.

Repeatability of measurements and no limitation on the tested material made this measurement method very popular, although the difficulties on the samples preparation and the measurement frequency limitation. This last limit was overcame with coaxial waveguides having smaller physical dimensions; the scientific literature is very rich of examples of new not standardized coaxial cables, showing the same good performances of the other standardized measurement method. Some examples of these new coaxial holder are described in [23], [24], [25], [5] and [26]. They are based not only on the ASTM D4935 test fixture, bat also on the withdrawn ASTM ES7 standard. The reason of the continuous conductor "revival" is due to the sample preparation simplicity (the reference specimen is not required) and the zero frequency lower limit [5]. However, the good electric contact is still a problem, hence these new coaxial holder musts be used with conductive materials.

2.1.6 Rectangular waveguides

An enlarged coaxial cable, like the ones already described, could be substituted with a rectangular waveguide to evaluate the shielding effectiveness of a material. The measurement setup schematized in Figure 2.17 is very simple: a vector network analyzer (VNA) is used to measure the scattering parameters of a rectangular waveguide transmission line. The specimen to be measured is inserted inside the waveguide, creating a line discontinuity. The sample can be either hold between two flanges, as reported in Figure 2.19 (a), or sized to fit the inner walls of a waveguide spacer (Figure 2.19 (b)). The measuring frequency range is the same of the waveguide TE_{10} mode (fundamental mode) whose electric and magnetic field lines are reported in Figure 2.18.

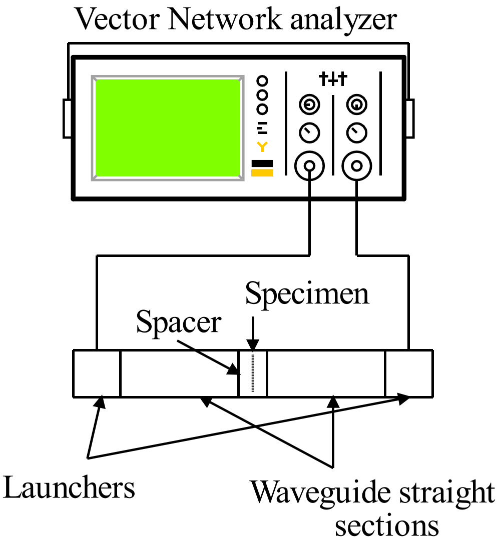

Figure 2.17: Measurement setup for measuring the shielding effectiveness of a specimen with a rectangular waveguide.

According to Hoang *et al.* [27], the shielding effectiveness can be obtained from the measured scattering parameters simply changing the sign of the S_{21} transmission coefficient magnitude, computed in decibels. An analytical demonstration of this shielding effectiveness computation is provided in [28]. However, also with the waveguide measurements the insertion loss definition could be applied, as made by Mehdipour, *et al.* in [29]. The decibels value of the shielding effectiveness $SE_{E|dB}$ is then computed according to the definition (1.2), measuring the S_{21} parameter either without the specimen (S_{21}) and with the specimen inserted inside the waveguide ($S_{21|spec}$), hence:

$$SE_{E|dB} = 20Log\left|\frac{S_{21}}{S_{21|spec}}\right| \tag{2.2}$$

for any point measured in the chosen frequency range.

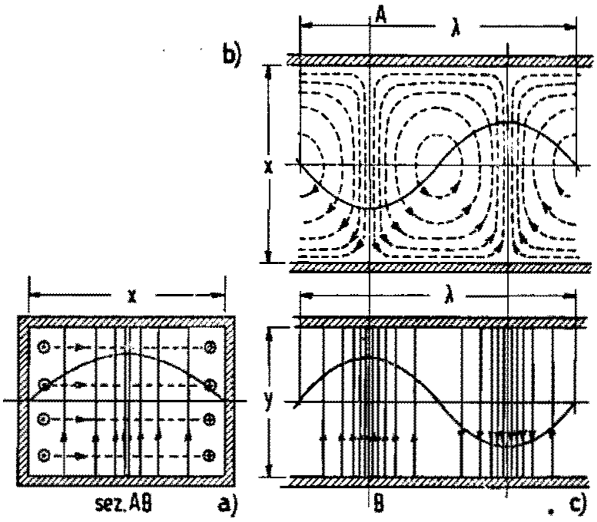

Figure 2.18: Electric (solid) and magnetic(dashed) field lines distribution of the TE_{10} fundamental propagation mode [30].

As the authors of [3] stated, the electric contact impedance between the sample and the waveguide should not be a problem, because the specimen must not create a short circuit across the transmission line (as made, for instance, in the ASTM D4935 coaxial holder).

The sample preparation simplicity and the measurement setup availability are not the only advantages of this method: due to the electric field lines distribution of the fundamental mode, the polarization (or the anisotropy) eventually presented in the measured material can be highlighted and evaluated. Some examples of polarized specimen measurements are provided in papers [31] and [32]. The dynamic range achievable with this method extends up to 90 dB [29].

The field lines distribution is also the reason why this method was never standardized: the TE_{10} mode does not simulate any of the standard shield test: high impedance source, low impedance source, near-field source or plane wave [3]. Since the two magnetic and the single electric field components cannot be separated, this electromagnetic field source cannot be compared to a near-field source. Hence, this measurement method is classified as a far-field method, although the wave impedance in a metallic waveguide is a function of frequency, as opposed to the far-field (plane wave or TEM mode) concept. This is the reason why this method is primarily used to measure the complex permittivity of dielectric materials, as described, for instance, in [33] and [29], instead of measuring its shielding effectiveness.

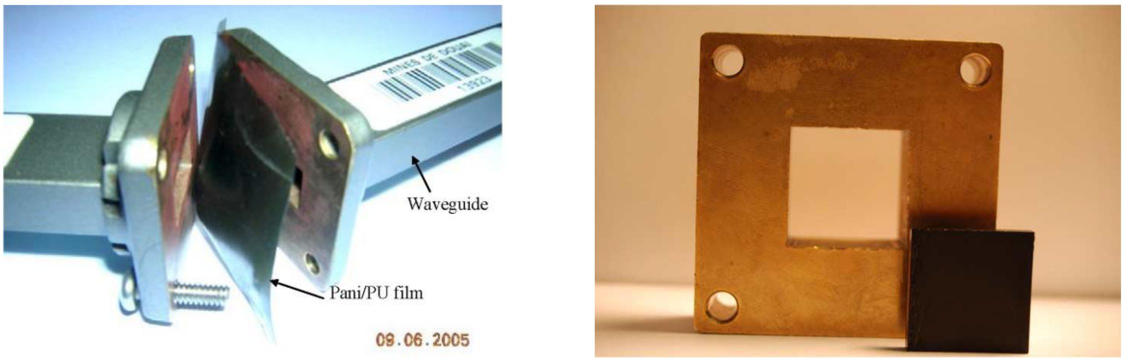

(a) (b)

Figure 2.19: Example of a specimen (Pani/PU film) inserted between two waveguide flanges [27] (a); A MWGNP sample (black parallelepiped) cut to fit a waveguide spacer [33] (b).

2.1.7 Time-domain technique

This method is described only in [34], [17] and [3], because it was not successfully used due to setup difficulties. In an anechoic chamber a rectangular panel, having dimensions of $(2.5 \text{ x } 2.8)\ \mathrm{m}$, must be inserted between two TEM horn antennas. The distance between the sample and an antenna is $30\ \mathrm{cm}$, assuring the far-field conditions. The measurement setup is shown in Figure 2.20.

The measurement procedure, as well as the setup realization, is not simple, because the waves transmitted trough the shield must be isolated from the ones diffracted by the sample edges. To solve this problem, the transmitting antenna is excited with short pulses, having known frequency and duration. The setup memorizes only the signals received during the time between the arrival of the transmitted wave and the edge-diffracted wave. This interval is called clean time. An FFT-based algorithm converts the received pulses, which gives the Shielding effectiveness in time domain, in the frequency domain: the frequency range is hence determined by the clean time, and is about $200\ \mathrm{MHz} \div 3.5\ \mathrm{GHz}$.

The dynamic range is $50 - 60\ \mathrm{dB}$, significantly lower than the one provided by the other methods: it is limited by the transmitting antenna maximum power, which cannot be too high otherwise waves diffracted by other setup elements can be received.

The principal limitations of this methods are the fact that only the transmitted waves can be measured (hence only the absorption loss), the relatively low dynamic range and the sample dimensions. To overcome this last limitation, the NBS used a copper plane with a circular aperture having diameter of 7.6 cm. However, the shielding effectiveness measurements presented in [3] shows some peaks probably due to the aperture resonances.

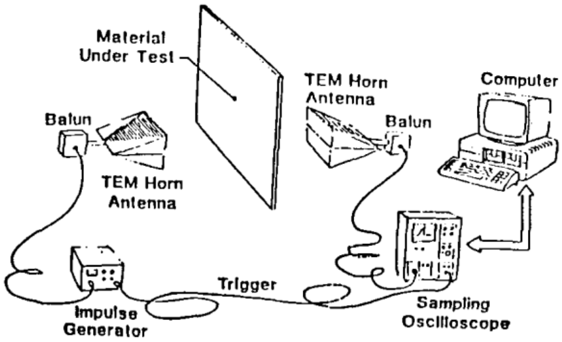

Figure 2.20: The time-domain shielding effectiveness measurement system [3].

2.1.8 Time-domain technique with absorber

The edge-diffracted wave, main problem of the method described in the 0 section, is solved absorbing it with an absorbing carbon-loaded polyurethane foam [35].

The schematic view of the measurement setup is showed in Figure 2.21. The source and the receiving antennas are ridged horns; the transmitting antenna simply illuminates the specimen with a plane wave, since it is properly located with respect to the receiving antenna, while the field diffracted from the sample edges is absorbed by the multilayered polyurethane foam. The receiving antenna only detects the signal transmitted through the shield, giving an information of its shielding effectiveness.

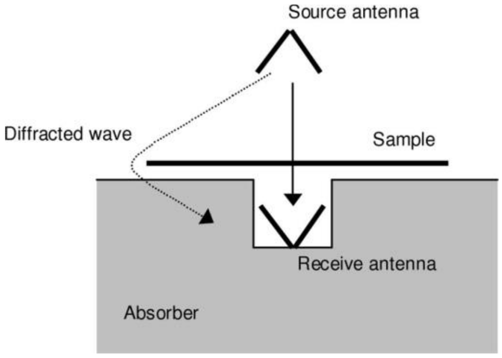

Figure 2.21: Proposed method showing absorption of diffracted energy [35].

The final setup is schematized in Figure 2.21 and showed in Figure 2.22 (a). A reference specimen, having known shielding effectiveness, is required. Marvin *et al.* used a holed brass sheet, measured with the ASTM D4935 coaxial cable.

One disadvantage of this method is that the absorber foam creates a rectangular waveguide having cutoff frequency of about $1\ \mathrm{GHz}$, so the electromagnetic field illuminating the specimen is not a pure plane wave. Another disadvantage could be the sample dimension, which is a circle of $60\ \mathrm{cm}$ diameter. On the other hand, with this very cost-effective method, a dynamic range of about $100\ \mathrm{dB}$ is achievable in a $(1 \div 8.5)\ \mathrm{GHz}$ frequency range. Moreover, the measurement results are in good agreement with the ones obtained with some other standardized methods, like the reverberation chamber and the ASTM coaxial holder.

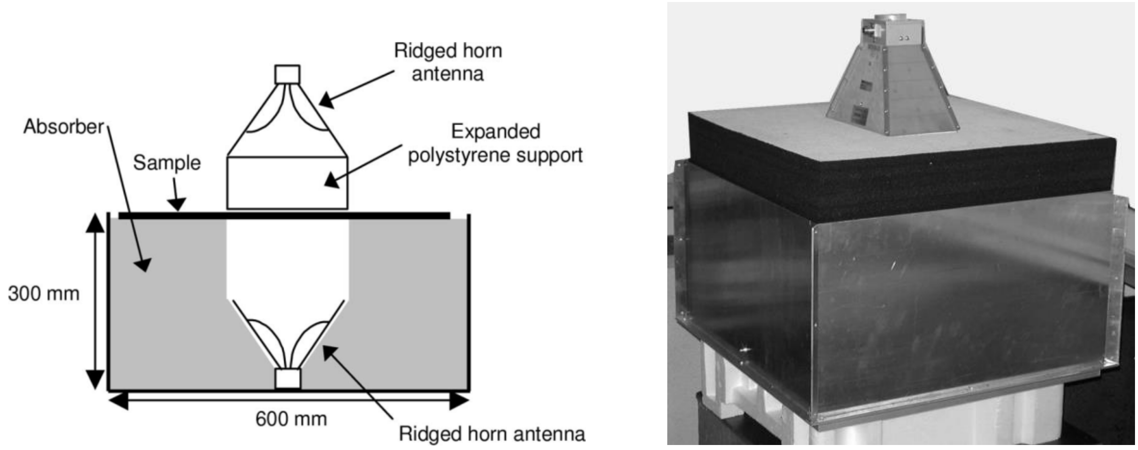

(a) (b)

Figure 2.22: Final measurement setup purposed by Marvin *et al.*:
schematic view (a) and its realization (b) [35].

Although this purposed measurement method is not standardized, it was used by other searcher to measure, for instance, the shielding effectiveness of composites nanostructured materials [36], or to measure the wave transmitted through a printed circuit board (PCB) [37].

2.1.9 Open field measurements

If it is required to measure the shielding effectiveness of “big enclosures”, such an aircraft fuselage [38], which cannot be tested in an anechoic chamber, it is possible to do some measurements in an open space, as showed (for instance) in Figure 2.24.

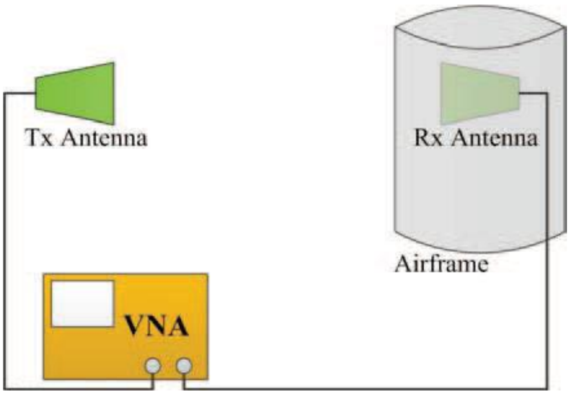

Figure 2.23: Test setup of this shielding effectiveness measurement method [38].

Since this is not properly a measurement method, different methods could be applied to the setup in Figure 2.24. The most obvious solution is to use the measurement setup described in [39] and schematized in Figure 2.23, where a cylindric enclosure, having the same diameter of the aircraft fuselage, is tested. Two horn antennas, one transmitting, the other one used in reception, are aligned and spaced in such a way to verify the far-field conditions. With this setup a reference measurement is performed, in order to obtain the unobstructed signal power and to account for the ambient reflections and disturbances at the measurement frequency. Different measurements are done rotating both antennas. The receiving antenna is then located inside the dummy shield, and the shielded signal intensity are done locating both antennas in the same position chosen for the reference measurements.

Figure 2.24: Carbon–fiber reverberation chamber in shielding effectiveness measurement configuration [38].

The acquired data are then post-processed applying an inverse Fourier Transform to reproduce a time-domain signal, which is used in the same time gating technique, described in the 2.1.7 section, to eliminate the ground reflected received signals, thus isolating the direct path through the shield.

Another very similar solution is described in [38], where the dummy aircraft fuselage is modeled as an electrically large reverberation chamber. The transmitting antenna is the illuminator of a frequency-stirred chamber. In this test setup the aircraft fuselage substitutes the small chamber of a nested reverberation chamber setup described in 2.1.1 section. The measurement frequency range is $(1\ \mathrm{GHz} \div 6)\ \mathrm{GHz}$, with a $35\ \mathrm{dB}$ dynamic range.

The shielding effectiveness of a space shuttle Endeavour was evaluated by Johnk *et al.* in [40], with the test setup schematized in Figure 2.25. In this paper the shuttle hangar was used in place of the big chamber of a frequency-stirred reverberation chamber measurement setup. The Endeavour is used as the nested small chamber. The rated measurement frequency range is $30\ \mathrm{MHz} \div 6\ \mathrm{GHz}$ while the dynamic range is not declared due to NASA copyright.

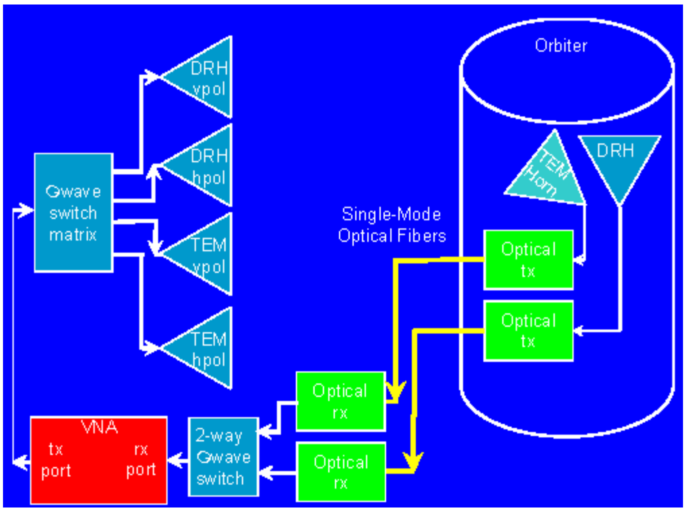

Figure 2.25: Block diagram of the measurement setup described in [40].

2.1.10 Shielding effectiveness from complex permittivity

The far-field shielding effectiveness of a dielectric material can be predicted from its complex permittivity, as briefly described in [3]. In this paper, Wilson *et al.* stated that this method is limited to low loss materials and not highly conductive composites, for frequency ranges up to (only) $100\ \mathrm{MHz}$, due to the availability of measurement setups. However, the years following the paper [3] shows a very rich research on theoretical prediction and measurement methods of the complex permittivity of composites materials, especially in the microwave frequency range.

One of the most used measurement setups is the one based on the rectangular waveguide, described in section 2.1.6.

As the authors of the paper [41] states, the literature is very poor of research about the prediction of absorbing materials shielding effectiveness starting from its complex permittivity. Hence, they described a complete theoretical study for calculating the shielding effectiveness of dielectric materials, accompanied by an experimental verification with measurements of $\mathrm{SiC_f/SiCN}$ composites.

2.2 Near-field sources

2.2.1 Magnetic shielding effectiveness

The magnetic field shielding effectiveness of metallic plates and magnetic (high permeability) materials could be measured in near-field zone. The used source is an elementary magnetic dipole (electrically small loop) placed near the tested specimen and aligned to another identical loop, used as receiver. The near-field distance is determined by the low frequency range used with this method, whose maximum value is about $1\ \mathrm{MHz}$.

A typical measurement setup is showed in Figure 2.26 [42]: a large copper plate, $(63\mathrm{x}49)\ \mathrm{cm}$, is placed between two $6\ \mathrm{cm}$ radius loops, which are $7.5\ \mathrm{cm}$ spaced. The rated frequency range is $100\ \mathrm{Hz} \div 1\mathrm{MHz}$. Recently, in literature, this method is usually called MSE near-field (Magnetic Shielding Effectiveness).

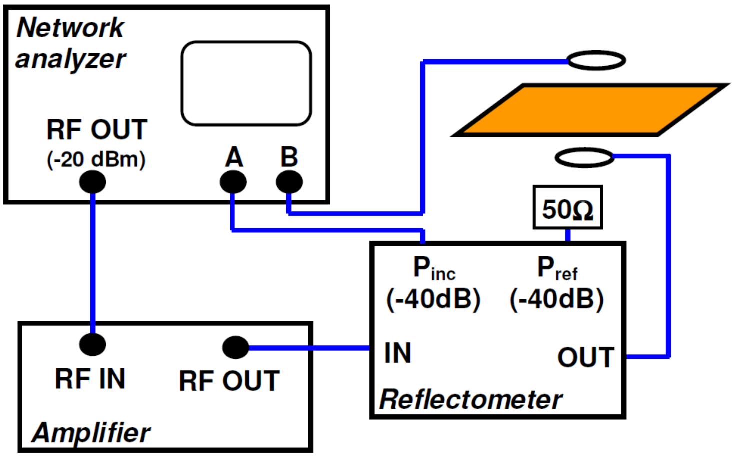

Figure 2.26: Example of test setup for near-field MSE measurements [42].

The first complete theoretical study of the shielding effectiveness with this measurement method can be found in [43] while a brief description of this widely used method, called Eddycurrent meter, can be found in [44]. The major interest of this method, during the last decades, is due to the diffusion of wireless battery chargers and power electronics equipment in electric cars, which produces high intensity low-frequency radiations that must be shielded [45].

This test method is standardized for the measurements of shielding enclosures in the already described IEEE 299™-2006 standard, with the test setup schematized in Figure 2.27. In this standard, the usable frequency range is the lower one, $9\ \mathrm{kHz}$ to $20\ \mathrm{MHz}$, for enclosures having smaller linear dimensions less than $2\ \mathrm{m}$. The IEEE 299.1™-2013 standard validates this setup for smaller enclosures down to $0.75\ \mathrm{m}$.

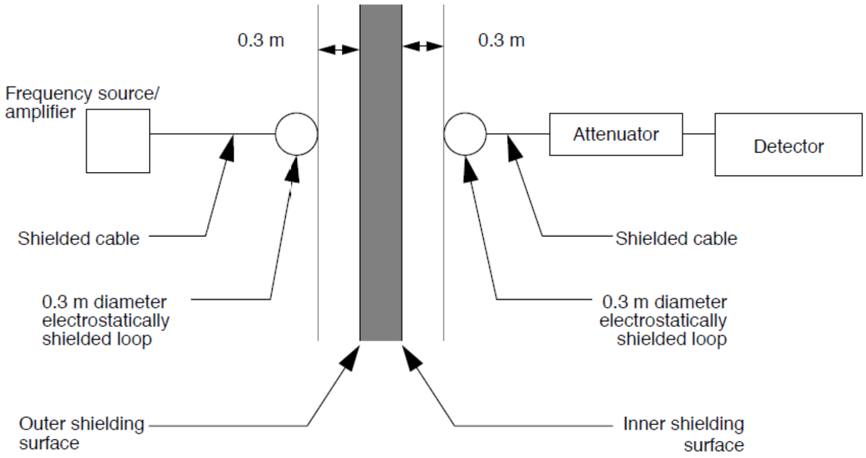

Figure 2.27: Schematic diagram of the test configuration for magnetic tests showing dimensions of transmit (TX) and receive (RX) antennas [11].

2.2.2 Dual TEM cell

A single TEM cell is a rectangular coaxial transmission line (RCTL) having dimensions larger than the diameter of a coaxial cable. The inner and outer conductors are designed in such a way to maintain a $50\ \Omega$ characteristic impedance in the whole cell length. Coaxial connectors are provided in both RCTL ends, to wire it with measurement coaxial cables. This test fixture is very similar to the already described ASTM D4935 waveguide holder; however, as the authors of [4] pointed out, there is no advantage in using this rectangular transmission line in the same fashion. Instead, two identical RCTLs could be stacked and coupled with an aperture, creating the dual TEM (DTEM) cell.

An example of dual TEM cell realization is reported in Figure 2.29, while the orthogonal sections of the test fixture described in [4] is schematized in Figure 2.28. In this figure, the upper cell is chosen to be the driving cell, since it is fed at port 2, while the lower cell, used in reception, is wired to a network analyzer with ports 1 and 4. The port 3 is simply terminated with a 50 Ω resistor. The aperture transfers power from the driving cell to the receiving cell via the square aperture. Here is inserted the specimen for which it is asked to measure the shielding effectiveness.

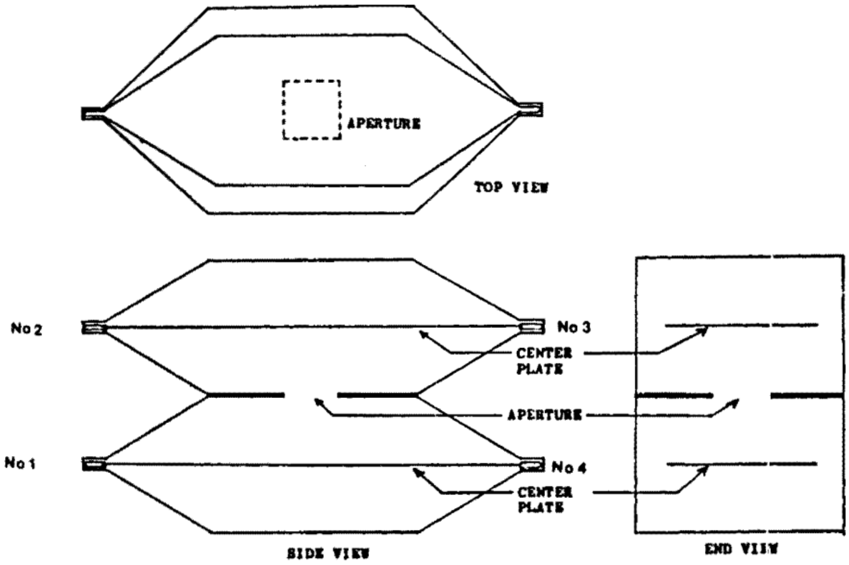

Figure 2.28: Dual TEM cell schematic [4].

Since this aperture couples energy asymmetrically, the penetration of normal electric field and tangential magnetic field through the sample could be measured. Hence, with tis test fixture it is possible to measure the shielding effectiveness of a specimen against both the near electric and magnetic field sources. The DTEM cell design equations and a design example could be found in [46]. The measurement frequency range is 1MHZ ÷ 4GHz, lower limited by the stray coupling of the cell [47], while the upper limit is due to the cell resonances. The achievable dynamic range is $(50 \div 60)$ dB [40], limited by the need of a perfect electric contact, which is very difficult to obtain; in [47] a solution for this problem is presented.

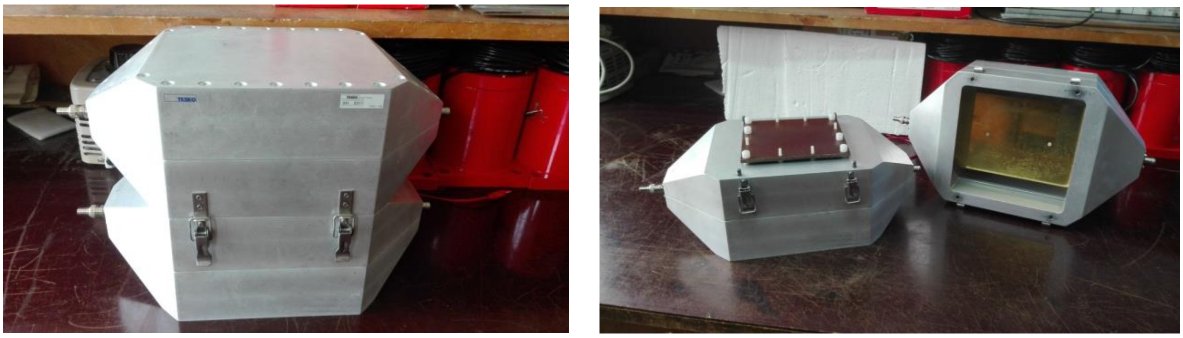

(a) (b)

Figure 2.29: An example of dual TEM cell described in [48].

One advantage of this test fixture is the required specimen dimensions, which are smaller than the other described methods; in [47], for instance, a $50.4\ \mathrm{mm}$ square sample is tested. As the authors of [48] pointed out, this is not a standardized method for measuring the shielding effectiveness of materials.

2.2.3 Opened (apertured) TEM cell

In the dual TEM cell fixture, already described in the 2.2.2 section, the cell used in reception could be excited not only by another identical rectangular coaxial transmission line, but also with a reverberation chamber or a gigahertz TEM cell. The result is the so called apertured TEM cell, a rectangular coaxial line with one of the shielding faces completely removed. An exhaustive study of the apertured TEM cell is presented in [49]; the cell used by the authors of this article is showed in Figure 2.30.

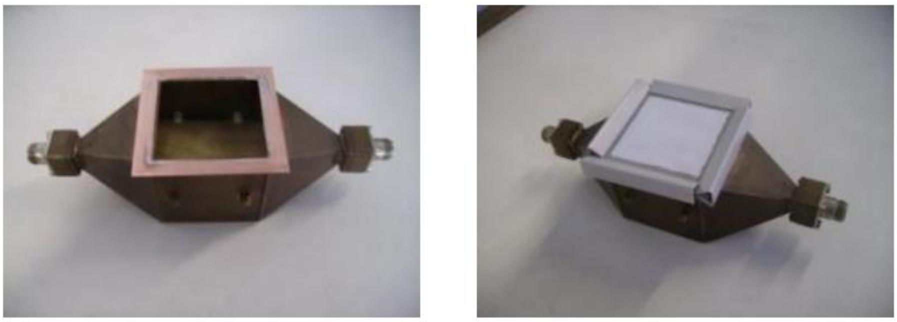

Figure 2.30: Apertured TEM cell without and with test sample in place [49].

Wilson and Ta underlined in [4] that the advantage to use this cell as a probe in a reverberating chamber is the cell is excitation, which is obtained with an electromagnetic field having a statistically uniform amplitude. Moreover, the electric and magnetic field couplings could be separated, collecting the unshielded signal power with in both cell terminals, and doing the sum and the difference of the output signals with an hybrid coupler. The disadvantage of the reverberation chamber excitation is that the direction and the polarization of the field impinging the specimen is unknown. If it is a problem for the required measurements, a GTEM cell could be used as a source of a well-defined electromagnetic field direction and polarization.

Another possibility with the GTEM cell is to use it as a receiver, since the GTEM cell is used mainly for radiated emission measurements. In this setup, the apertured TEM cell act as a source of electromagnetic field. The power generated by the TEM cell is then measured with the GTEM cell with and without the sample placed on the aperture. A comparison between these two approaches is provided by Pocai *et al.* in [49].

The authors of the paper [50] used small electric and magnetic probes to evaluate the shielding effectiveness of shielding cans. The S parameters of a 180° hybrid coupler were measured to compute the specimen shielding properties with respect to electric and magnetic near-field sources. The measurement setup of this study is shown in Figure 2.31. With the described methods, the sample dimensions, the frequency range and the measurement dynamic range are the same of the GTEM cell and the dual TEM cell.

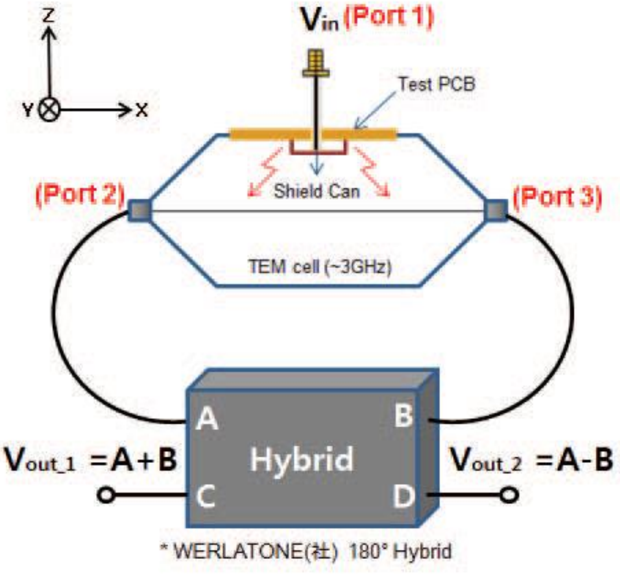

Figure 2.31: Test setup of TEM cell with a hybrid to measure S parameters of [50].

Chapter 3

Materials and samples realization

As explained in the Summary chapter, in this thesis the shielding effectiveness of different biochar types and graphene coating are measured in the microwave frequency band. The specimens preparation and the characterized materials are described in this chapter. They are composites material, made with epoxy resin and biochar, and composites coating on epoxy resin, made with a conductive polymer and graphene. Those coating composites were described in the 3.2 subsection, and were studied and realized in the Politecnico di Milano department of "Chimica, materiali e ingegneria chimica Giulio Natta". Hence, more of the 3.2 subsection contents are taken from the [51] master's thesis.

3.1 Biochar-based composite materials

In material sciences a **composite material** (or shortened, composite) is a material realized with two or more constituent, having completely different chemical and physical properties, which forms a heterogeneous mixture. One of these materials, which constitute the most part of the composite volume, is a homogeneous mixture acting as a binder, and is called matrix. The other constituent material, called reinforcement (or filler), is supported by the matrix and modifies its chemical and physical properties, allowing for the creation of a totally new material. Epoxy resins and polyester resins are examples of organic polymers used as matrix in a composite material. Epoxy resin is mainly used in aerospace industry as a structural glue, and for boat and floors coating. Its capability to polymerize at ambient temperature (e.g. 25°C) and its non-toxicity are only two of the reasons why epoxy resins are used to create composites, especially in a preliminary research step, when the study of a novel filler is required.

In this thesis a commercial epoxy resin is used as matrix for biochar powders. The used resin is a Hexion EPIKOTE™ Resin MGS™ RIMR 135 to be mixed with a curing agent EPIKURE™ Curing Agent MGS™ RIMH 134 or RIMH 137 [52]. The main physical characteristics of this resin are reported in Table 3.1, while a complete list of its physical characteristics is reported in 0.

Characteristic	**Unit**	**Value**
Density	g/cm³	1,13 - 1,17
Viscosity	mPas	700 - 1.100
Pot life 96	MM.SS	96
Operational temperature	°C	-60 to +50 without heat treatment -60 to +80 after heat treatment
Processing temperature	°C	10 °C to 50 °C

Table 3.1: Hexion RIMR 135 main physical properties [52].

The word **biochar** is combined with the words "bio" (biomass) and "char" (Charcoal). It is a solid material obtained as by-product of the biomass pyrolysis [53] when they are processed to realize biofuels. Biochar is mainly used for soil amendment, waste management and heavy materials absorbent in soils. Moreover, it is carbon-negative, which means that it has the capability to sequestrate the carbon produced by microorganisms in soil, thus reducing the soli carbon emitted in the atmosphere. For this reason, biochar is a very promising material for the solution of the climate changes problems [53]. Recently the possibility to realize microbial fuel cells, direct carbon fuel cells and supercapacitors was investigated [54]; however, the electromagnetic shielding properties of this material are currently under investigation [55], [56].

The biochar characterised in this thesis were produced by two factories, with two completely different pyrolysis processes:

1. Bioforcetech corporation © biochar, produced starting from the waste water, yard waste, food waste and biosolids [57]. These materials are dried and pyrolyzed with a BioDryer and a P-Five Pyrolisis reactor, both Bioforcetech patented technologies. The pyrolysis is obtained burning the gases produced by the processed materials in a flameless environment.
2. A biochar supplied from Muhammad T. Afzal from University of New Brunswick, Canada. These biochar were produced starting from wood pellets and oat straw, with two pyrolysis process: a standard pyrolysis, similar to the one used by Bioforcetech, and a novel microwave-heating process, described in [54]. Their names and fabrication processes are reported in Table 3.2.

As it will be highlighted in the 3.1.1 subsection, some of the used biochar are conductive; their electrical resistivity depends not only on the used material, but also on the pyrolysis process.

Biochar name	Material	Process
PT-1	Wood pellets	Microwave pyrolysis, 2500W
PT-2	Wood pellets	Conventional pyrolysis, 500°C
PT-3	Oat straw	Conventional pyrolysis, 500°C
PT-4	Oat straw	Microwave pyrolysis, 2500W
PT-5	Wood pellets	Conventional pyrolysis, 500°C
PT-6	Wood pellets	Conventional pyrolysis, 600°C

Table 3.2: The used Afzal Biochar.

3.1.1 Composites preparation

The realized composites materials are a homogeneous mixture of epoxy resin with a biochar powder. The mixing process, in material sciences, is called dispersion. To obtain an homogeneous dispersion of a matrix with some powdered filler, such as carbon nanotubes, two processes could be used: the sonication mixing or the mechanical mixing with an Ultra-Turrax®. Unfortunately, both methods tend to create microscopic bubbles inside the dispersion, which cannot be eliminated neither with an exposure of the prepared specimens in a vacuum chamber. Since the curing reaction starts immediately after the mixing of the resin with its curing agent, it cannot be exposed for a long time (e.g. one hour) in a vacuum environment. The used epoxy resin, in fact, requires some hours to allow for the complete air bubbles escape, due to its density and viscosity. For those reasons, a mechanical mixer, based on a slow rotating paddle stirrer, was properly designed and described in section 3.3.

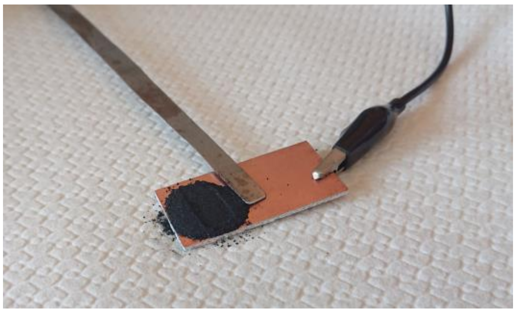

Figure 3.1: The used setup for measuring the DC resistance of a biochar powder cup. The red terminal, not showed, is connected to the steel paddle.

The Afzal's biochar at our disposal were primarily chosen according to their electrical resistivity; it was estimated with an approximative procedure, since there were no standard methods for measuring the resistivity of conductive powders.

A Fluke 8545A 6,5-digit bench multimeter [58] was used to measure the DC resistance of a cup of biochar powder, in a measurement setup showed in Figure 3.1. The steel paddle in this figure was firstly leaned on the powder, then a weak pressure was applied, finally it was strongly pressed until the biochar thickness reached approximately one millimetre. The results of the preliminary resistivity measurements are reported in Table 3.3. Looking at this table, the PT-1 and PT-4 biochar must be preferred due to its low resistivity; hence, they were chosen together with the PT-6 biochar, used to make a comparison of two biochar having the same origin, but different pyrolysis process (see Table 3.2). The used biochar (Figure 3.2) were firstly grounded with a mortar, then dispersed in the RIMR 135 component of the epoxy resin with the realized paddle stirrer. Each biochar was added to the resin component either in 10% and 20% weight, to obtain a significant change of the epoxy resin physical characteristics. To complete the preparation of the composite material, the curing agent was then added. With these composites the tested specimens were prepared according to the procedure described in the 3.5.1 subsection.

Biochar	Applied pressure	Measured resistance
PT-1	leaned	Tents megaohms
	weak	Tents kiloohms
	strong	Hundreds of ohms
PT-2	leaned	Infinite
	weak	Infinite
	strong	Hundreds megaohms
PT-3	leaned	Hundred megaohms
	weak	Tents megaohms
	strong	Unit of megaohms
PT-4	leaned	Unit of megaohms
	weak	Units of kiloohms
	strong	hundreds of ohms
PT-5	leaned	Infinite
	weak	hundreds of megaohms
	strong	Hundreds of megaohms
PT-6	leaned	infinite
	weak	Tents of megaohms
	strong	Unit of megaohms

Table 3.3: DC resistance estimation of the Afzal's Biochar.

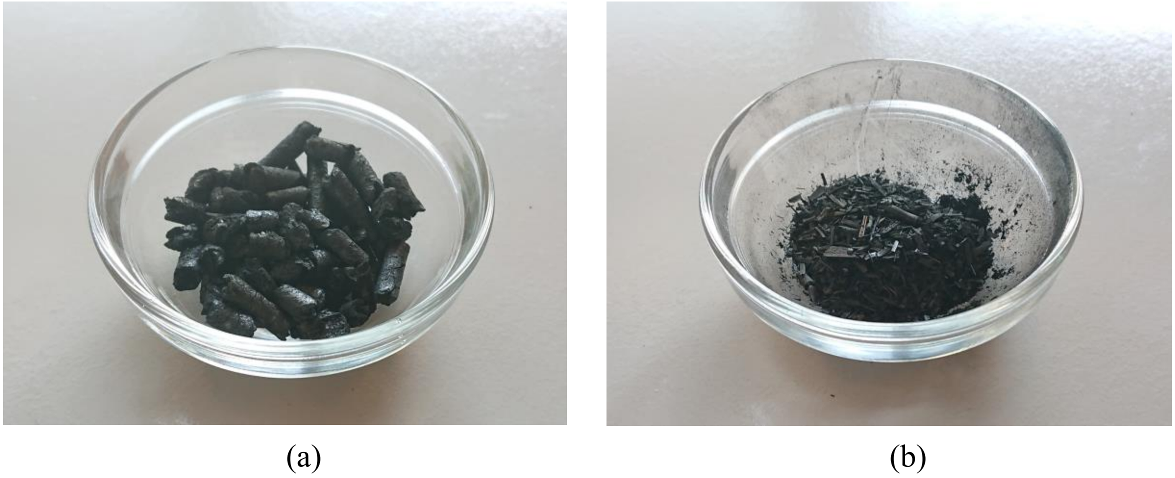

(a) (b)

Figure 3.2: The wood pellet PT-1 (a) and the oat straw PT-4 (b) biochar before the mortar grounding.

3.2 Conductive polymers-based composites

Intrinsically **conductive polymers** are a group of organic polymers having chain structure, density and mechanical properties of conventional polymers, and electrical, electronic, and optical properties comparable with the ones of metals [51]. Since they are very similar to semiconductors, they requires the addition of impurities (dopant) to become conductors. Unlike the silicon and other inorganic semiconductors, the organic polymers conduction mechanism is more complex, and is already under investigation [59] [60]. Doping is a reversible redox reaction that adds (n-doping) or removes (p-doping) electrons from the polymer backbone, leaving charged defects which can be delocalized as charge carriers. However, like the silicon-based semiconductors, the conductivity of those polymers is strongly influenced by the kind and amount of dopant and by the processing conditions. Conducting polymers are materials of interest for many applications such as OLEDs, flexible electronics, batteries, supercapacitors and corrosion protection.

Polyaniline (often called **PANI**) is a conductive polymer widely studied because of its good environmental stability and ease of synthesis. It has tunable physical properties because of its different oxidation states, and because not only it can be doped by an oxidative mechanism, but also by acid-base reaction. There are many types of polyaniline, either electrically conducting or insulating. The conductive form, called Emeraldine Salt (PANI-ES), is obtained by oxidative polymerization of aniline in an acidic environment, and has the appearance of a dark green powder. PANI were used, together with graphene, as filler of a polyester resin, to obtain the coating materials characterized in this thesis.

Graphite is one of the allotropes of carbon, the most stable in standard conditions. It has a hexagonal structure, obtained by the stacking of 2D hexagonal lattices with a 2-atom basis. Atoms in the plane are bonded covalently, while bonding between layers is via weak van der Waals bonds. Hence, the graphite layers could be easily separated, or exfoliated to different extents even up to a monolayer, which is called graphene. Graphene is a material widely used in electronic due to its exceptional electrical conductivity, even better than the Silver resistivity. When used as fillers for composites, performances depend on the dispersion procedure and on the amount of filler. The better the exfoliation of graphite up to the single monolayer, the better the composite electrical properties. Graphene could be obtained with graphite exfoliation, which is the preferred technique to realize large quantities of plates to be used as a filler in composites, since this productive process is scalable. This production cycle yields a mixture of monolayer and few layers graphenes, commonly called graphite or **graphene nanoplatelets (GNP)**, with average thickness depending on the degree of exfoliation.

3.2.1 Conductive polymers composites coating realization

All the coatings described in this subsection were realized in the laboratories of the “Chimica, materiali e ingegneria chimica Giulio Natta” department. They were deposited on an epoxy resin pristine sample, prepared before by the candidate.

The PANI coating was dispersed in a polyester resin according to the procedure described as follows. A PANI dispersion was obtained using $30\ \mathrm{ml}$ EtA (Ethyl Acetate) per gram of PANI, which was sonicated for an hour at $59\ \mathrm{kHz}$ and 100% power in a beaker, then it was turbomixed for 15 minutes at $9000\ \mathrm{R.P.M.}$ After that it was necessary to add an extra $30\ \mathrm{ml}$ EtA per gram of PANI again because of the rapid EtA evaporation. The dispersion was hence sonicated again for 15 minutes, then the polyester resin was added, and after 15 minutes of sonication procedure the crosslinking initiator was added. Coatings were deposited on epoxy resin substrate using a Walther-Pilot Mini manual spray gun. The coatings were sprayed until a homogeneous covering of the surface was obtained, left for about 30 minutes at room temperature, and cured in an oven with a thermal cycle of 15 minutes at 80°C first, then a thermal ramp up to 150°C was applied, finally they were cured for 20 minutes at 150 °C.

A different procedure was used to obtain the dispersion of GNP in a polyester resin. GNP were preliminary dispersed in EtA, sonicated for one hour at $59\ \mathrm{kHz}$ and 100% power using $150\ \mathrm{ml}$ EtA per gram of GNP. After that it was mechanically stirred at $500\ \mathrm{R.P.M.}$ for an hour. It was then necessary to add again $150\ \mathrm{ml}$ EtA per gram of GNP because of the rapid EtA evaporation during the stirring procedure. The GNP and PANI dispersion, obtained using $30\ \mathrm{ml}$ EtA per gram of PANI, were then sonicated for an hour at $59\ \mathrm{kHz}$ and 100% power in two different beakers. The PANI dispersion was then added to the GNP dispersion and turbomixed for 15 minutes at 9000 R. P. M., hence sonicated for 15 minutes. Polyester resin was then added, and the dispersion was sonicated again for 15 minutes before adding the crosslinking initiator. The obtained composite was deposited using the same procedure used for the PANI composite.

3.3 Epoxy resin mixer

As already mentioned in the 3.1.1 subsection, the epoxy resin and the filler must be slowly mixed with a mechanical stirrer based on a rotating paddle. As can be seen from Figure 3.3, the device was realized with a drill press, a stepper motor and a brass paddles stirrer. The rotating paddles dimensions fits the baker inner diameter, and their shape was designed in such a way to obtain a homogeneous dispersion without air bubbles inside the composite. The circuit design phases and its realization steps are described in this section.

Figure 3.3: The realized mechanical mixer.

3.3.1 Circuit overview

To slowly mix the epoxy resin with the filler, the only requirement for the motor is the low speed rotation (less than ten RPM), hence a unipolar stepper motor, half-step driven, is used. The driver circuit for the stepper motor is fully analog, because a microcontroller-based circuit (or a digital circuit) is not an optimized solution to accomplish this simple task.

The designed circuit is shown in Figure 3.4; it is based on a NE555 timer, working as a sawtooth oscillator, and on a bar LED display driver (LM3914). The first 8 outputs of the LM3914 integrated circuit were used to generate the eight phases driving a generic unipolar stepper motor. Diodes D1 to D8 are a diode matrix that is utilized to extract four signals starting from the eight outputs of the IC2; those signals are used to properly drive the four transistors T2 to T5, which will drive the unipolar stepper motor. To realize the power stage, PNP transistors were chosen, because the LM3914 outputs are current sinks.

The IC2 turns on the output corresponding to a defined voltage level applied to its pin 5; to have its outputs turning on sequentially, a sawtooth control signal is used.

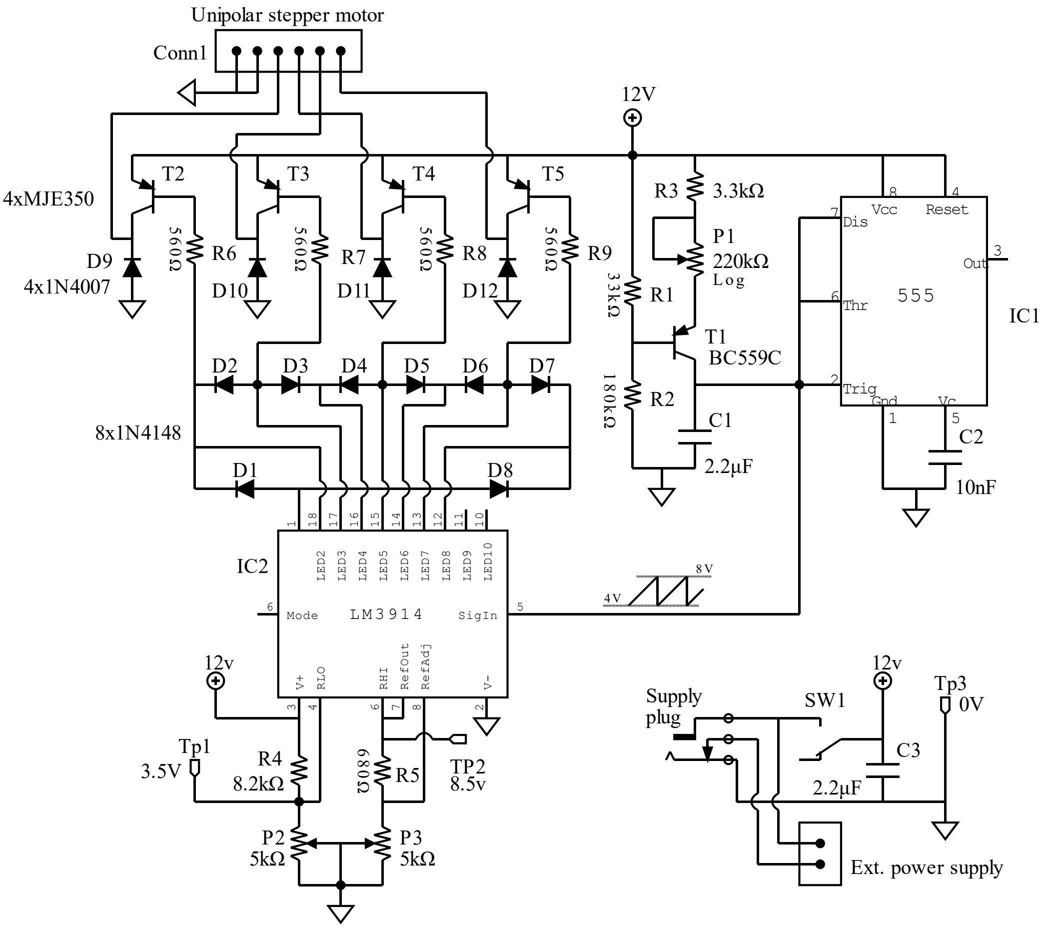

Figure 3.4: Schematic diagram of the designed stepper motor driver circuit.

The capacitor C1 is charged with a constant current with the T1 transistor. Given V_{cc} the 12 V power supply, the NE555 timer is used to charge the capacitor C1 to a voltage level equal to $2/3V_{cc}$; after that it is rapidly discharged until the voltage across it reaches the $1/3V_{cc}$ level. The trigger and threshold pins of the timer are wired in such a way that the oscillator circuit is self-starting. The oscillator frequency is changed turning the potentiometer P1; its value is in the $(0.632 \div 41.15)$ Hz range. This interval was chosen to have the paddle rotating slowly enough (a precise value in RPM is not required).

3.3.2 Design procedure

In this section the circuit design details are reported; the description is divided into three subsections, following the three blocks the circuit is divided to. The used approach is bottom-up: the Sawtooth oscillator is first described, because its output signal level determines the reference levels for the Bar LED display integrated circuit, hence the P_2, P_3, R_4 and R_5 resistors. However, the PNP transistors of the Output power stage sinks from the LM3914 a current which is determined by the R_5 resistor value, so the second designed circuit part is the Output power stage.

Sawtooth oscillator

The low frequency value of the oscillator suggests the use of a large capacitance for the C_1 capacitor, and low $(\leq 1 \text{ mA})$ values of the T1 bias current. Electrolytic capacitors were avoided due to their ESR parasite, which is a problem during the charge phase. Non-polarized mylar capacitors were than used, and this choice limits the value of the capacitance to few microfarads. A 2.2 µF capacitor was chosen for C_1, while a bias current of 1 ma was set for the emitter T1 current. The BC559C datasheet [61] gives the h_{fe} and V_{EB} data:

$$h_{fe,min} = 400 \tag{3.1}$$

$$V_{EB}(@Ic = 1ma) = 0.66\ V \tag{3.2}$$

The value of the base current I_B is then computed as:

$$I_B = \frac{I_C}{h_{fe,min}} = \frac{1ma}{400} = 2.5\ \mu A \tag{3.3}$$

The current I_p of the voltage divider, based on R_1 and R_2, was chosen to be greater than ten times the computed base current, so that

$$I_p \simeq 50\ \mu A \tag{3.4}$$

Since the voltage across the R_3 resistor must be at least $10\%V_{cc}$, to guarantee the transistor polarization stability, the value of R_1 is computed as:

$$R1 = \frac{V_{EB} + V_{R3}}{I_p} = \frac{V_{EB} + V_{cc} \cdot 0.01}{I_p} \tag{3.5}$$

substituting the (3.2) and (3.4) into (3.5), the R_1 value results $R_1 = 37.2$ kΩ. The nearest E12 series standard value was chosen to be:

$$R_1 = 33\ k\Omega \tag{3.6}$$

By inverting the voltage divider formula, the R2 resistor was computed:

$$R_2 = R_1 \cdot \left(\frac{V_{cc}}{V_{EB} + V_{R3}} - 1 \right) \tag{3.7}$$

with this equation, a standard value immediately results for R_2:

$$R_2 = 180\ k\Omega \tag{3.8}$$

The expression relating the R_3 resistor and the C_1 capacitor with the output signal period is taken from the manual [62]:

$$T = \frac{C_1}{2} \cdot \frac{\frac{2}{3} V_{CC} \cdot R_3 \cdot (R_1 + R_2)}{R_1 \cdot V_{CC} - V_{EB}(R_1 + R_2)} \tag{3.9}$$

Knowing that the sawtooth signal period is in the range $(0.0243\ \div\ 1.58325)$ s, the value of R_3 is computed from the equation (3.9), when the potentiometer P1 is set to zero (minimum period):

$$R_3 = T_{min} \cdot \frac{R_1 \cdot V_{CC} - V_{EB}(R_1 + R_2)}{\frac{2}{3} V_{CC} \cdot \frac{C_1}{2} \cdot (R_1 + R_2)} \tag{3.10}$$

substituting the obtained data in the (3.10) relationship, the R_3 value is $R_3 = 3.31$ kΩ, which leads to the following nearest standard value:

$$R_3 = 3.3\ \text{k}\Omega \tag{3.11}$$

The value of P1 is computed from the (3.10) equation substituting the maximum oscillator period $\mathrm{T_{max}}$ instead of $\mathrm{T_{min}}$, obtaining $\mathrm{P_1} = 215.7\ \mathrm{k\Omega}$. The nearest E12 series standard value for P1 is then:

$$P_1 = 220\ k\Omega \tag{3.12}$$

Output power stage

The coils of the used stepper motor sink a 300 ma continuous current from the collectors of the MJE350 medium power transistors. The considered collector current Ic is:

$$I_C = 350\ mA \tag{3.13}$$

From the ON semiconductor datasheet [63] the collector to emitter saturation voltage $\mathrm{V_{ECSAT}}$, the base to emitter saturation voltage $\mathrm{V_{EBSAT}}$, and the $\mathrm{h_{fe}}$ minimum current gain value were red:

$$V_{ECSAT} = \ 0.2\ V \tag{3.14}$$

$$V_{EBSAT} = 0.9\ V \tag{3.15}$$

$$h_{fe} = 30 \tag{3.16}$$

as good design rule, an $\mathrm{h_{fe}}$ value lower than the minimum one was considered:

$$h_{fe} = 20 \tag{3.17}$$

with these data the polarization resistor $\mathrm{R_6}$ (T2 transistor) is computed:

$$R_6 = \frac{V_{cc} - V_{EBSAT} - V_{ECSAT}}{\frac{I_C}{h_{fe}}} \tag{3.18}$$

the equation (3.18) gives $R_6 = 588.6\ \Omega$, which leads to the choice:

$$R_6 = R_7 = R_8 = R_9 = 560\ \Omega \tag{3.19}$$

Since the base current $\mathrm{I_B}$, for any transistor, is:

$$I_b = \frac{I_C}{h_{fe}} = \frac{0.35A}{20} = \ 17.5\ mA \tag{3.20}$$

The power dissipated from anyone of these polarization resistors is less than 0.25 W. Moreover, since for any transistor the power dissipation is:

$$P_{diss} \simeq V_{ECSAT} \cdot I_C = 350mA \cdot 0.2V = 70\ mW \tag{3.21}$$

heatsinks are no necessary.

Bar LED display integrated circuit

The amplitude of the sawtooth signal applied to the IC2 pin 5 is included in the range $(4 \div 8)$ V, as dictated by the NE555 comparator thresholds. This range is divided into 8 parts, as the number of the stepper motor phases, having amplitude equal to 0.5 V.

In order to have the first output (IC2 pin 1) turned on when the input signal voltage is in the $(4 \div 4.5)$ V range, the voltage applied to the lowest terminal of the IC2 internal voltage divider is:

$$V_{RLO} = 3.5\ V \tag{3.22}$$

This voltage is applied to the pin 4 of the LM3914 IC and is obtained from the R_4 to P_2 voltage divider. A test point Tp1 was added on the PCB to simplify the adjustment procedure. The same consideration holds for the highest voltage pin of the internal comparator, which is applied to the pin 6 of the IC2, and is measurable using the Tp2 test point.

Since the power transistor polarization current must be delivered from the LM3914 IC, the R5 resistor value must be computed accordingly, using the simplified formula reported in the datasheet [64]:

$$R_5 \simeq \frac{12.5}{I_{LED}} = \frac{12.5}{17.5mA} = 714\ \Omega \tag{3.23}$$

where I_{LED} is the current sunk from each medium power transistor base terminal. The equation (3.23) reads $R_5 = 714\ \Omega$, so the nearest lower standard value was chosen:

$$R_5 = 680\ \Omega \tag{3.24}$$

The voltage across the R3-P5 series resistors is called $V_{ref,out}$ in the LM3914 datasheet; a specific formula is given to compute the P3 value:

$$V_{ref,out} = 1.25 \cdot \left(1 + \frac{P_3}{R_5}\right) \tag{3.25}$$

This voltage must equate the upper value for which the last output must be turned on; to have the 8th output on when the input voltage is in the $(7.5 \div 8)$ V range, the $V_{ref,out}$ voltage must be equal to 8.5 V. The P_3 value can be now computed with the (3.25), obtaining $P_3 = 3.94$ kΩ, leading to the standard value:

$$P_3 = 5\ k\Omega \tag{3.26}$$

3.3.3 PCB realization

The printed circuit board (PCB) relative to the Figure 3.4 schematic diagram, was drowned with a CAD, and shown in Figure 3.5.

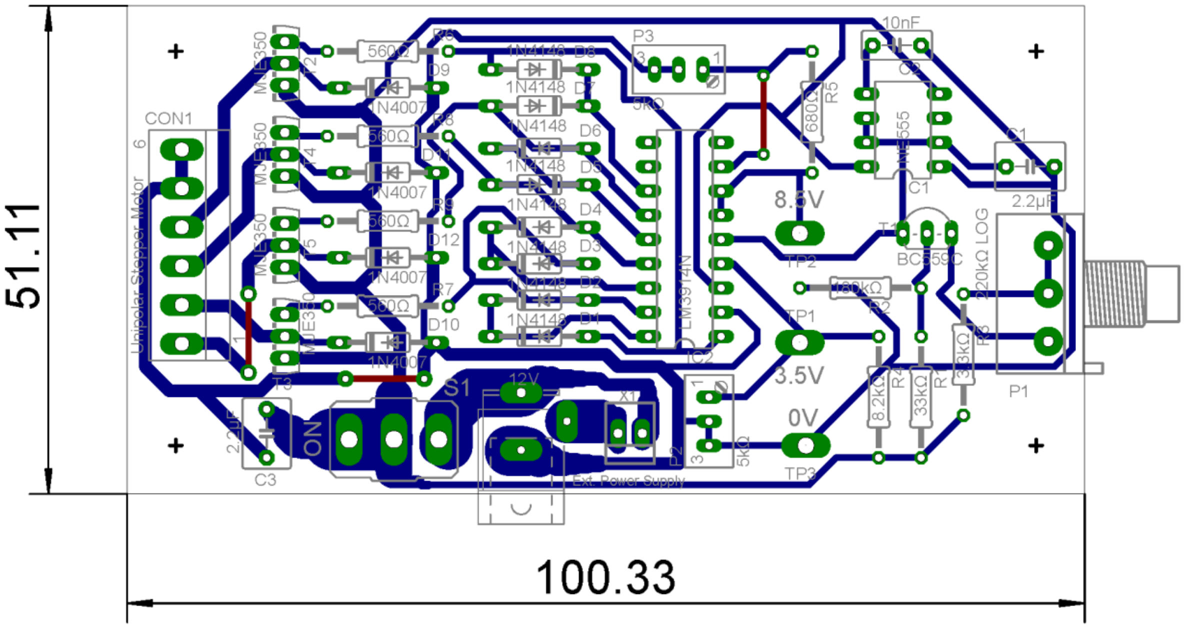

Figure 3.5: PCB picture from the CAD program. Dimensions are in millimeters.

A copper board having the same dimensions indicated in Figure 3.5 was mastered with a Press n Peel sheet, then it was etched with ferric chloride. After the drilling and the silkscreen transfer operations, the PCB appears as showed in Figure 3.6 (a) and (b).
The final PCB, after the components soldering operation, is shown in Figure 3.7; the components part list is reported in Table 3.4.

Component	Name (Figure 3.6 (b))	Value
Resistors	R1	33 kΩ
	R2	180 kΩ
	R3	3.3 kΩ
	R4	8.2 kΩ
	R5	6.8 kΩ
	R6 to R9	5.6 kΩ
	P1	220 kΩ, Logarithmic
	P2, P3	5 kΩ, Multiturn trimmer
Capacitors	C1, C3	2.2 μF, polyester
	C2	10 nF, polyester
Diodes	D1 to D8	1N4148
	D9 to D12	1N4007
Medium-power transistors	T1 to T5	MJE350
Integrated circuits	IC1	NE555
	IC2	LM3914N
Various components	S1	Slide switch
	12V	Power supply jack
	CON1	Stepper motor connector
	X1	Header pin
	TP1…TP3	PCB test point
	M1	North American Philips control corp. Unipolar stepper motor mod. A82747 (12 V, 300 mA, 300 PPS, 375 RPM, 7.5°)

Table 3.4: PCB components part list.

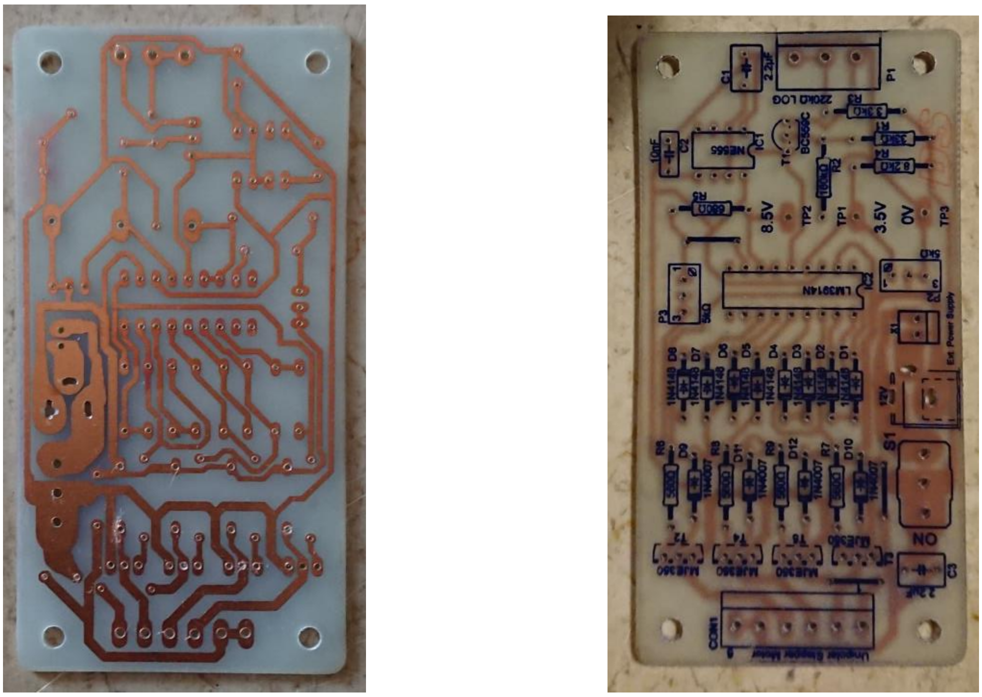
(a) (b)

Figure 3.6: PCB Copper (a) and components (b) side.

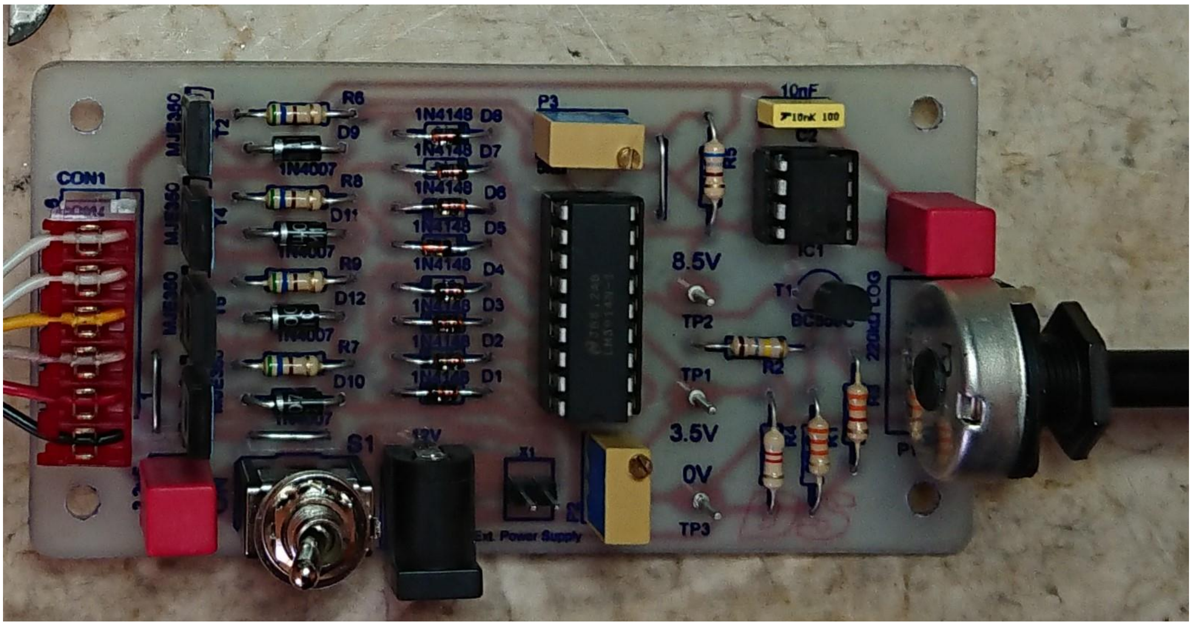
Figure 3.7: Mounted PCB.

The board in Figure 3.7 was then tested before its package assembly, done with a Gewiss junction box (Figure 3.3). The circuit arranged inside the box after its drilling and cutting phases is showed in Figure 3.8 (a) and (b).

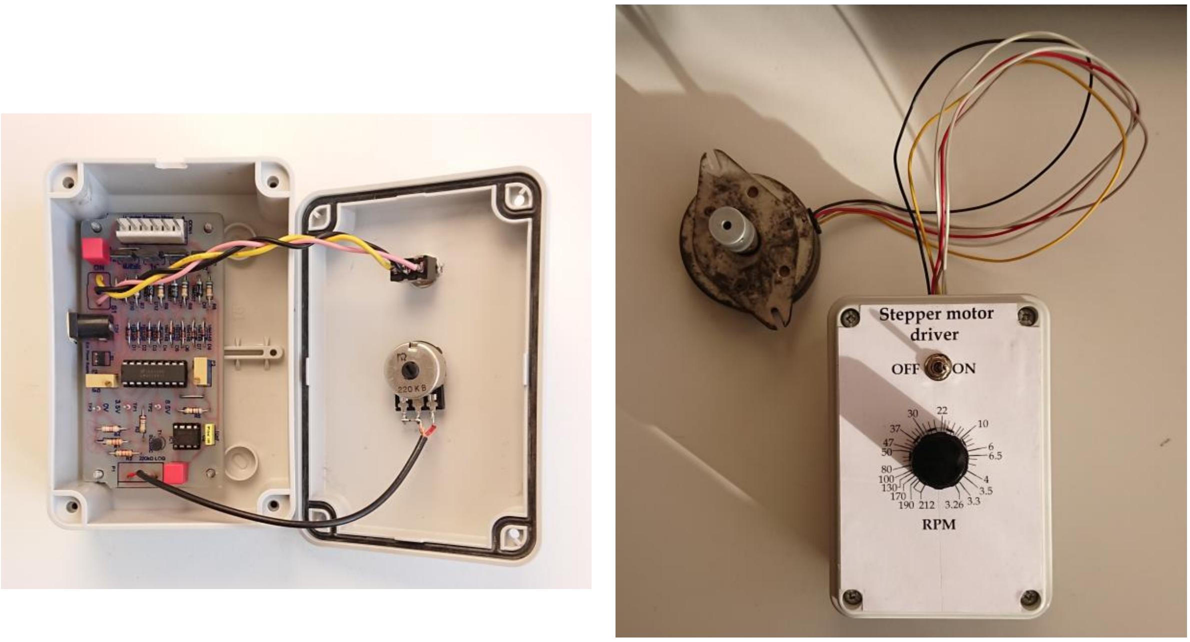

(a) (b)

Figure 3.8: The realized PCB inside the junction box (a) and the package final result (b).

3.3.4 Circuit adjustment and motor speed computation

As already described in section 3.3.2, the reference voltages $\mathrm{V}_{\mathrm{RLO}}$ and $\mathrm{V}_{\mathrm{ref,out}}$ of the IC2 internal comparator chain needs to be adjusted. With regard to Figure 3.7, it must act on P1 and P2 trimmers, following this simple procedure:

1. If connected, disconnect the stepper motor unplugging the CON1 connector;
2. Turn the circuit on sliding the S1 switch;
3. Connect a voltmeter between the test points TP3 (ground) and TP1; the voltmeter must have an high input impedance ($\geq 20\ \mathrm{k}\Omega$) and at least $10\ \mathrm{mV}$ resolution.
4. Turn the P2 trimmer screw until the voltage read on the voltmeter display equals the one indicated on the silkscreen for the TP1, namely $3.50\ \mathrm{V}$;
5. Repeat the steps 3 and 4 changing the TP1 test point into TP2.

The sawtooth oscillator frequency after the adjustment procedure was measured with an Agilent Infiniii Vision MSO 7054A oscilloscope. The minimum and maximum measured frequency are:

$$f_{min} = 670\ mHz \tag{3.27}$$

$$f_{max} = 42.7\ Hz \tag{3.28}$$

From the oscillator frequency, knowing that for each period the motor receives eight pulses, it is possible to compute the value of revolutions per minute (RPM). The used formula was taken from [65]:

$$RPM = \frac{PPS \cdot 60s \cdot \frac{\alpha^\circ}{2}}{360^\circ} \tag{3.29}$$

where α° is the motor step angle, and PPS is its number of Pulses Per Second driving the motor. In this circuit the number of pulses for each period is 8, while the α° angle is halved because of the half-step driving. Therefore, the number of RPM is related to the oscillator frequency with the formula (3.30):

$$RPM = \frac{f_{osc} \cdot 8 \cdot 60s \cdot \frac{\alpha^\circ}{2}}{360^\circ} = \frac{f_{osc} \cdot 2s \cdot \alpha^\circ}{3^\circ} \tag{3.30}$$

It is now possible to compute the minimum and maximum value for the revolutions per minute, namely $\mathrm{RPM}_{\mathrm{min}}$ and $\mathrm{RPM}_{\mathrm{max}}$, substituting the (3.27) and (3.28) in the (3.30) relationship:

$$RPM_{min} = \ 3.35\ RPM \tag{3.31}$$

$$RPM_{max} = 213.5\ RPM \tag{3.32}$$

The formula (3.30) was also used to draw the graduated scale in showed in Figure 3.8 (b).

3.4 Coaxial waveguide samples

As explained in section 2.1.5, in order to test a new material with the ASTM D4935 standard [20], two specimens are required: the reference specimen and the load specimen (see Figure 3.9). The sample thickness must be smaller (<1/100) than the electrical wavelength of the field transmitted inside the specimen [20]; however, the specimen thickness was chosen to be 1 mm, because thinner composite disks would be deformable, while thicker specimens would not allow an efficient signal transmission between the two flanges [20].

3.4.1 Realization procedure

The first realized sample was the central part of the reference specimen, hence the small disk in Figure 3.9. To obtain an epoxy resin disk having 33.02 mm diameter [20], and 1 mm thickness, a silicone mould was properly realized. The resin was casted inside the mould, then covered with a silicone lid, and left cured for 36 hours at 22°C room temperature.

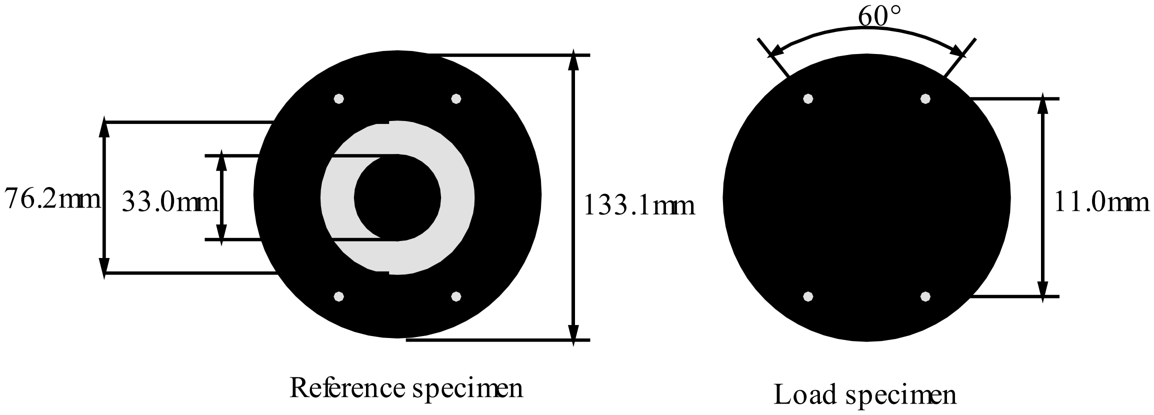

Figure 3.9: Reference and load specimens draw according to the ASTM D4935 standard [20].

With the described procedure eight samples (see Figure 3.10), were realized. After the curing time, their thickness and diameter were measured, to test the repeatability of the realization procedure. Measurements reported in Table 3.5 shows that every sample has a central thinning, caused by the major pressure the silicone lid exerts on its center, due to its weight. To solve this problem, a perfectly levelled surface must be used as lid, for instance a glass plate or a metallic plate. However, the epoxy resin can be covered only with a silicone lid, because this material (as well as the baking paper) is the only one that can be detached after the curing reaction.

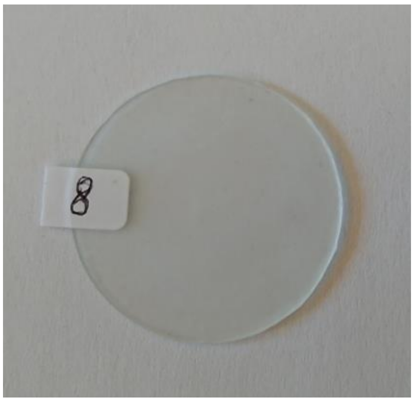

Figure 3.10: An example of epoxy resin disk after curing (sample number 8).

The Table 3.5 shows that the best result is 0.11 mm maximum difference in thickness between the disk center and its periphery. The ASTM D4935 adopted standard requires that the maximum variation in average thickness within the specimen must be less than 5% [20], hence the described specimen preparation method cannot be used to realize samples complying with this measurement standard. For this reason, the only measurements reported in the 4.1

subsection are the ones related to the characteristic impedance of the coaxial waveguide, to be made in a preliminary phase as recommended in [20].

Sample number	Average Diameter (mm)	Average thickness (mm)	Central thickness (mm)	Thickness variation (mm)
1	33.40	1.16	1.05	0.11
2	33.30	1.19	1.11	0.08
3	33.45	1.30	0.43	0.87
4	33.28	0.92	0.75	0.17
5	33.59	1.07	0.97	0.96
6	33.34	0.98	0.63	0.35
7	33.31	0.80	0.20	0.60
8	33.40	0.98	0.72	0.26

Table 3.5: Dimensions of the realized samples.

3.5 Rectangular waveguide samples

All the tested specimens had a parallelepiped shape, realized to fit the inner walls of a waveguide spacer, as described in the 2.1.6 sub-section. To measure the specimens, they were press fitted inside the spacer; then the spacer was inserted in the measurement setup described in the 4.2 subsection. Two measurement setups were realized and described in this subsection: one with the WR90 waveguide, and another one with the WR137 waveguide. For both waveguides, the samples thickness was primarily chosen to be $4\ \mathrm{mm}$ and $8\ \mathrm{mm}$, to have a good mechanical stresses resistance. The physical properties of the realized composites, in fact, are very similar to the ones of the pristine epoxy resin. These two thickness values were than maintained because the preliminary shielding effectiveness of the pristine samples was measured to be very low (few dBs).

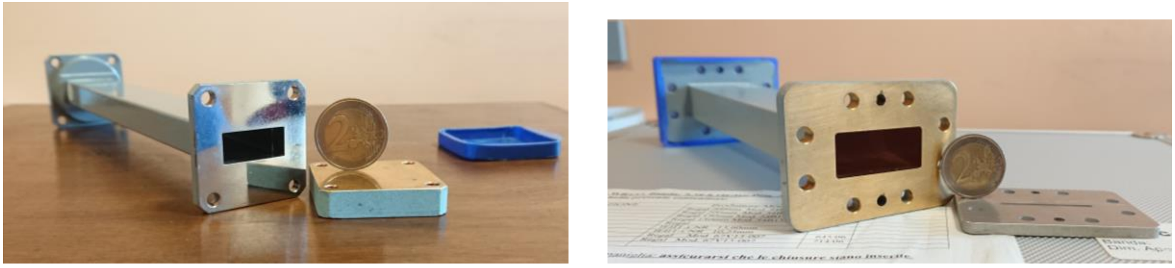
(a) (b)

Figure 3.11: The used WR90 flange (a) and WR137 waveguide.

The specimens rectangular cross-section dimensions are the same of the used waveguides, hence $(22.86 \text{ x } 10.16)$ mm for the WR90 waveguide and $(34.8488 \text{ x } 15.7988)$ mm for the WR137 specimens. The dimension tolerance, according to the MIL standard, is 0.1016 mm for each waveguide. An aperture dimension estimation for both waveguides is provided in Figure 3.11.

3.5.1 Realization procedure

The rectangular waveguide composite specimens were realized with a procedure very similar to the one already described in the 3.4.1 subsection for the ASTM coaxial holder. The epoxy resin composite was prepared according to the procedure described in the 3.1.1 subsection, than it was casted inside a properly designed silicone mould, hence left cured for about 36 hours.

The specimens realization procedure used for the ASTM coaxial holder were improved, allowing for the realization of samples whose physical dimensions tolerances are schematized in Table 3.6.

Specimen width	Specimen height	Specimen thickness
22.86 mm, $\pm 6.6\%$	10.16 mm, $\pm 1.8\%$	4 mm, $\pm 20\%$

Table 3.6: Physical dimensions and their variations for the 35 realized specimens.

From this table it can be noticed that the samples dimensions variation are smaller than the waveguide physical tolerances, hence this method was used also for the realization of WR137 waveguide samples.

Six of the realized $4\ mm$ thickness pristine samples were coated with the composites described in the 3.2 subsection. The specimens appearance after the deposition procedure is showed in Figure 3.12.

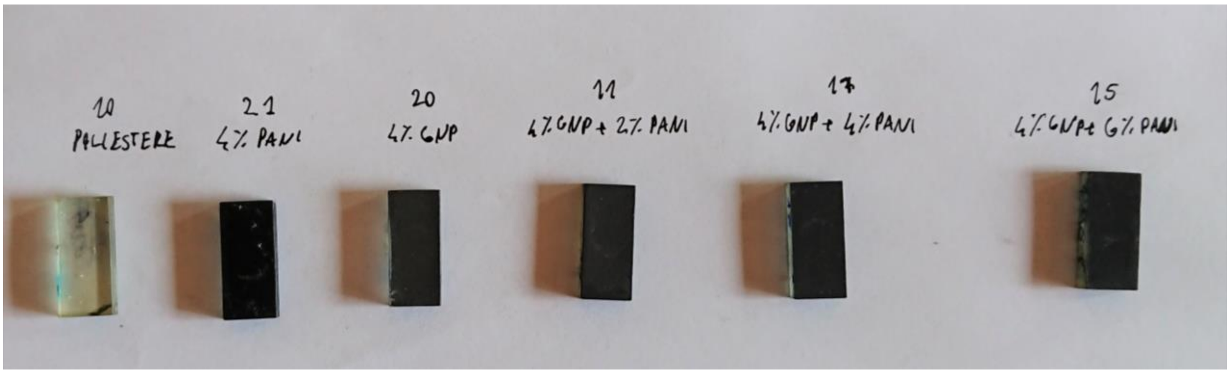

Figure 3.12: The epoxy resin 4 mm specimens after the coating deposition.

Chapter 4

Measurement Results

The composite materials, widely described in Chapter 3, were characterised in the C band with a WR137 waveguide test bench, and in the X band with a WR90 waveguide setup. The realized measurement setups and the measurement results are described in this chapter, together with the coaxial waveguide impedance evaluation. All the test benches were based on a Programmable Network Analyser (PNA) Agilent E8361A [66], having a working frequency range of 50 MHz to 67 GHz, suitable for the C and X bands. The acquired data were processed and plotted with a MATLAB® script.

4.1 Coaxial waveguide impedance measurement

In the 3.4.1 section the reasons why the composites were not tested with this test fixture were described. However, the ASTM D4935 standard requires that the coaxial cable characteristic impedance must be verified prior to make every specimen measurement.

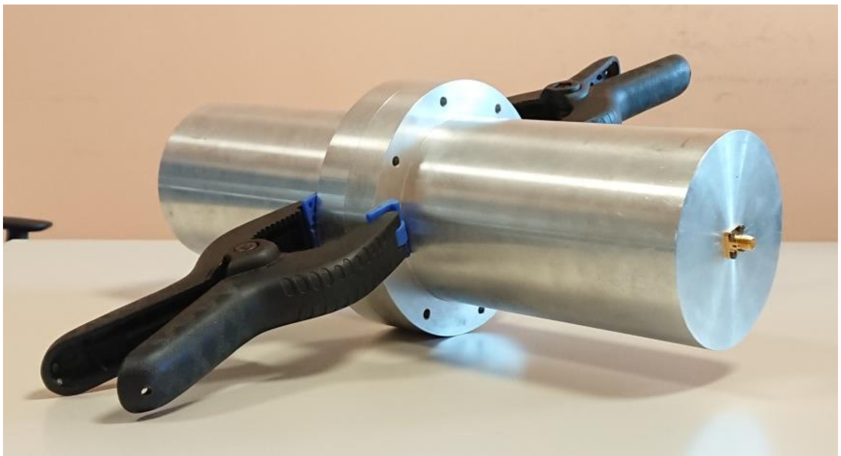

Figure 4.1: The coaxial cable prepared for the characteristic impedance measurement.

The two test fixture halves were cleaned with ethyl alcohol and paired with two spring clamps, as highlighted in Figure 4.1, then the S parameters of the entire coaxial cable were measured. The ASTM standard prescribes a measurement range of 30MHz ÷ 1.5GHz [20]; however, since the lower measurable frequency of the used network analyser is 50MHz, the adopted measurement range is 50MHz ÷ 1.5GHz.

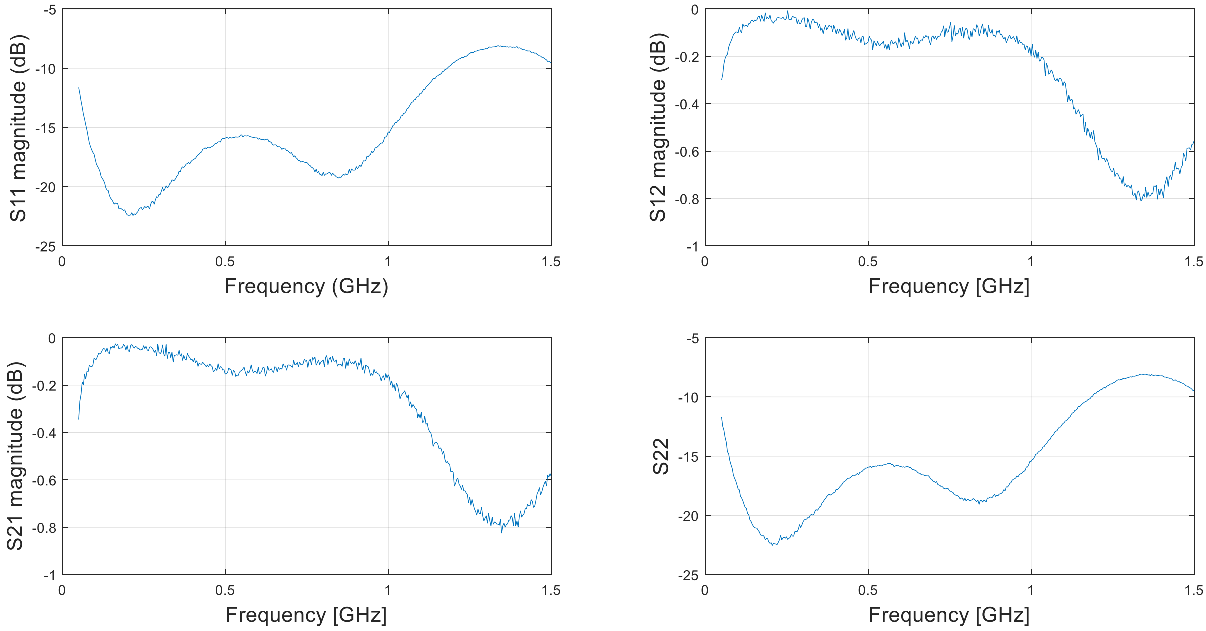

Figure 4.2: Rectangular plot of measured S parameters.

The measured S parameters were than processed with a MATLAB® script, to extract the coaxial waveguide characteristic impedance; the four S parameters were also plotted, either in polar form and Smith chart graph. In Figure 4.2 the real part, the imaginary part and the absolute value of the 2-port S parameters are showed. Since the measured device is reciprocal and symmetric, in Figure 4.3 the S_{11} and S_{12} parameters only are reported in a Smith chart graph. The expected S_{11} plot is a spot positioned exactly on the smith chart center; the obtained graph spiral suggests that the impedance of the coaxial cable is not exactly 50 Ω in the measured frequency range. The transmission coefficient S_{21} (equal to the reported S_{12}) instead, is like expected, showing a small amount of losses due to the transmission line non idealities.

The computed characteristic impedance is plotted in Figure 4.4. As expected from the S_{11} plot, there are three resonances, highlighted by the absolute value impedance peaks. As consequence, the characteristic impedance is not constant in the measured frequency range, although outside the peaks it tends to the 50 Ω ideal value.

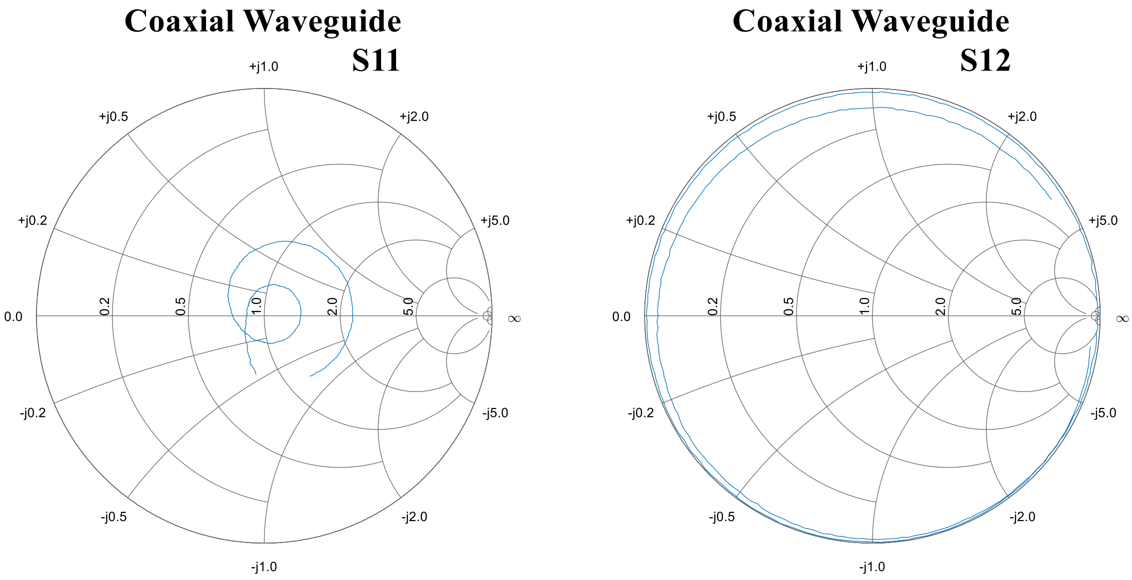

Figure 4.3: Smith chart plot of S_{11} and S_{12} parameters.

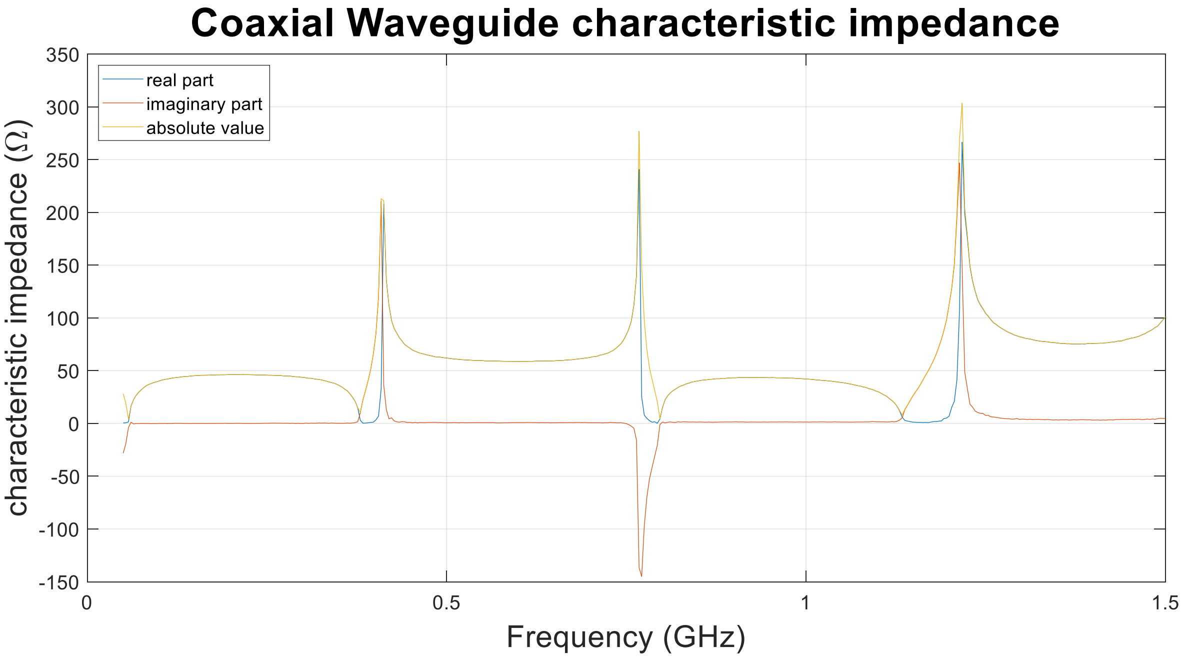

Figure 4.4: Computed characteristic impedance starting from the measured S parameters.

4.2 Rectangular waveguide measurements

In this section the procedure for obtain the specimens scattering parameters, either with the WR90 and WR139 waveguides, is described. The measurement basic principles of this method are described in section 2.1.6, and are not reported here; the setup schematic view only is repeated, in Figure 4.5, for the sake of clarity. Each network analyser port was wired with the waveguides right angle launchers (RAL) through a couple of Teledyne Accu-Test® calibration coaxial cables. To obtain a correct TE_{10} mode excitation inside the waveguide, two waveguide straight pieces, having equal length, were inserted between the launchers and the measured sample. Since the specimens were press-fitted inside the waveguide, it was unpractical to insert them in a straight piece; hence, a waveguide spacer, having thickness higher than the specimen thickness, was used. Finally, for each frequency band, a proper calibration kit was deployed. Since the spacer length and losses were not taken into account by the calibration correction, the shielding effectiveness was computed with the insertion loss definition (2.2) with both waveguide setups.

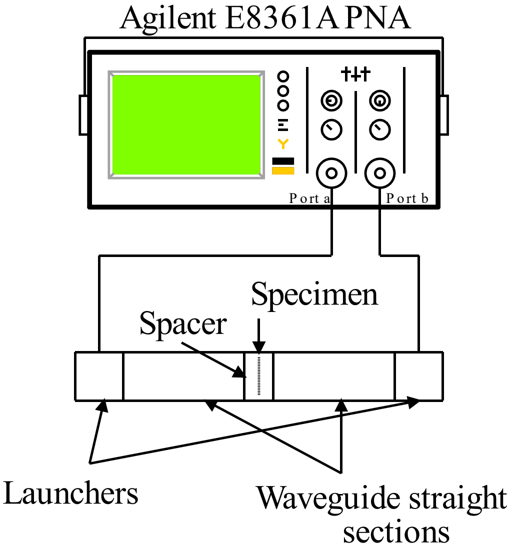

Figure 4.5: Schematic view of the measurement setup used for the WR90 and WR139 waveguides.

4.2.1 WR90 measurement setup

The X band measurements were done with a Maury Microwave X7005E calibration kit, shown in Figure 4.6. This kit was designed to perform an SSLT (Short-Short-Load-Thru) calibration, not supported by the used PNA; moreover, the classical TRL (Thru-Reflect-Match) calibration could not be done with the deployed kit. A valid alternative to the very popular TRL calibration is the **TRM (Trhu-Reflect-Match)** variant. In this calibration technique, the 12-terms error matrix is computed by measuring a matched load instead of a piece of line having known length. This calibration is then a degenerate case of the TRL calibration, where an infinite-length piece of line (the matched load) is measured [67]. The need to measure a short circuit, a matched load and a port thru, makes this calibration technique a very similar to the SOLT calibration, without the open standard.

Figure 4.6: The used Maury Microwave calibration kit [68].

An example of the tested specimen press-fitted in the brass $10\ \mathrm{mm}$ waveguide spacer is shown in Figure 4.7 (a) and (b). The measurement setup in Figure 4.8 was assembled with the described calibration kit, the spacer and two $20\ \mathrm{cm}$ waveguide straights. The PNA measurement frequency range was the same of the calibration kit, namely $(8.2 \div 12.4)$ GHz, divided into 801 points. The source power level was set to be $0\ \mathrm{dBm}$. A 15 samples average was activated.

(a)

(b)

Figure 4.7: Pristine specimen (a) and Biochar composite specimen (b) press fitted inside the waveguide spacer.

The acquired 2-ports S parameters were than post processed, as already discussed in the 2.1.6 section, with a MATLAB® script, to plot the S_{21} scattering parameter and to compute the shielding effectiveness of the tested specimens.

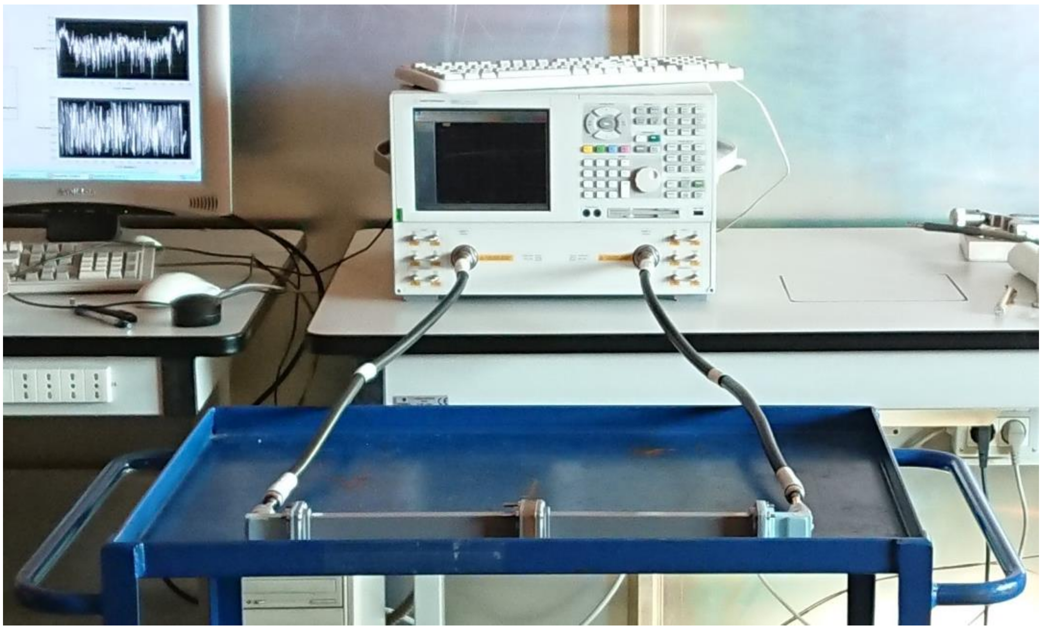

(a)

(b)

Figure 4.8: The realized WR90 measurement setup.

4.2.2 WR137 measurement setup

The Afzal's biochar-based composites were tested also in the C band with a WR137 waveguide setup. The PNA settings, the calibration coaxial cables and the specimens preparation procedure are the same used for the WR90 waveguide. The only difference is obviously the deployed calibration kit, realized by the IEIIT-CNR institute and shown in Figure 4.9. Its rated frequency range is $(5.38 \div 8.18)$ GHz.

Figure 4.9: The used IEIIT-CNR calibration kit.

In Figure 4.10 an example of two specimens press fitted inside the waveguide spacer is reported, while the realized WR137 measurement setup is presented in Figure 4.11.

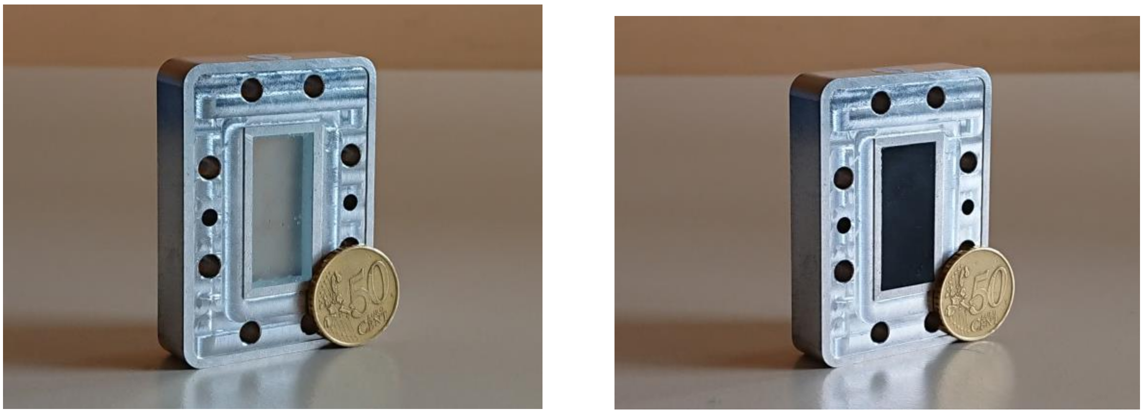

(a)

(b)

Figure 4.10: Example of a pristine specimen (a) and a Biochar specimen (b) press fitted inside the waveguide spacer.

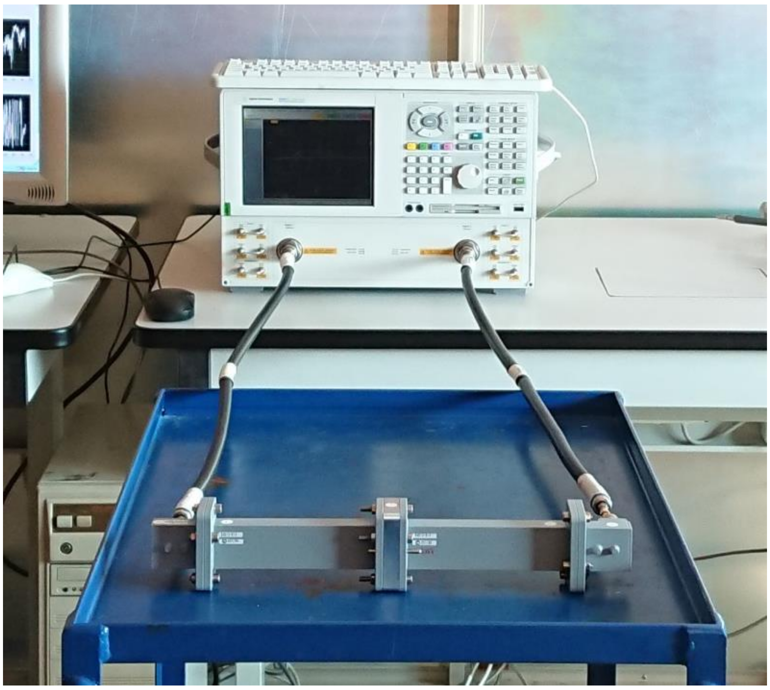

(a)

(b)

Figure 4.11: The realized WR137 measurement setup

4.3 Shielding effectiveness

With the measurement setups described in the 4.2 subsection the 2-port scattering parameters of each specimen were measured; the shielding effectiveness was then computed according to the (2.2) equation, here recalled:

$$SE_{E|dB} = |S_{21}|_{dB} - |S_{21|spec}|_{dB} \tag{4.1}$$

where S_{21} is the transmission coefficient measured without the sample inserted, while $\mathrm{S}_{21|\mathrm{spec}}$ represents the transmission coefficient with the specimen press fitted inside the waveguide spacer. Since the S_{21} scattering parameter only was accounted in the presented measurements, it is reported together with the shielding effectiveness measures.

As described in Chapter 3, all the realized composites were based on a Hexion epoxy resin, used as matrix. This material was hence measured first, in order to evaluate the shielding effectiveness of the dispersed biochar and the deposed composites. The samples made with the epoxy resin only, (Figure 4.7 (a) and Figure 4.10 (a)) are called pristine samples.

4.3.1 WR90 measurements

Pristine samples

The WR90 measured transmission coefficient and shielding effectiveness of the 14 realized pristine specimens, having $4\ \mathrm{mm}$ thickness, are showed in Figure 4.12 and Figure 4.13 respectively. The specimens without imperfections were compared to the ones with some air bubbles, or with an approximately $3\ \mathrm{mm}$ diameter bubble (called big bubble). These graphs show that the measured shielding effectiveness are overlapped in a $0.3\ \mathrm{dB}$ range value. The measurements of a $8\ \mathrm{mm}$ sample are also reported. The lower value of its shielding effectiveness is due to a resonance in the measured frequency range, as shows its reflection coefficient. Since this was a problem found in all the realized $8\ \mathrm{mm}$ composites, the $4\ \mathrm{mm}$ thick specimens were mainly studied in the X band.

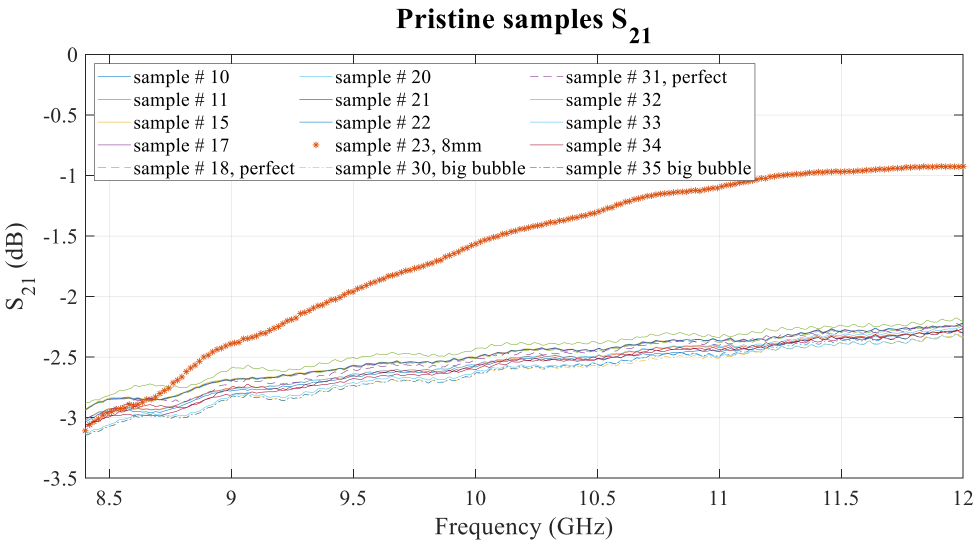

Figure 4.12: WR90 pristine samples S_{21} measurements.

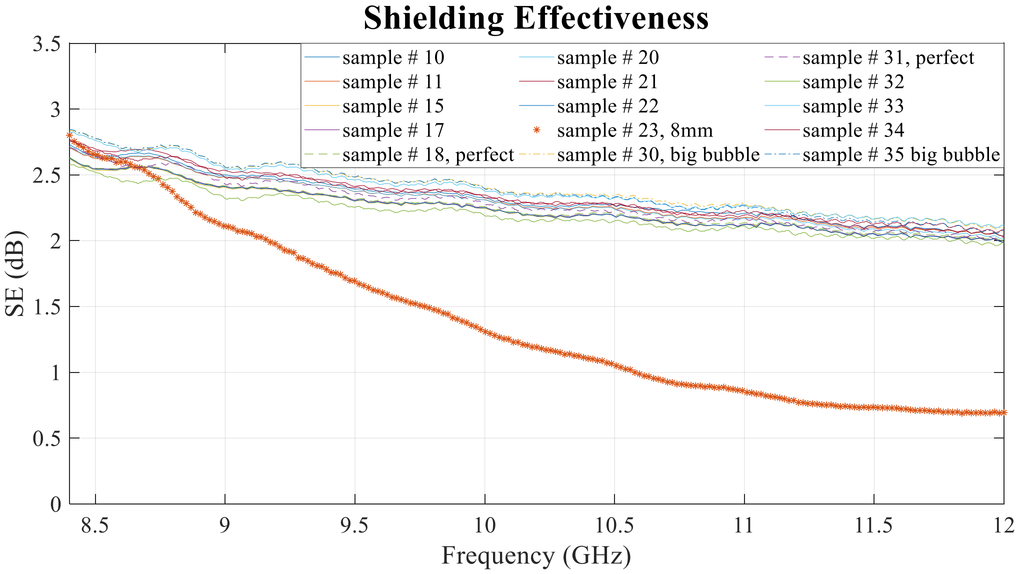

Figure 4.13: WR90 pristine samples shielding effectiveness measurements.

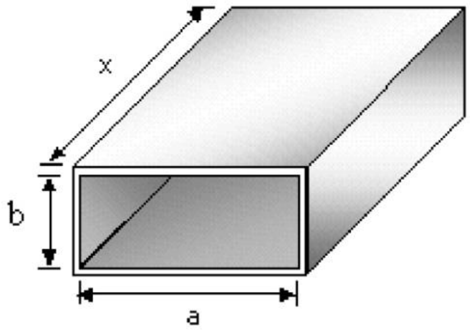

Figure 4.14: Rectangular waveguide cross section base (called ‘a’) and height (called ‘b’).

With referring to the Figure 4.14, the effects of the electric contact of the press fitted specimen with the waveguide walls were evaluated, exasperating the samples side imperfections by shaving off them with a metallic file. In Figure 4.15 the pristine specimen was firstly measured, then its ‘b’ side was shaved off. As can be seen, the two measurements are overlapped, because, as recalled in the 2.1.6 subsection, the magnitude of electric field lines is zero in a rectangular waveguide with the TE_{10} mode. The effect of the ‘a’ side shaving are, as expected, much more considerable than the ones obtained with the ‘b’ side shaving, as shows the Figure 4.16. In this figure, the measurement repeatability of the same sample was also evaluated, with the red trace completely overlapped on the blue trace.

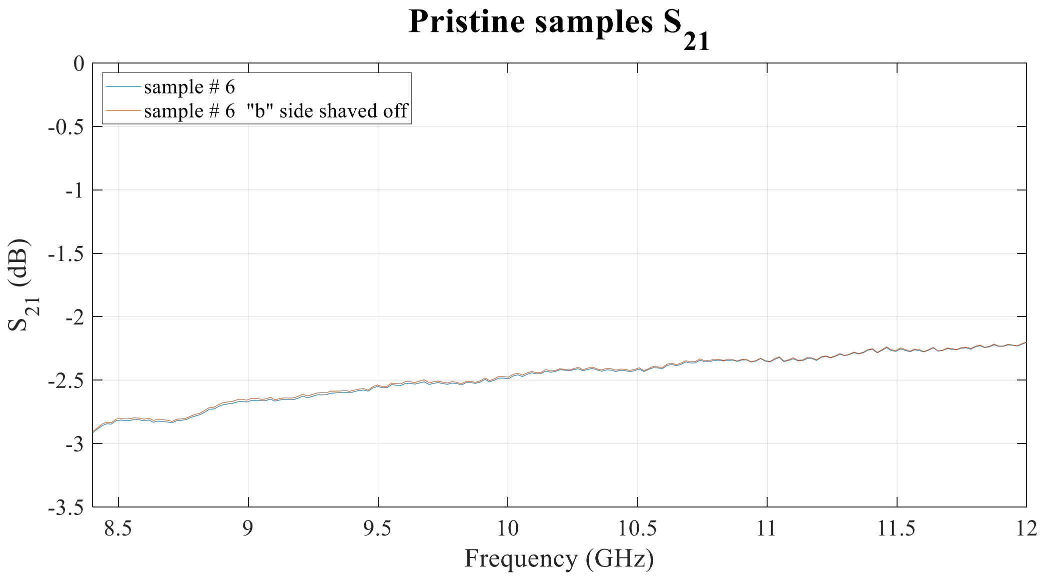

Figure 4.15: Differences between the pristine sample measurements and the same specimen with the ‘b’ side $0.5\ \mathrm{mm}$ shaved.

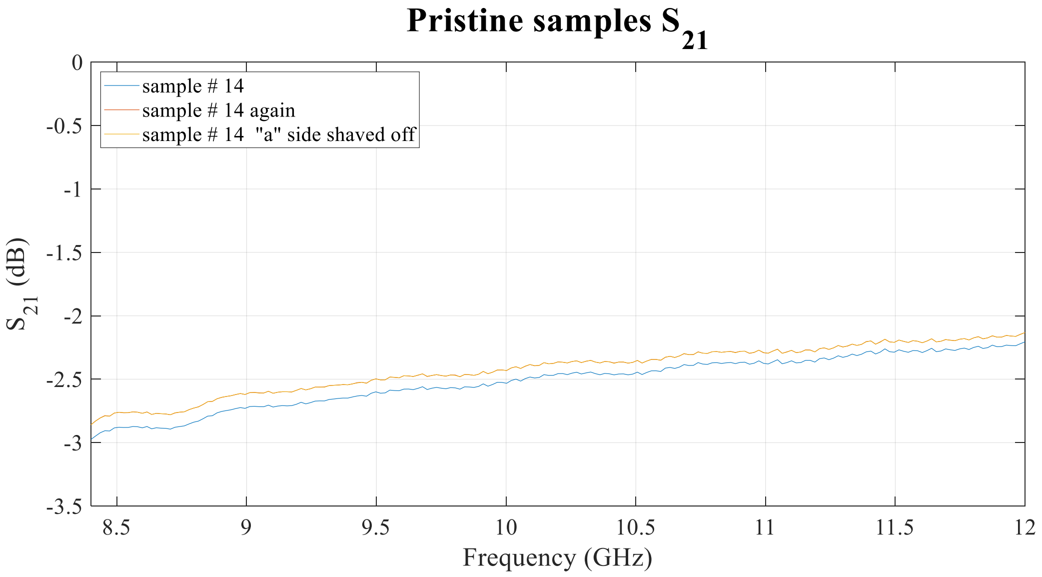

Figure 4.16: Differences between the pristine sample measurements and the same specimen with the ‘a’ side $0.5\ \mathrm{mm}$ shaved.

The effects of the ‘a’ side center defects are highlighted in Figure 4.17, where one ‘a’ side was firstly shaved on its center only (red trace), then both ‘a’ sides were center shaved off (yellow trace). This imperfection is much more noticeable than the others, due to the electric field lines distribution of the fundamental mode.

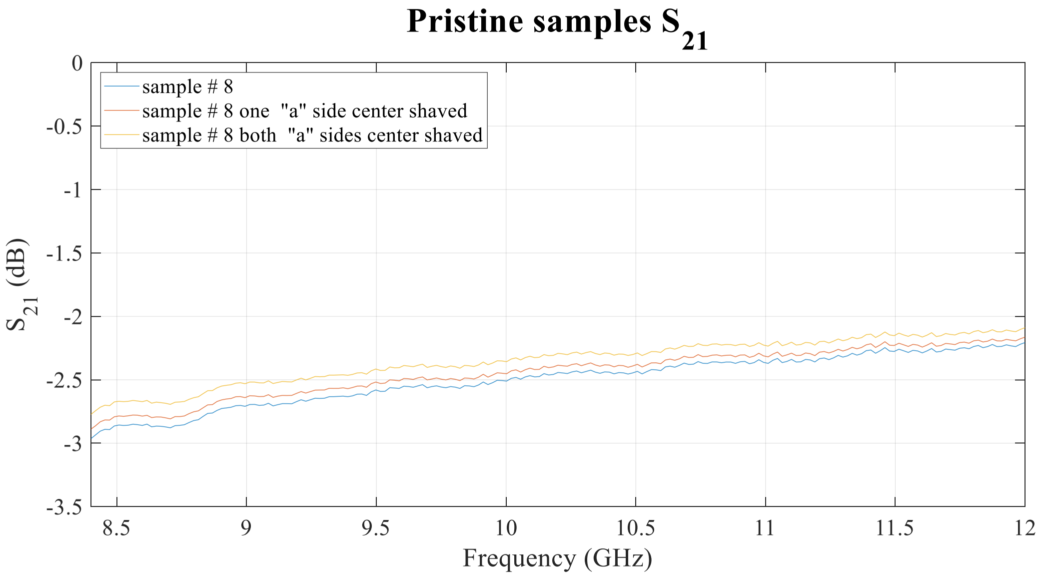

Figure 4.17: Effect of the ‘a’ side center shaving on the measured sample.

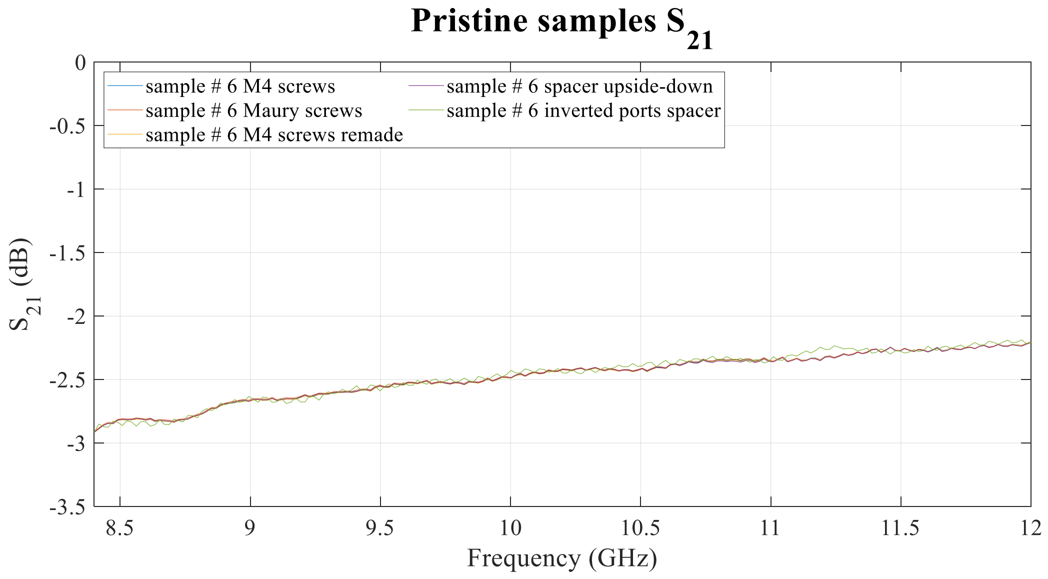

Figure 4.18: Waveguide to spacer alignment impact and spacer port inversion effect on the S_{21} measurements.

Finally, in Figure 4.18, the effects of different assemblies on the measurement setup are evaluated. The red and yellow traces simulate the waveguide straight-to-spacer alignment defects due to the use of standard M4 screws instead of the Maury screws, included in the calibration kit. As can be seen, these two traces are overlapped. The purple trace, which is measured inverting the spacer upside-down, is also overlapped to the other two traces. The only noticeable effect of the measurement setup is the spacer port inversion, as shown by the green trace.

Bioforcetech biochar composites

The result of all the reported evaluations is that a 0.3 dB error could be chosen to be the measurement tolerance, since the uncertainty due to the used PNA is lower than 0.3 dB [66]. Moreover, as it will be discussed, all the measured biochar composites are insulating, as well as the pristine samples, hence the contact impedance problem on the computed shielding effectiveness has the same order of magnitude. This was confirmed also by the measurements of the realized composites, either for the 4 mm and 8 mm specimens, made after two different calibrations, and reported in Figure 4.19.

The effects of the 3 mm diameter air bubbles is highlighted also for the Bioforcetech biochar in Figure 4.20, while the 10% and 20% shielding effectiveness of 4 mm specimens with this biochar are showed in Figure 4.21 (a) and Figure 4.21 (b) respectively.

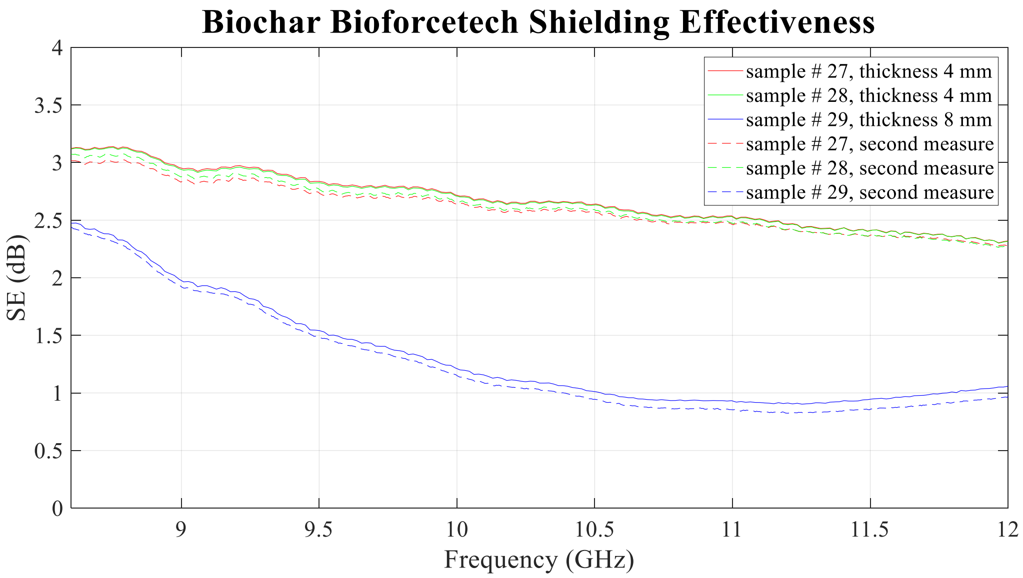

Figure 4.19: Repeatability of the specimens realized with the Bioforcetech biochar, with a 20% weight filler.

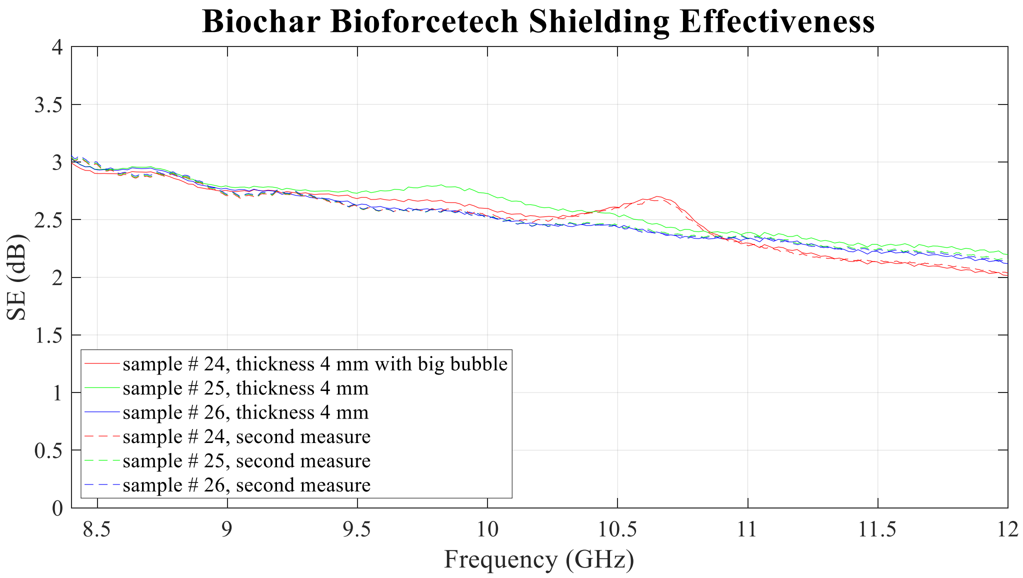

Figure 4.20: Shielding effectiveness repeatability on the 10% specimens.

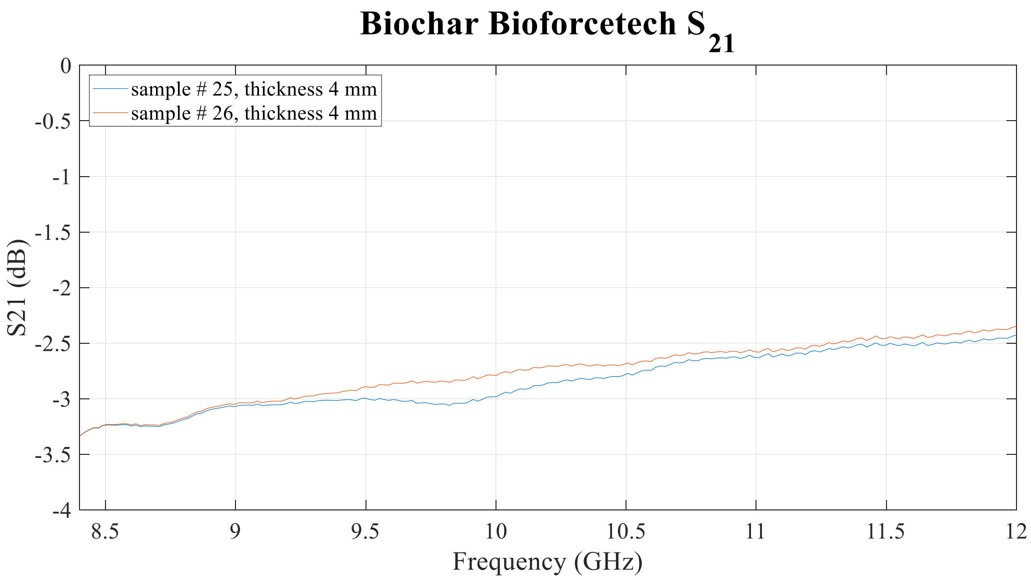

(a)

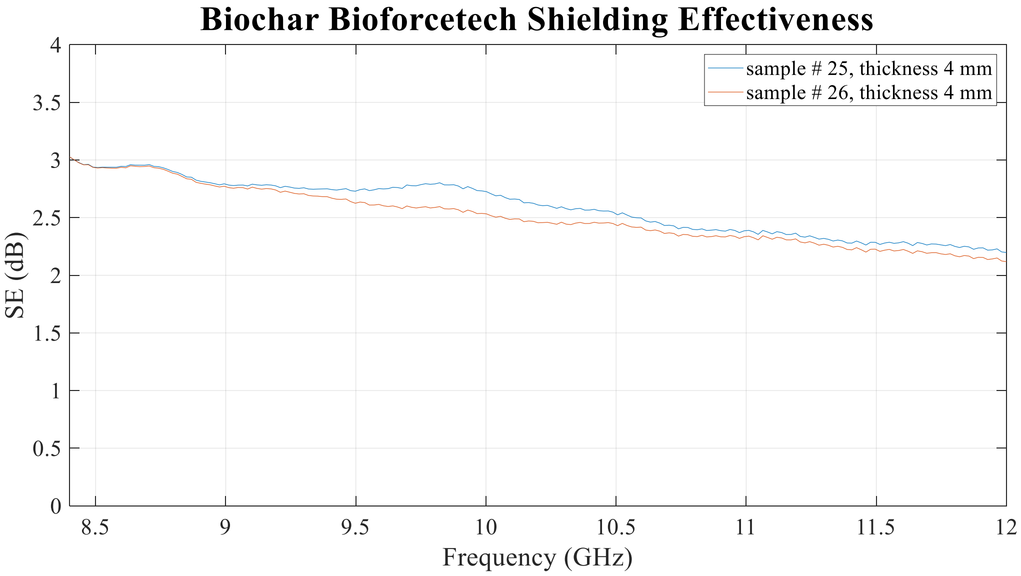

(b)

Figure 4.21: Bioforcetech biochar measurements with 10% filler concentration.

The 20% filler composite measurements, with the same biochar, are showed in Figure 4.22 (a) and Figure 4.22 (b) instead.

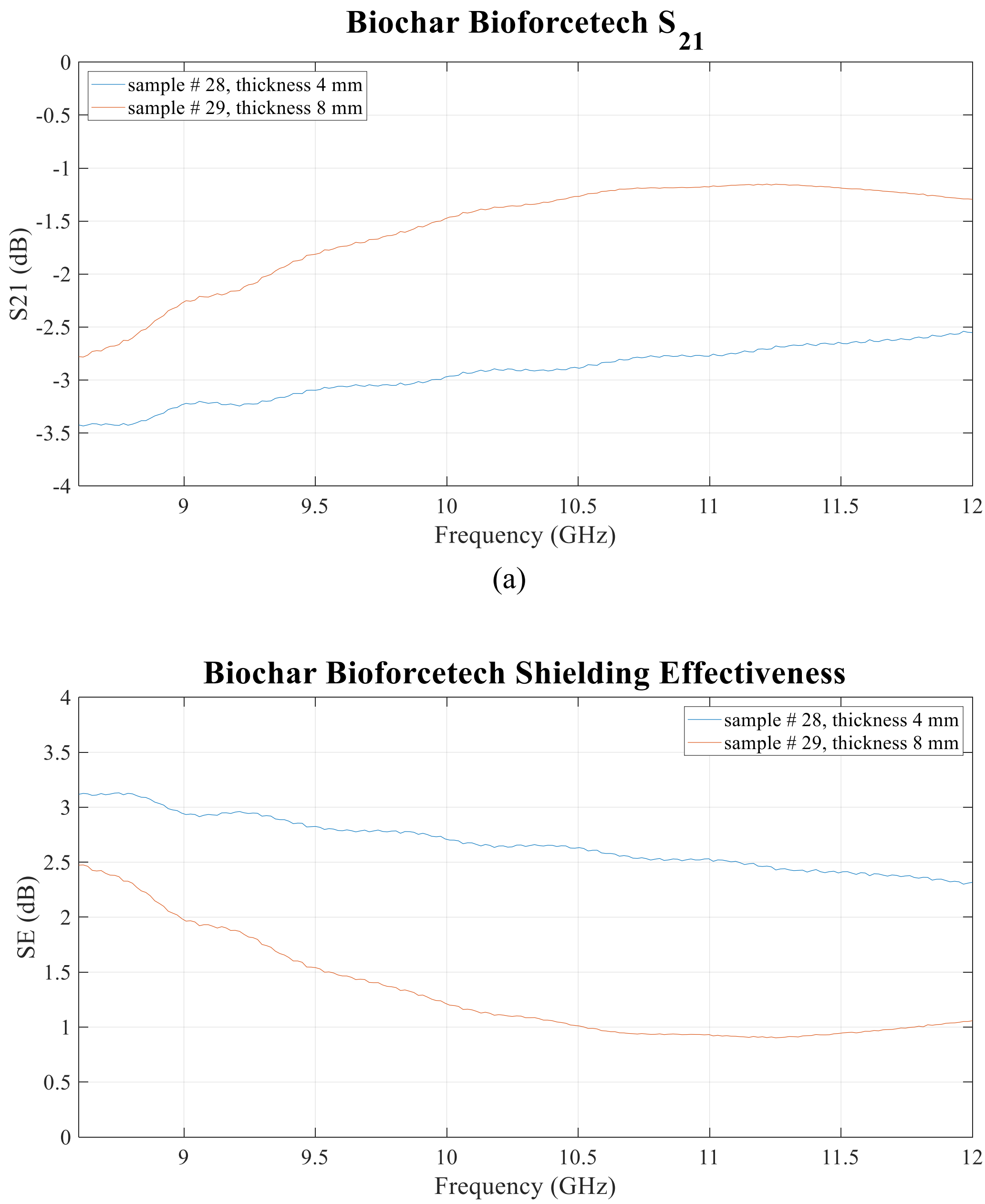

(a)

(b)

Figure 4.22: Bioforcetech biochar measurements with 20% filler concentration.

Two 4 mm thick samples having different Bioforcetech biochar concentration are showed in Figure 4.23. From this graph it could be noticed a slight shielding effectiveness increase (less than 0.3 dB) due to the filler concentration doubling.

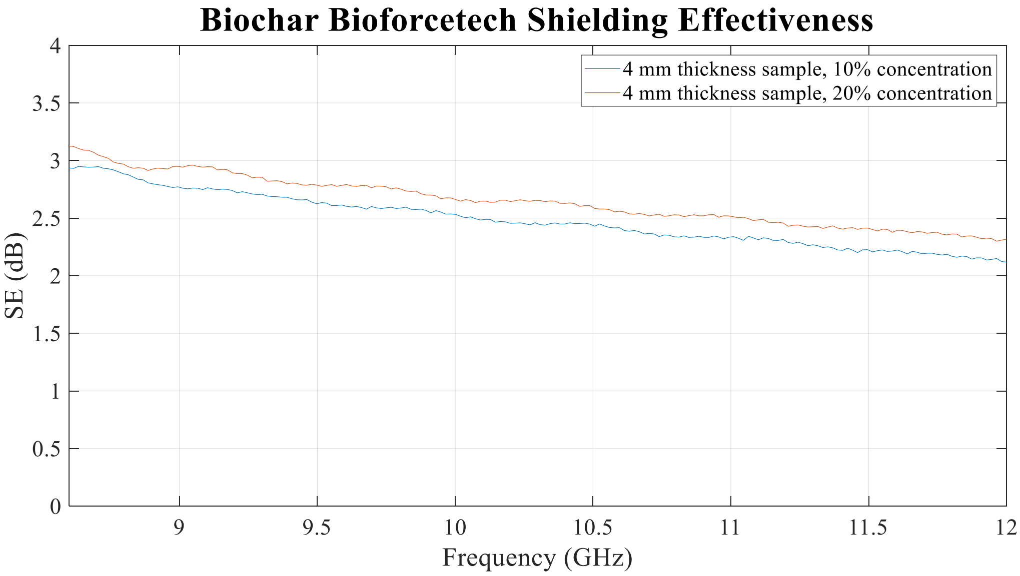

Figure 4.23: Effect of the Bioforcetech biochar filler concentration on two 4 mm specimens.

Afzal's Biochar composites

The measurements of the composites specimen based on the Afzal's biochar are reported in Figure 4.24 to Figure 4.29. Since, as exhaustively verified for the Bioforcetech composites, the measurements are repeatable, for each biochar type only one 4 mm thick specimen was realized; for the 20% filled composites, one 8 mm thick sample was also realized.
Also for these biochar based composites, the 8 mm thick specimens showed an unregular trend due to the already mentioned resonance.

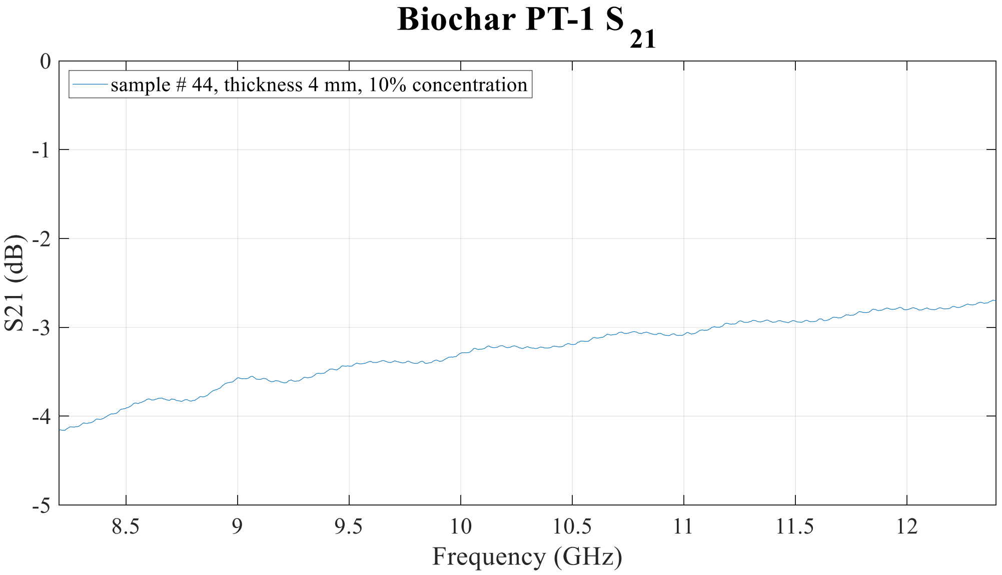

(a)

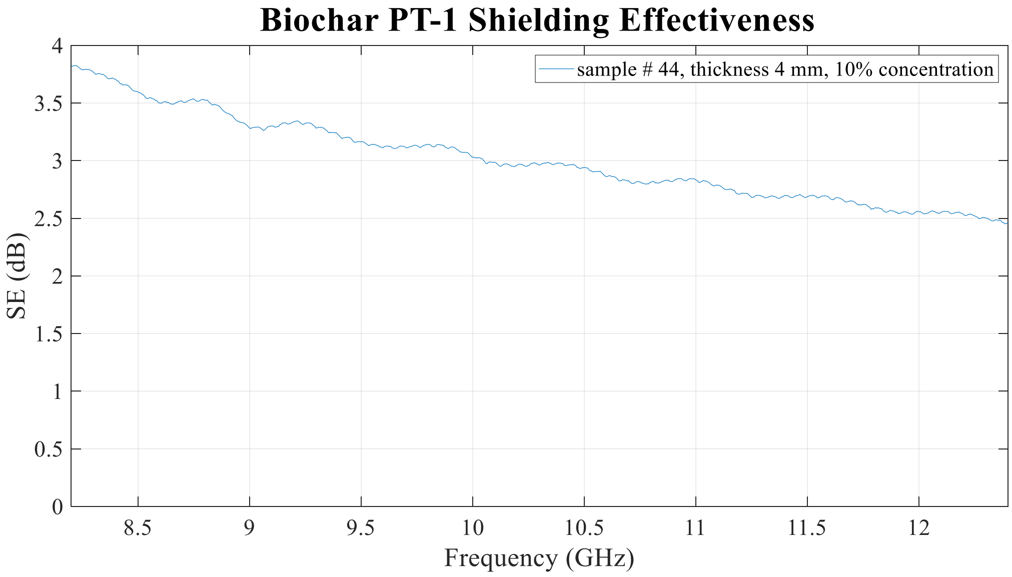

(b)

Figure 4.24: PT-1 biochar S_{21} (a) and shielding effectiveness (b).

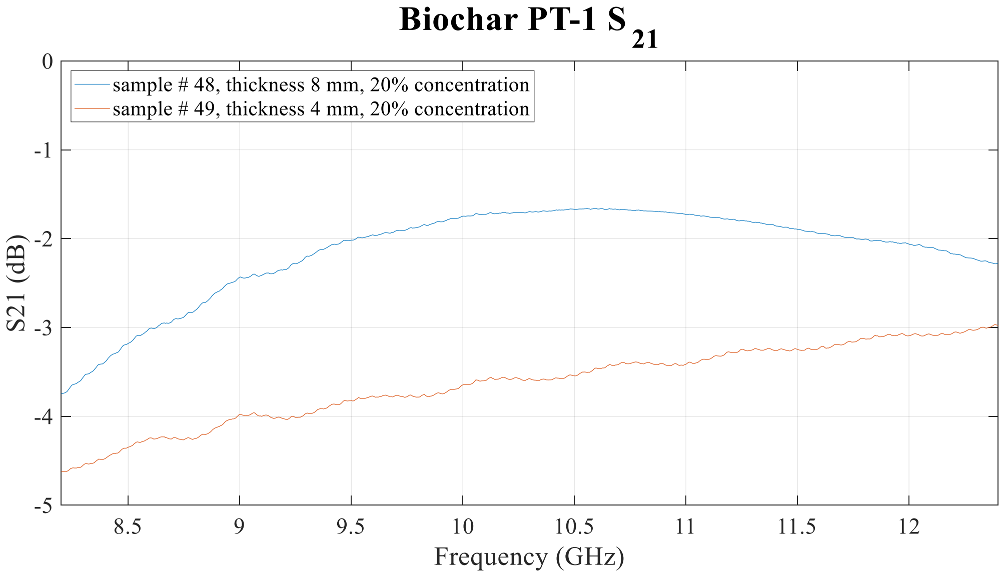

(a)

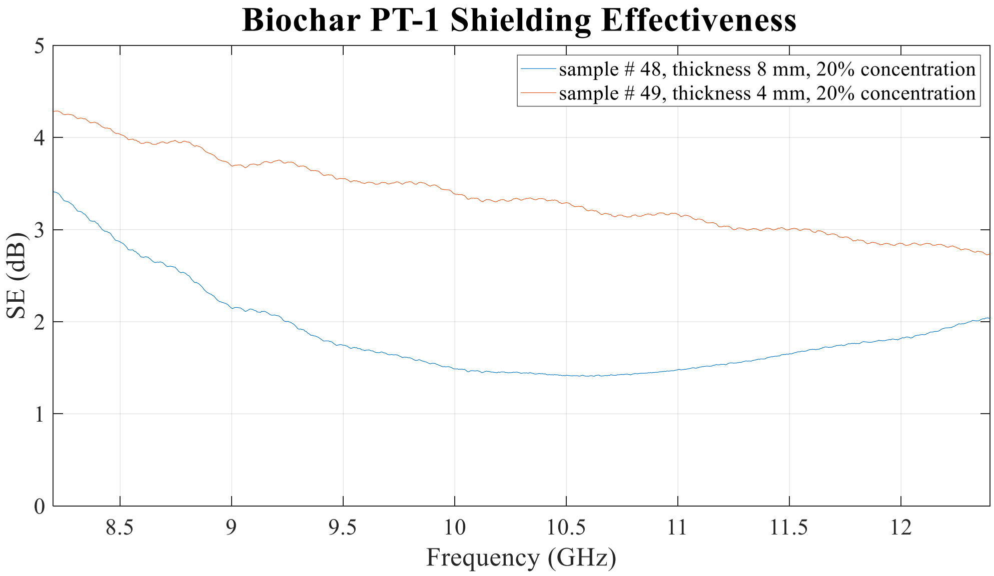

(b)

Figure 4.25: PT-1 biochar S_{21} (a) and shielding effectiveness (b).

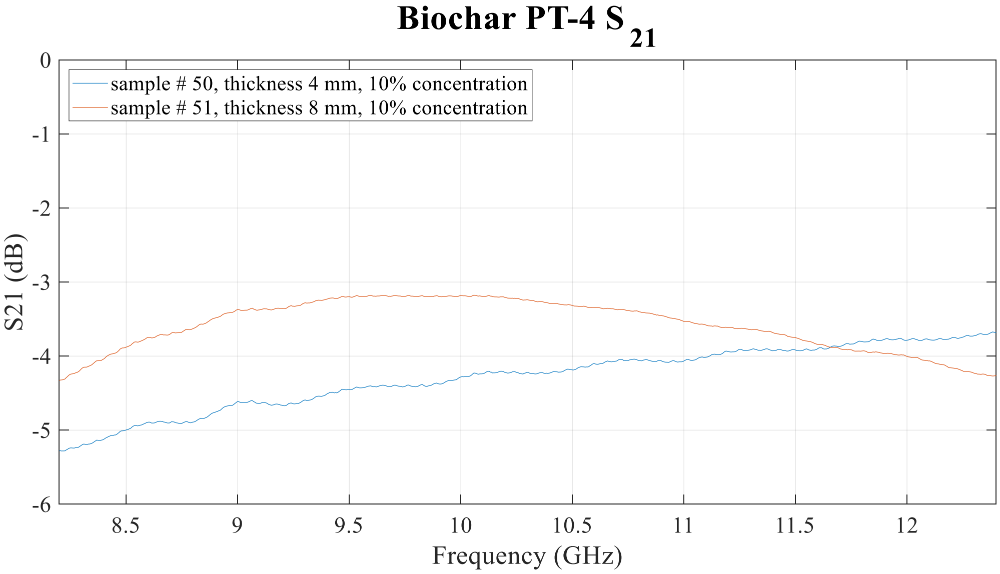

(a)

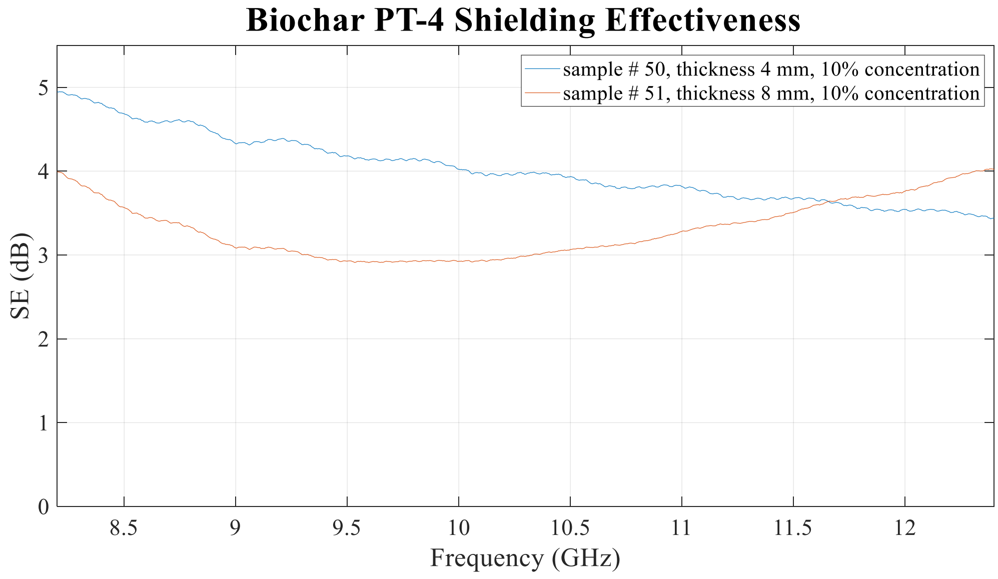

(b)

Figure 4.26: PT-4 biochar S_{21} (a) and shielding effectiveness (b).

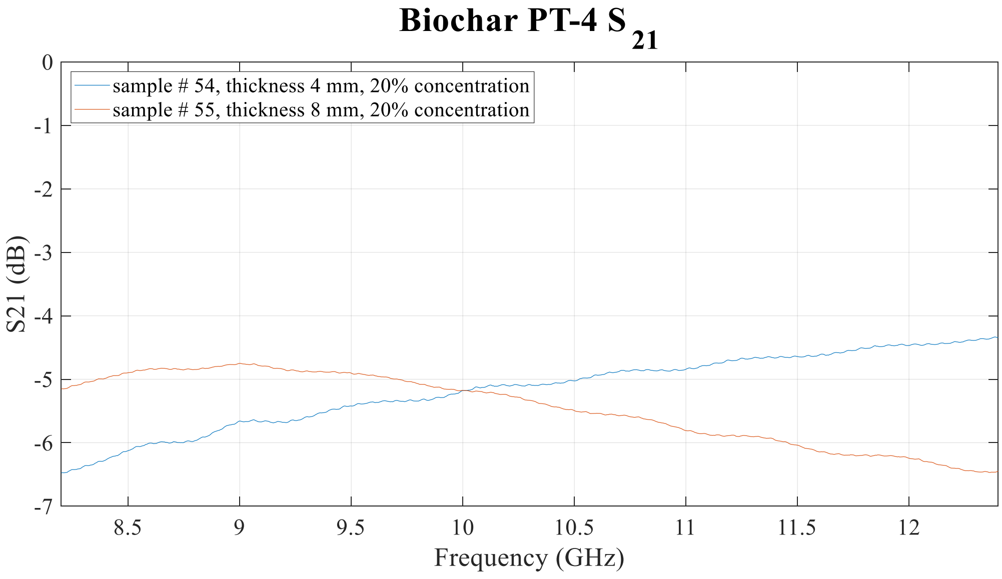

(a)

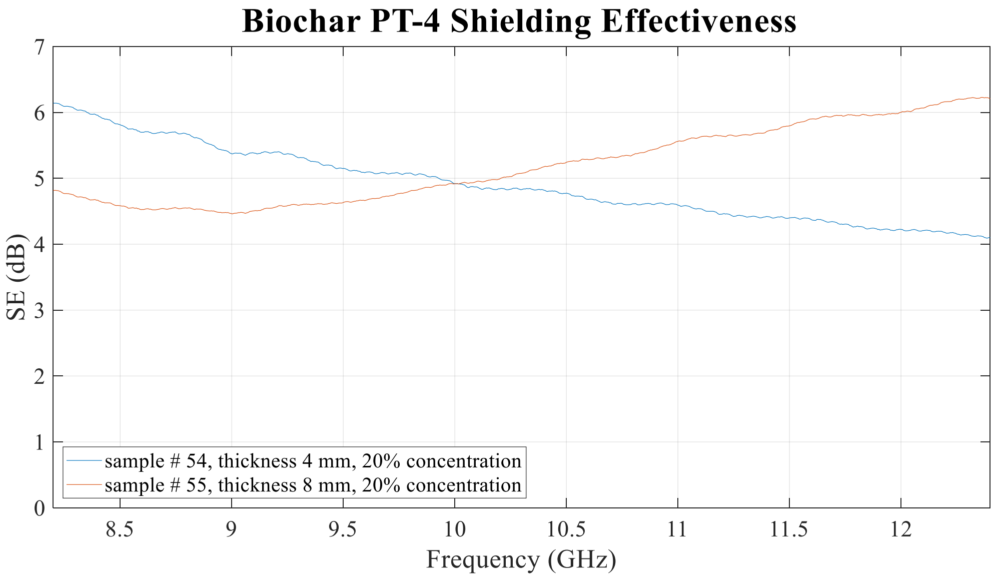

(b)

Figure 4.27: PT-4 biochar S_{21} (a) and shielding effectiveness (b).

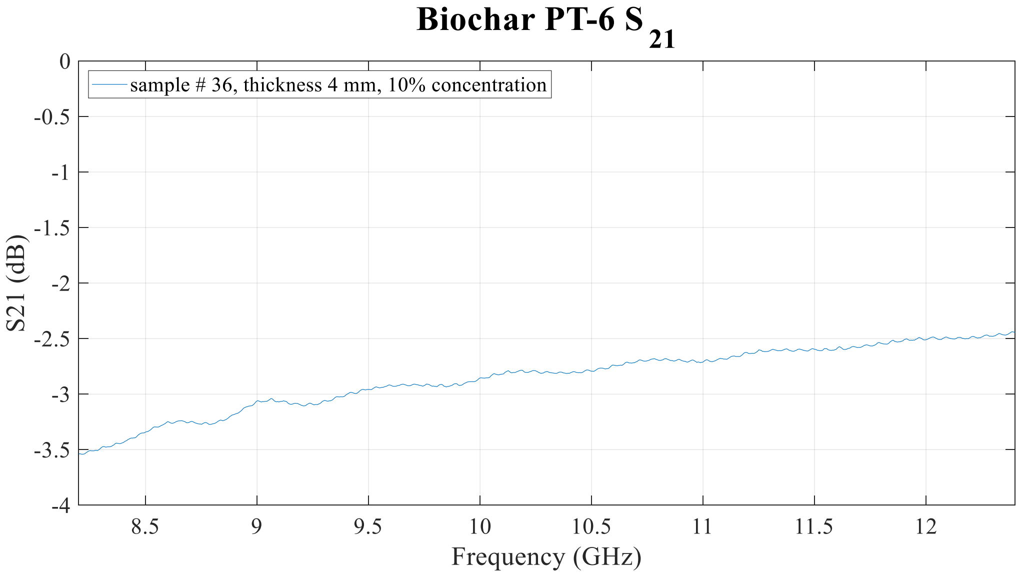

(a)

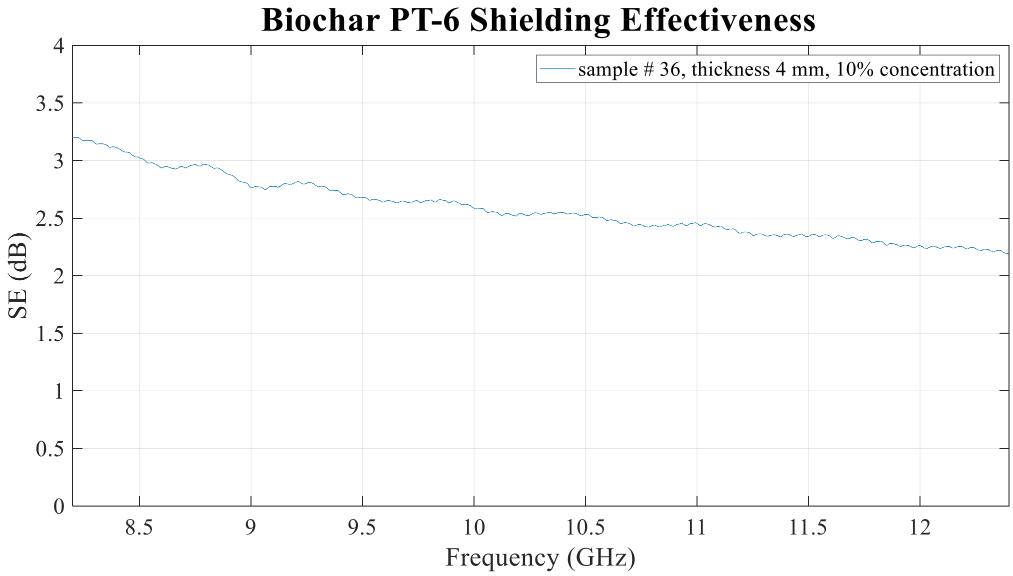

(b)

Figure 4.28: PT-6 biochar S_{21} (a) and shielding effectiveness (b).

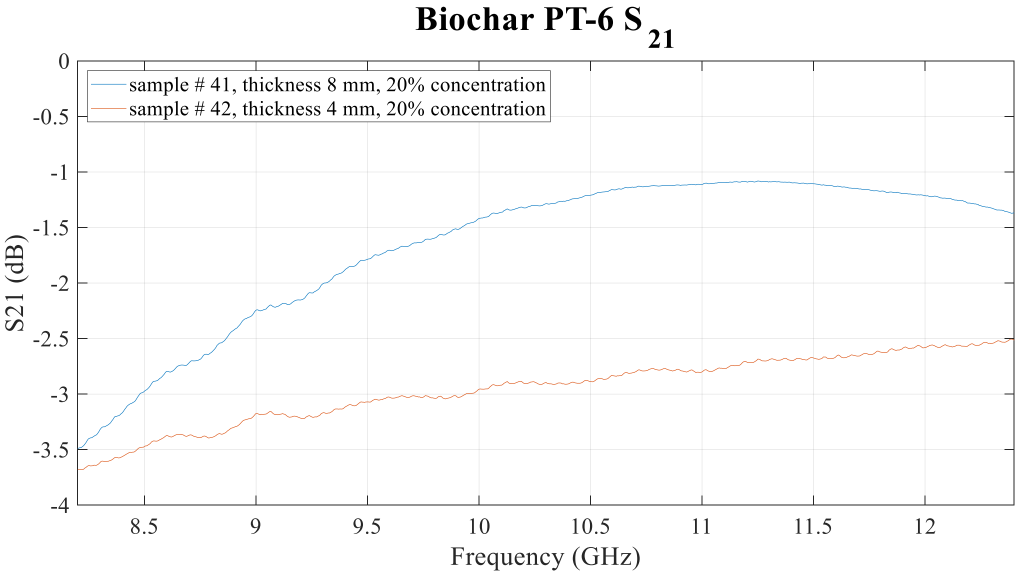

(a)

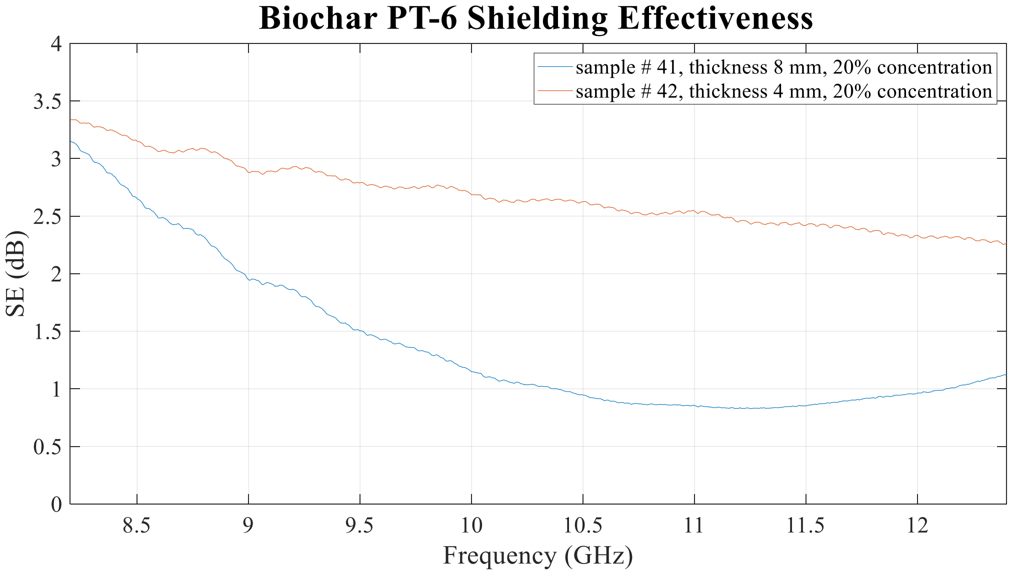

(b)

Figure 4.29: PT-6 biochar S_{21} (a) and shielding effectiveness (b).

A comparison between the used biochar was done for the $4\ \mathrm{mm}$ thick samples only. A pristine sample was compared to the composites obtained with the 10% weight filler in Figure 4.30, while in Figure 4.31 the same sample was compared to the 20% filled composites. As could be noticed, for both concentrations the PT-4 biochar shows the highest shielding effectiveness. Moreover, the composites based on this biochar show an $1\ \mathrm{dB}$ increase in the shielding effectiveness when the filler concentration is doubled. The same increase does not happen for the Bioforcetech and PT-6 biochar, whose shielding effectiveness is almost unchanged. PT-1 biochar shows, in any case, a $0.5\ \mathrm{dB}$ increase in the shielding effectiveness, which is noticeable because it is greater than the measures tolerance.

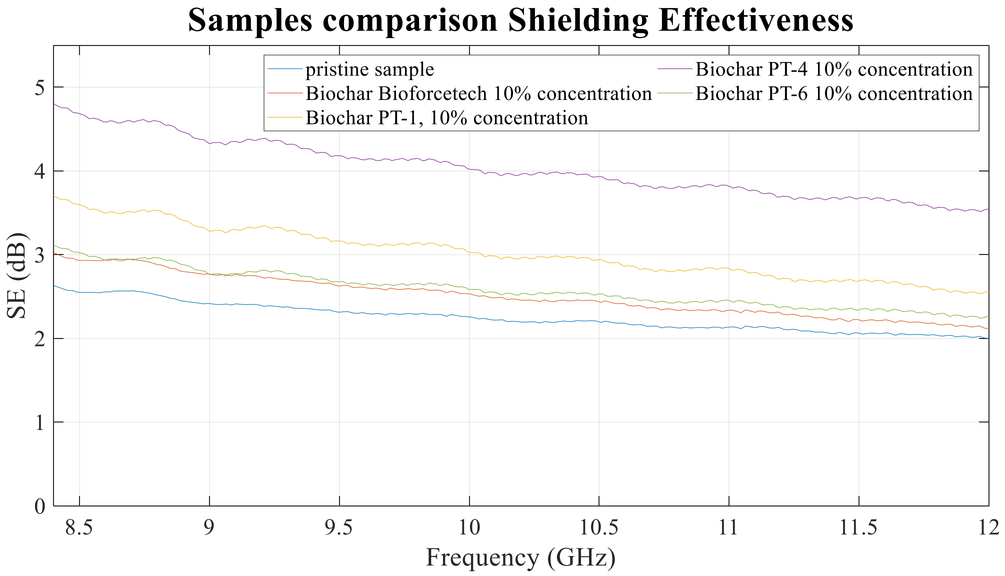

Figure 4.30: A comparison between the biochar used as filler.
The thickness of each specimen is 4 mm.

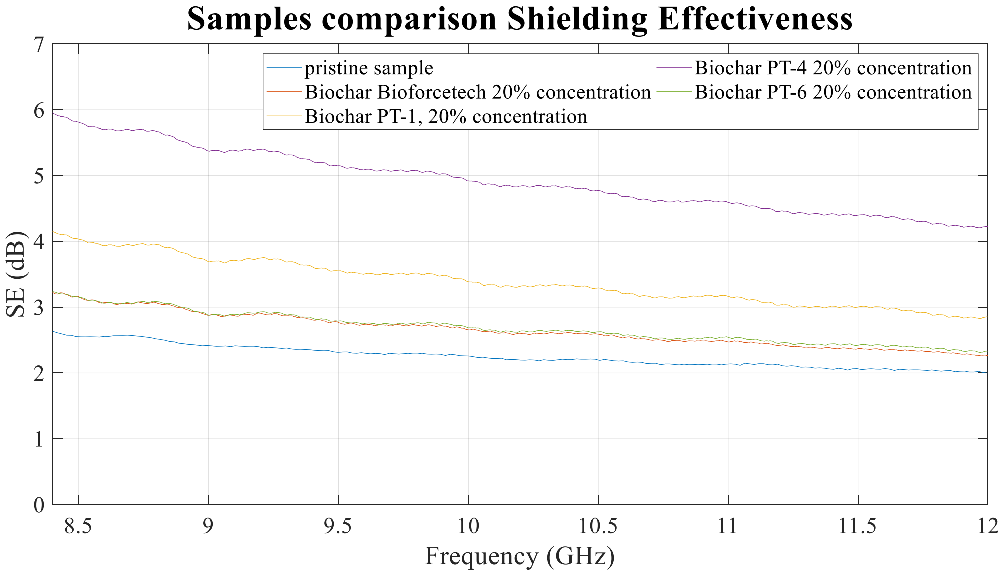

Figure 4.31: A comparison between the biochar used as filler.
The thickness of each specimen is 4 mm.

Composites coating measurements.

The shielding effectiveness of the coated samples and their transmission coefficients are reported in Figure 4.32 (b) and Figure 4.32 (a) respectively. The graph showed in Figure 4.32 (b) is called “Total Shielding effectiveness” because the plotted shielding effectiveness is the result of the epoxy resin insertion loss and the coating composites insertion loss. The shielding effectiveness of the coating only $(\mathrm{SE}_{\mathrm{coating|dB}})$ is computed subtracting the total insertion loss $(\mathrm{SE}_{\mathrm{total|dB}})$, plotted in Figure 4.32 (b), with the pristine sample insertion loss $(\mathrm{SE}_{\mathrm{pristine|dB}})$, measured prior to the coating deposition:

$$SE_{coating|dB} = SE_{total|dB} - SE_{pristine|dB} \tag{4.2}$$

Since, as can be seen from Figure 4.32 (b), the shieliding effectiveness of the polyester resin and the 4% PANI specimens is very similar to the pristine sample specimen (dashed line), the shielding effectiveness of these two samples appears to be slightly negative in the upper part of the measured frequency range. However, the points where the computed shielding effectiveness is negative are acceptable, because they are in the already discussed $0.3\ \mathrm{dB}$ measurement tolerance.

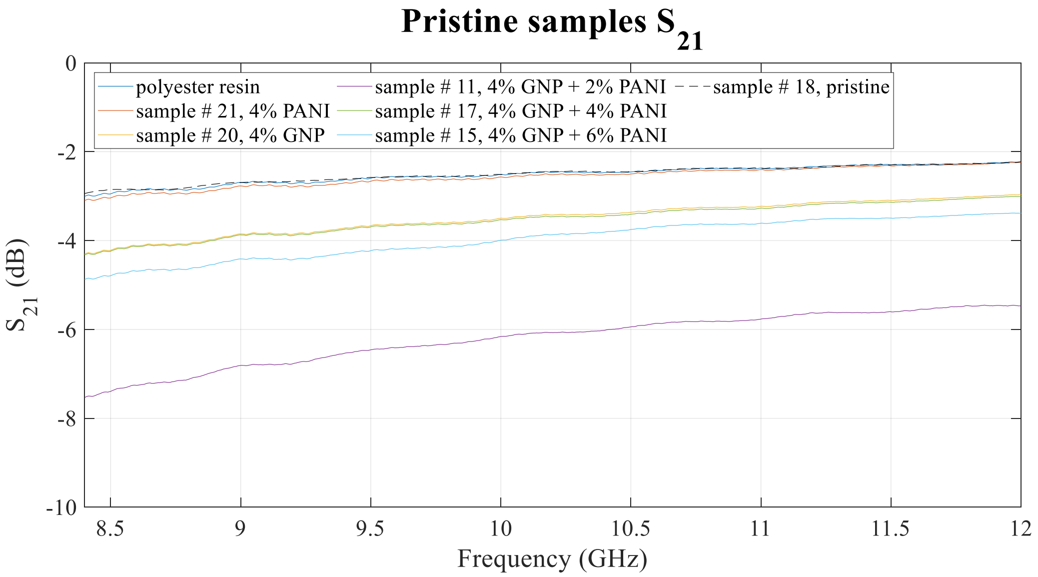

(a)

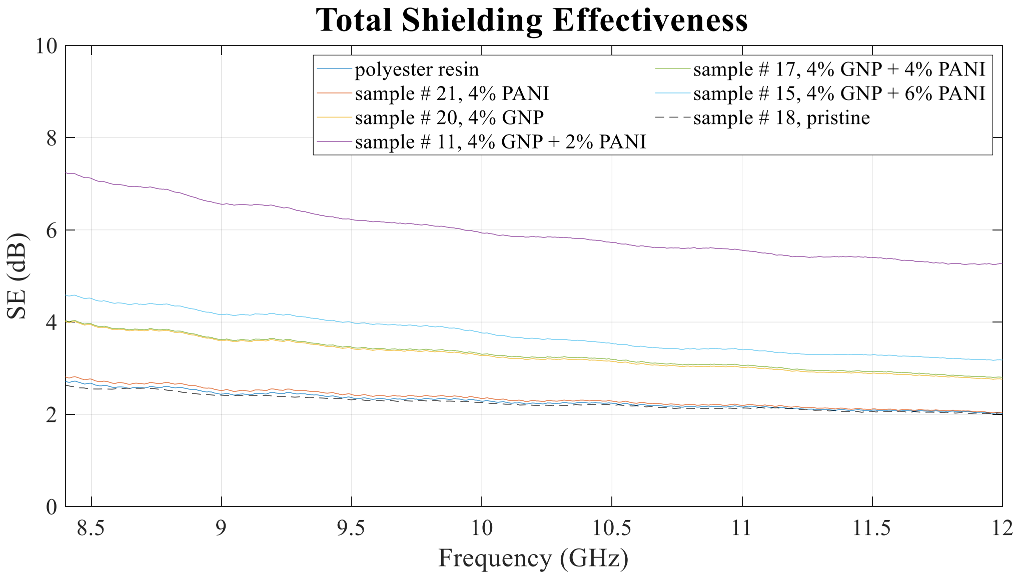

(b)

Figure 4.32: transmission coefficient (a) and shielding effectiveness (b) of the coated samples in Figure 3.12.

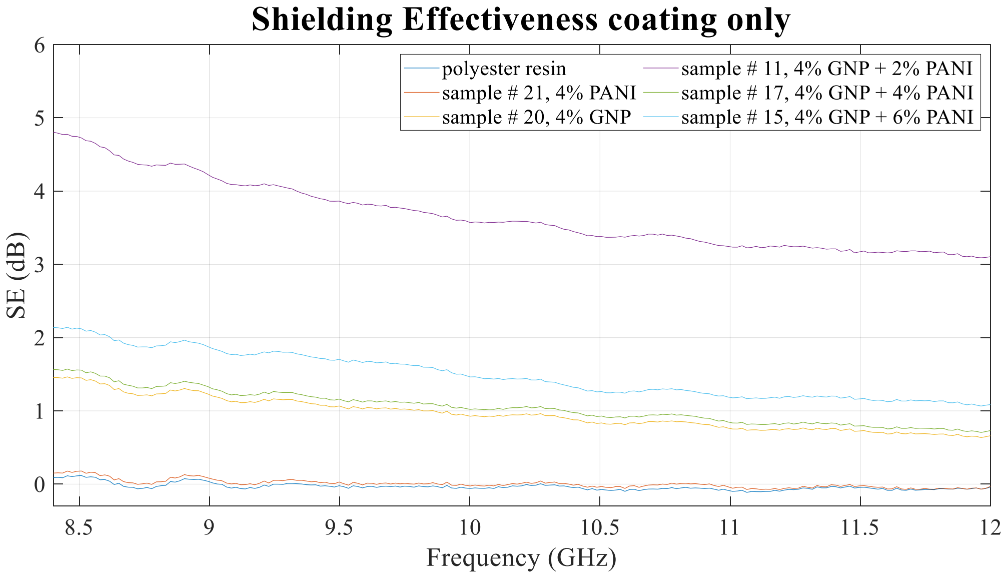

Figure 4.33: The coating only shielding effectiveness, computed according to the equation (4.2).

The graph in Figure 4.33 shows that the polyester resin only exhibits a zero shielding effectiveness, as well as the epoxy resin pristine samples. The low conductivity of the polyaniline (PANI) gives the coated specimen a shielding effectiveness similar to the pristine samples. With regards to the graphene nanoplates (GNP) composites, the shielding effectiveness was expected to increase with increasing the PANI concentration. However, the purple trace in Figure 4.33, which represents the measurements with the lowest PANI concentration, exhibits the highest shielding effectiveness. It could be hence postulated that the lowest the PANI concentration, the highest the shielding effectiveness. Unfortunately, the specimen coated only with the GNP shows a shielding effectiveness lower than all the samples coated with both GNP and PANI. This proves that a combination of PANI and GNP is the best solution for the shielding conductive polymers. Finally, the obvious uncorrelation between the PANI concentration and the shielding effectiveness increase in the 11, 17 and 15 specimens confirms that there is no advantage in increasing the PANI concentration in GNP based composites. From the small number of the tested specimens it must be postulated that there is an optimum combination in the PANI and GNP concentrations to obtain the highest shielding effectiveness in the measured frequency band. On the other hand, as highlighted in the 3.2 subsection, the organic polymers conduction mechanism is more complex than the one of inorganic semiconductors, and is already under investigation [60].

4.3.2 WR137 waveguide measurements

The measurements done with the WR137 calibration kit are reported in this chapter. The composites based on the Afzal's biochar only were measured, because the extensive measurements of the Bioforcetech biochar, made with the WR90 waveguide, showed a low shielding effectiveness value. The coating on the WR137 pristine samples were, instead, unavailable.

Pristine samples

As was done for the WR90 waveguide, the pristine sample insertion loss was evaluated first, to know the contribution of the added fillers in the realized composites. The transmission coefficient and the shielding effectiveness of the epoxy resin specimens are reported in Figure 4.34 (a) and Figure 4.34 (b) respectively. These measurements are in good agreement with the ones obtained with the WR90 waveguide setup, since they differ with only 1 dB. Moreover, no resonance is showed in the measured frequency range by the 8 mm thick samples.

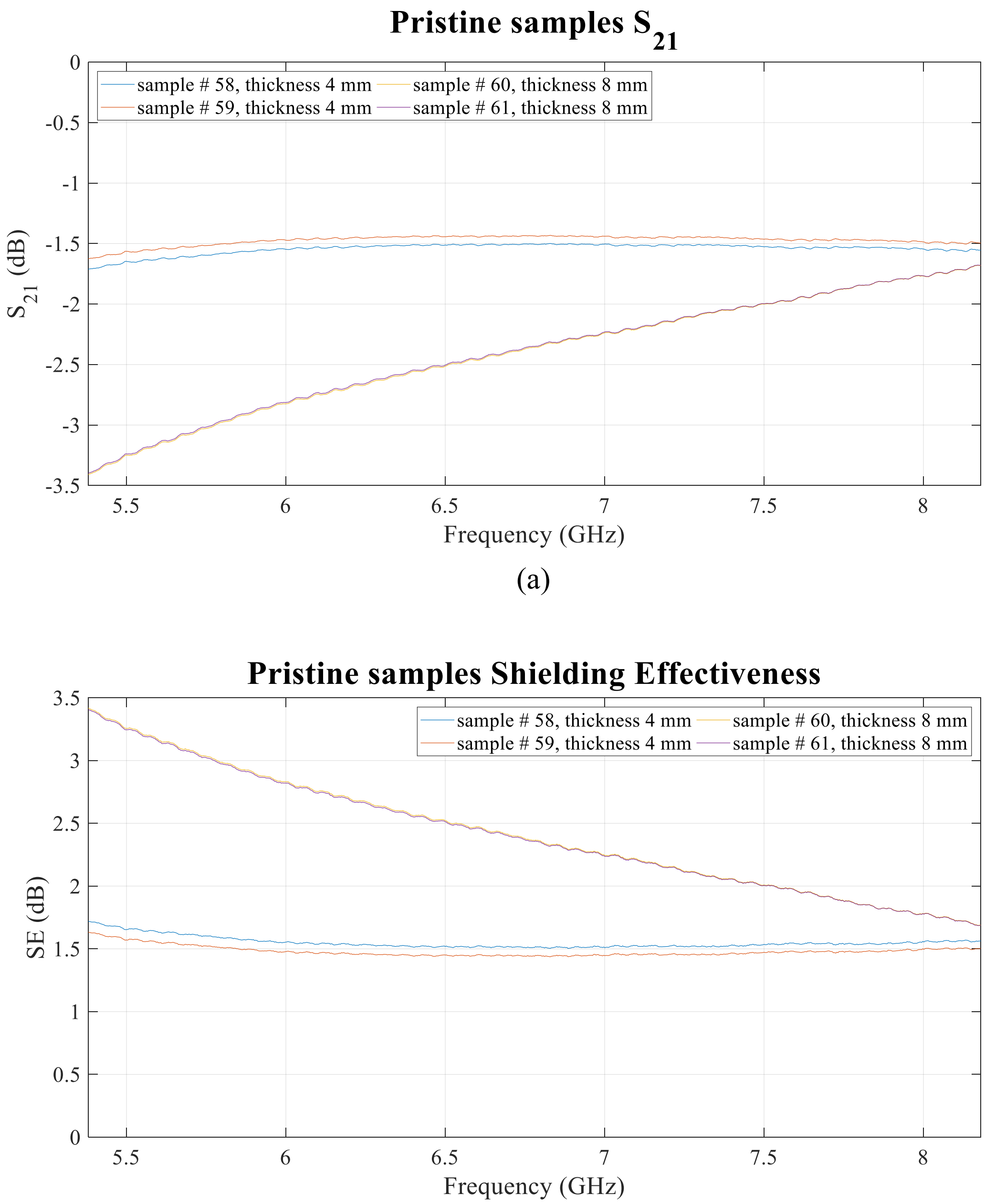

(a)

(b)

Figure 4.34: The pristine samples shielding effectiveness.

Afzal’s biochar composites

For each chosen Afzal’s biochar, a 4 mm and a 8 mm thick sample was realized either with the 10% and 20% filler concentration. The transmission coefficients and the shielding effectiveness of the measured specimens are reported in Figure 4.35 to Figure 4.40 (a) and Figure 4.35 to Figure 4.40 (b) respectively. All the 8 mm thick specimens exhibits an increasing shielding effectiveness. This trend is more regular than the one showed in the X band, because there are no resonances in the reflection coefficient in the C band.

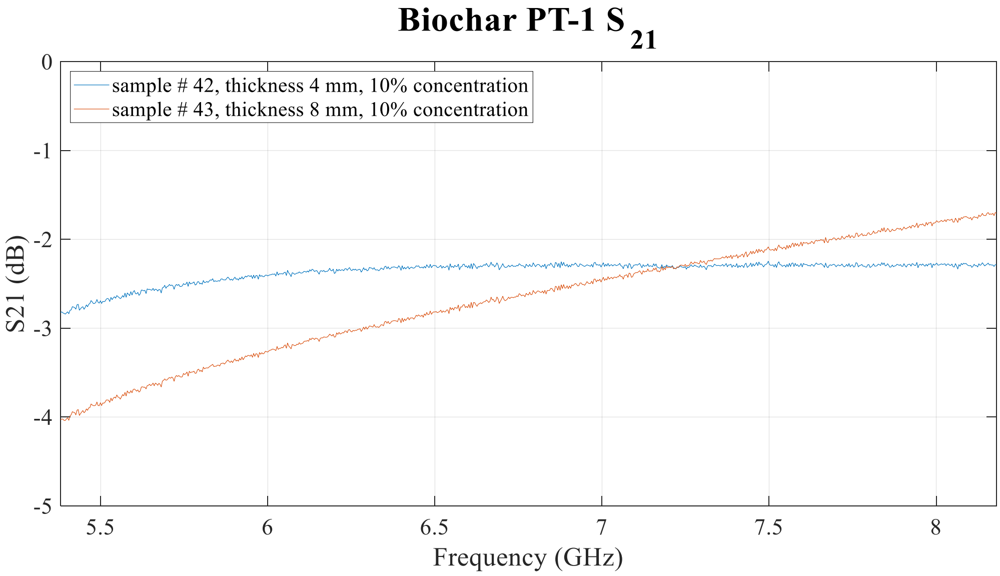

(a)

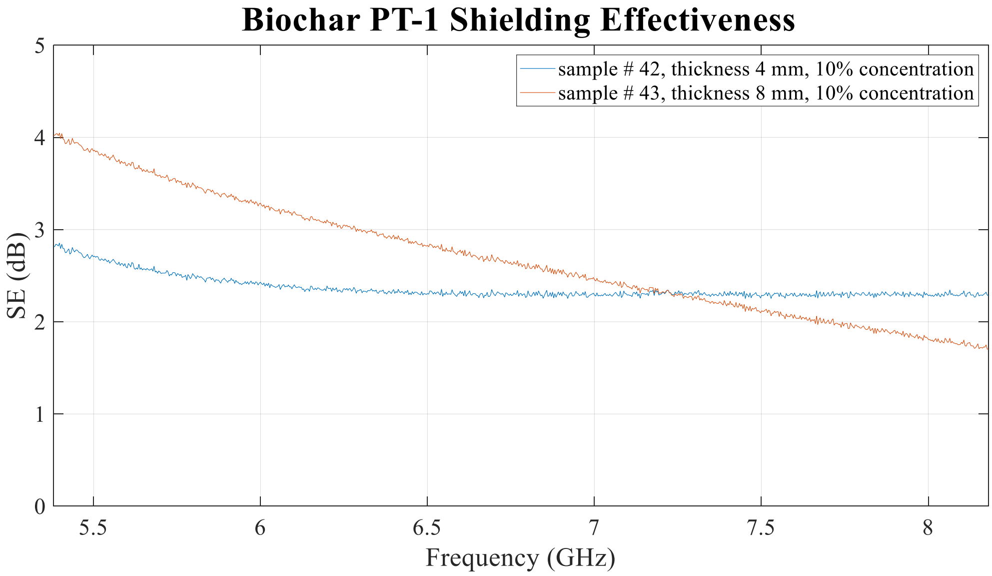

(b)

Figure 4.35: PT-1 composites insertion loss (a) and shielding effectiveness (b).

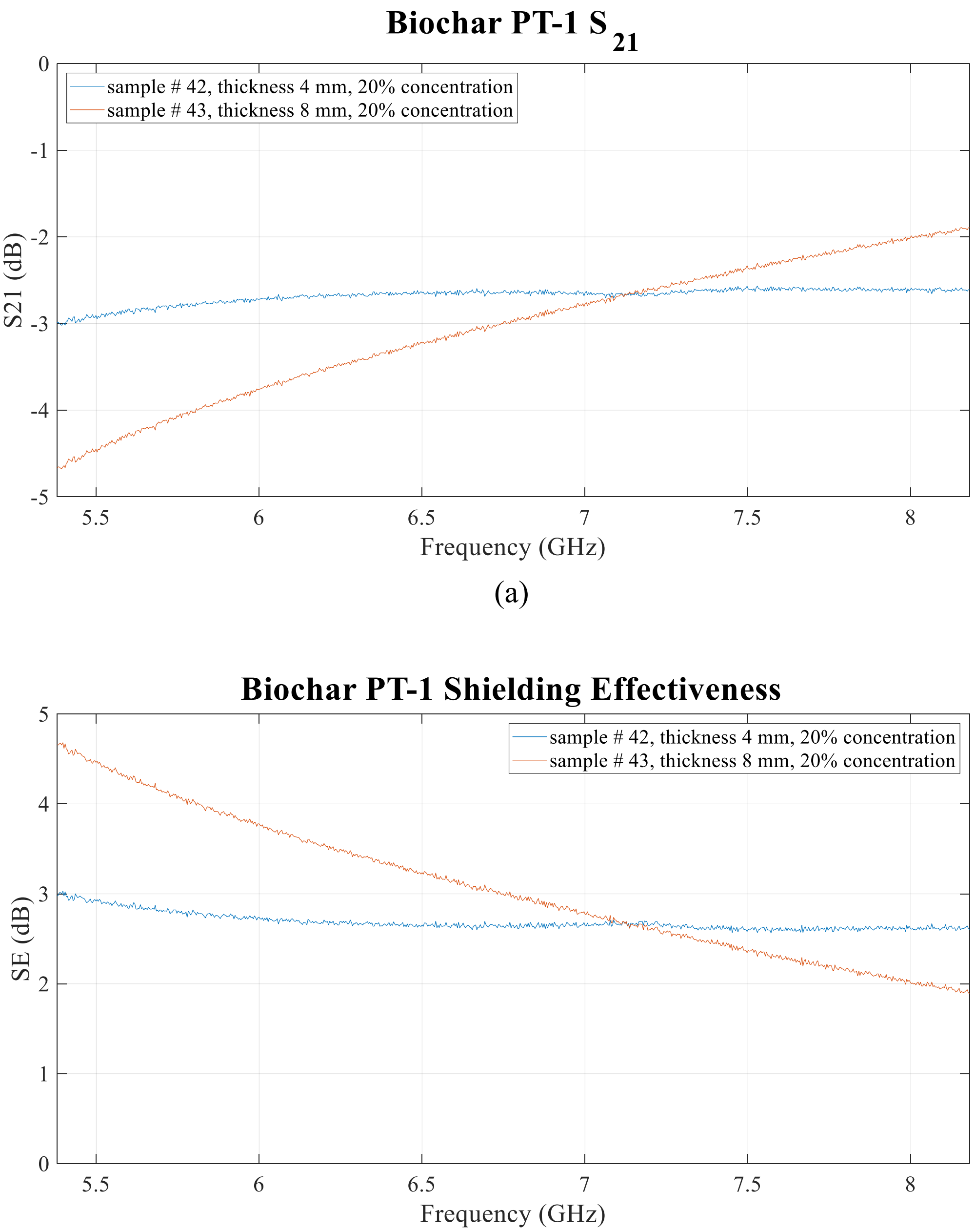

(a)

(b)

Figure 4.36: PT-1 composites insertion loss (a) and shielding effectiveness (b).

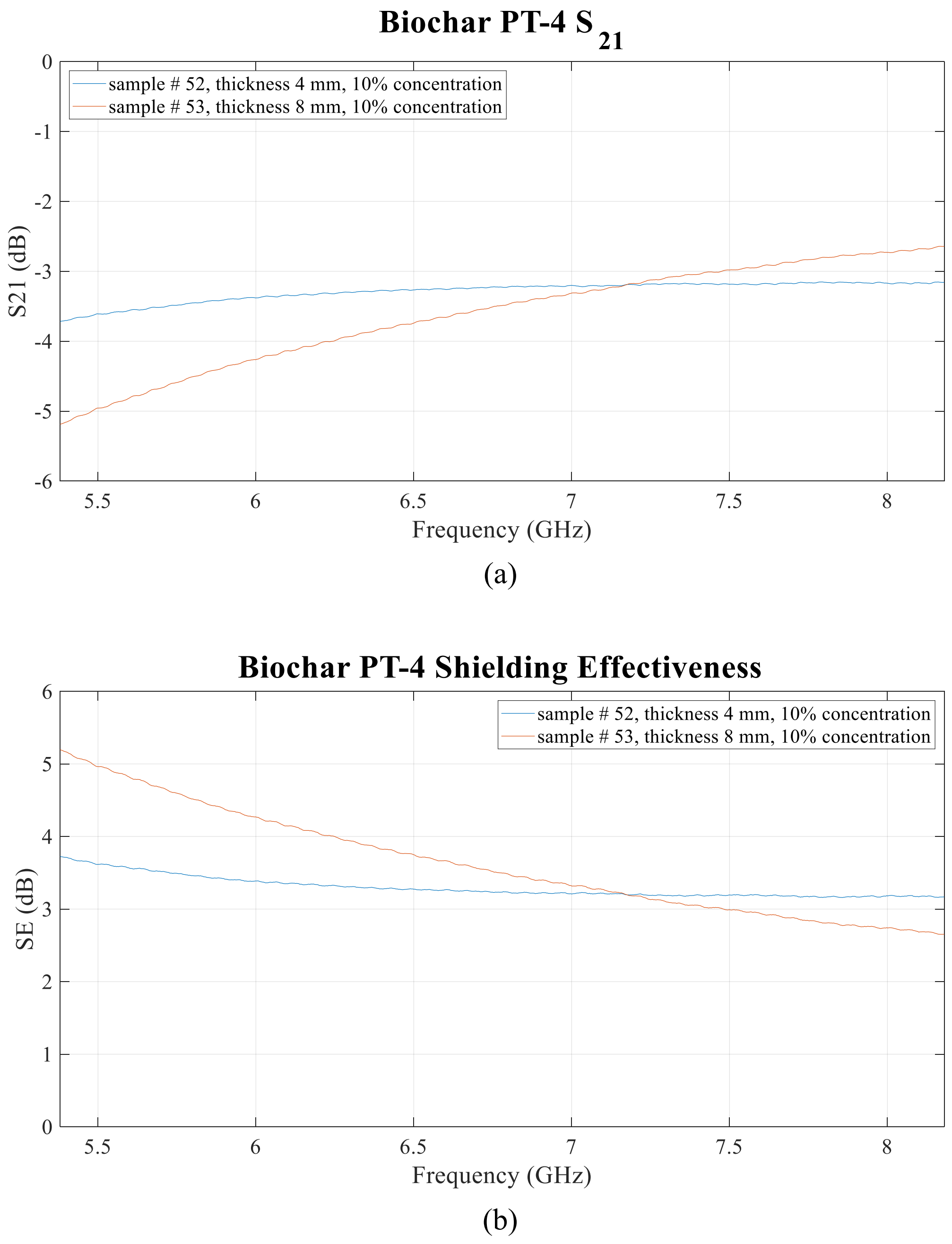

(a)

(b)

Figure 4.37: PT-4 composites insertion loss (a) and shielding effectiveness (b).

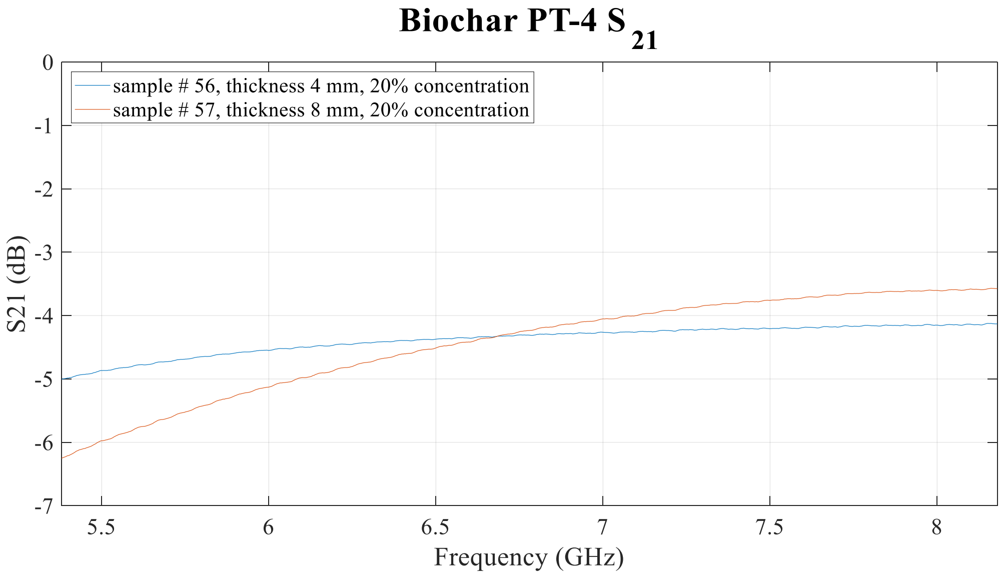

(a)

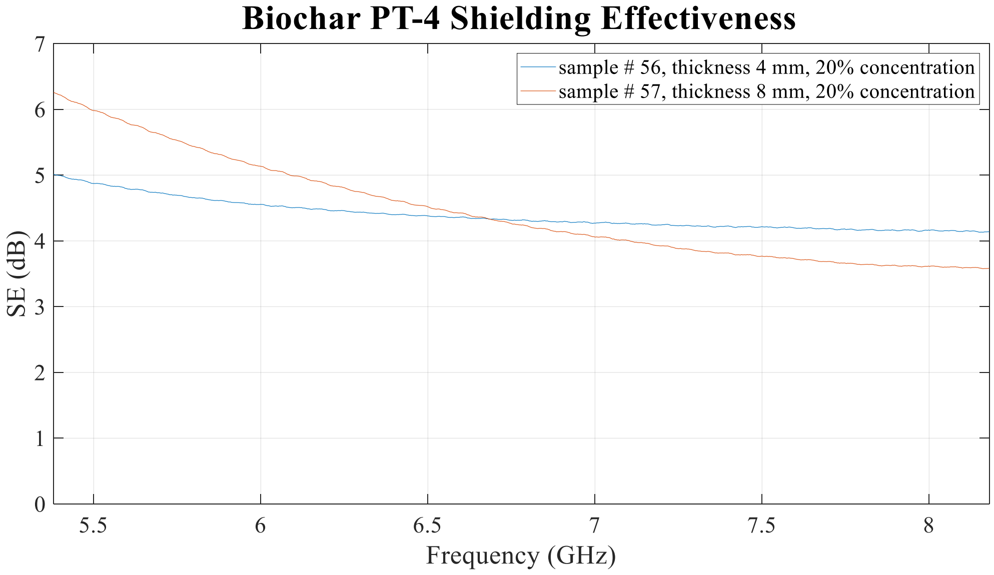

(b)

Figure 4.38: PT-4 composites insertion loss (a) and shielding effectiveness (b).

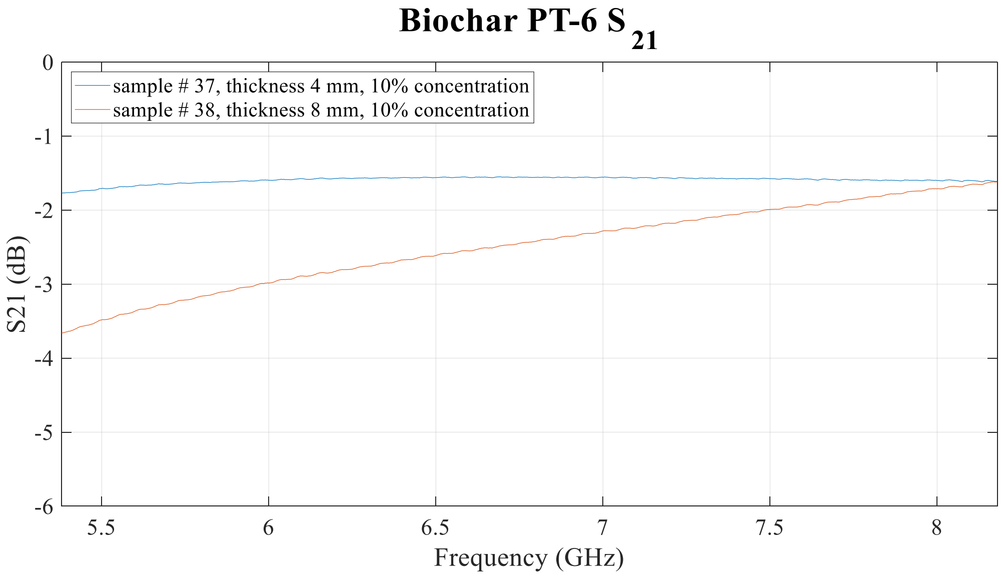

(a)

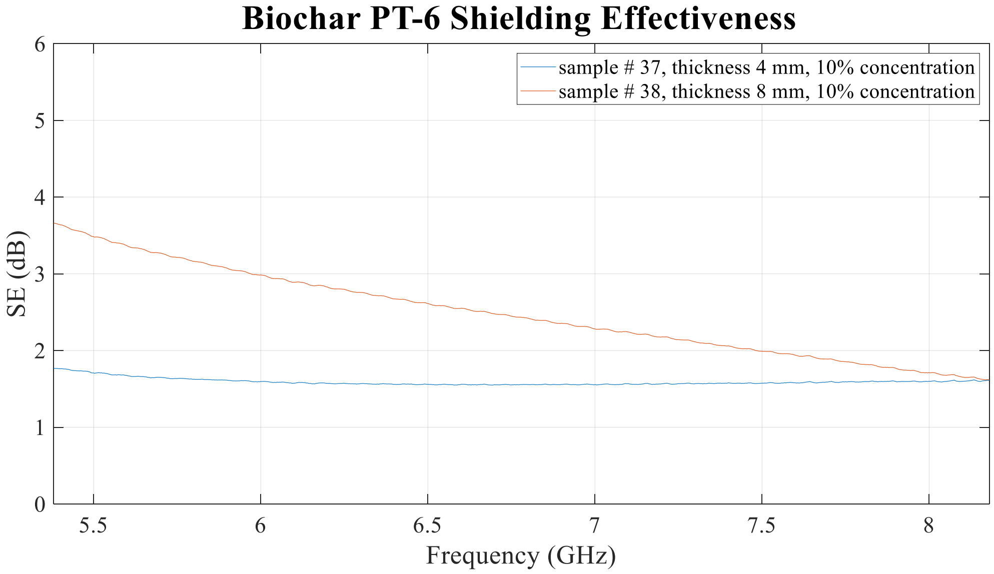

(b)

Figure 4.39: PT-6 composites insertion loss (a) and shielding effectiveness (b).

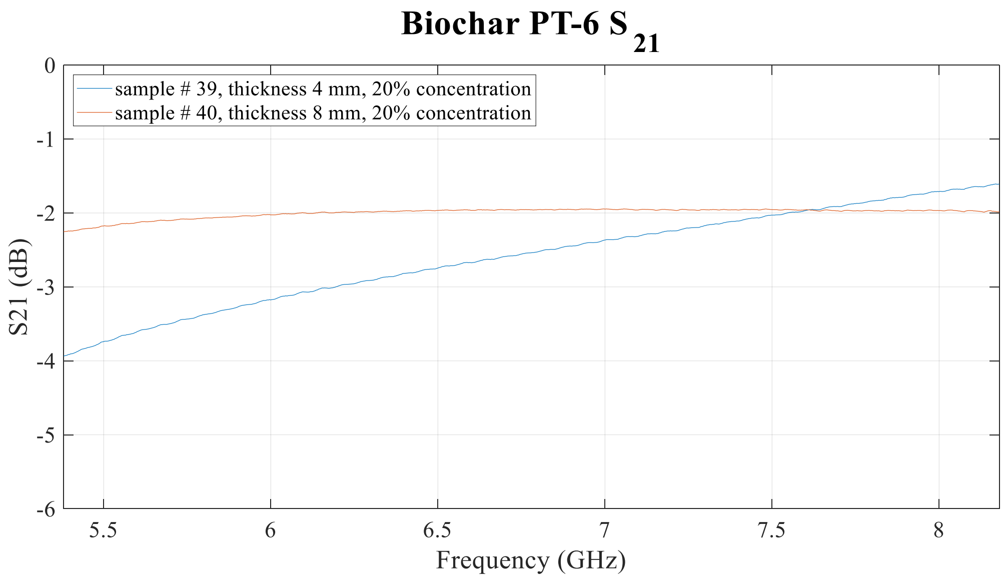

(a)

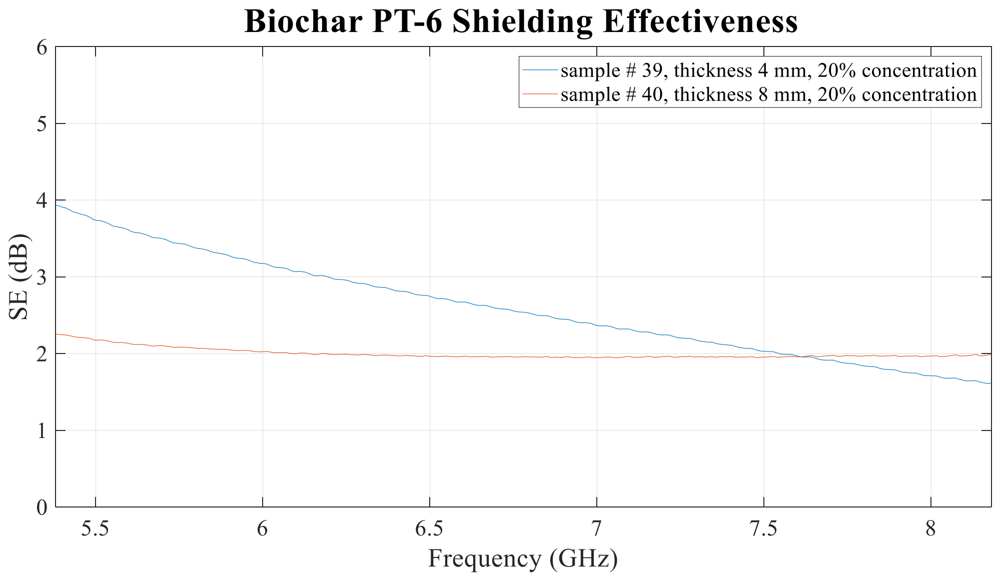

(b)

Figure 4.40: PT-6 composites insertion loss (a) and shielding effectiveness (b).

For each specimen thickness, the effect of the biochar concentration increase is highlighted in Figure 4.41 for the 4 mm thick samples, and in Figure 4.42 for the 8 mm thick specimens. The 4 mm thick samples shows the same increase in the shielding effectiveness measured in the X band. A totally different trend can be observed for the 8 mm thick specimens, whose shielding effectiveness is constantly increasing. The highest measured value is represented by the 20% PT-4 composite, whose shielding effectiveness increases up to $6\ dB$.

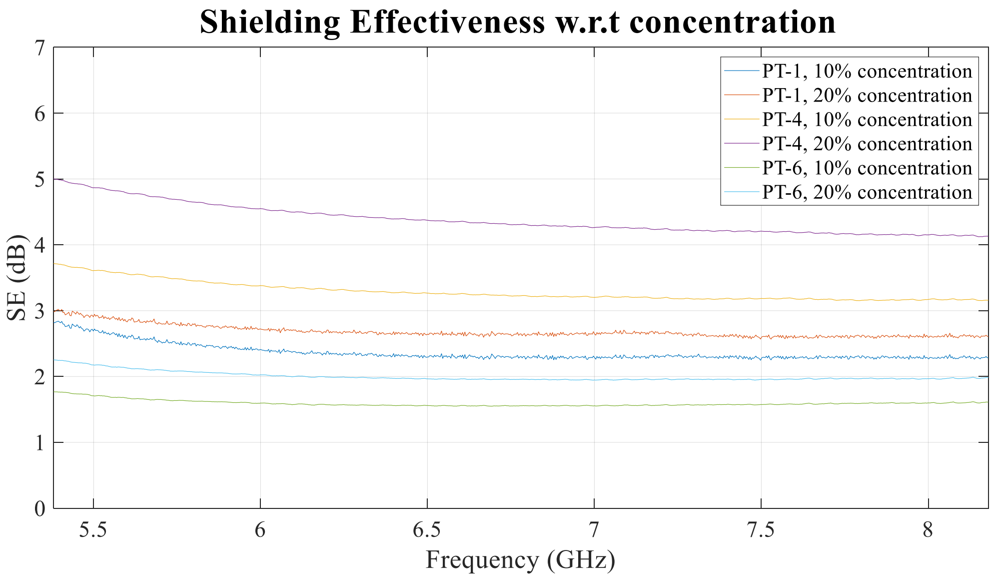

Figure 4.41: The filler concentration effect on the realized 4 mm thick samples.

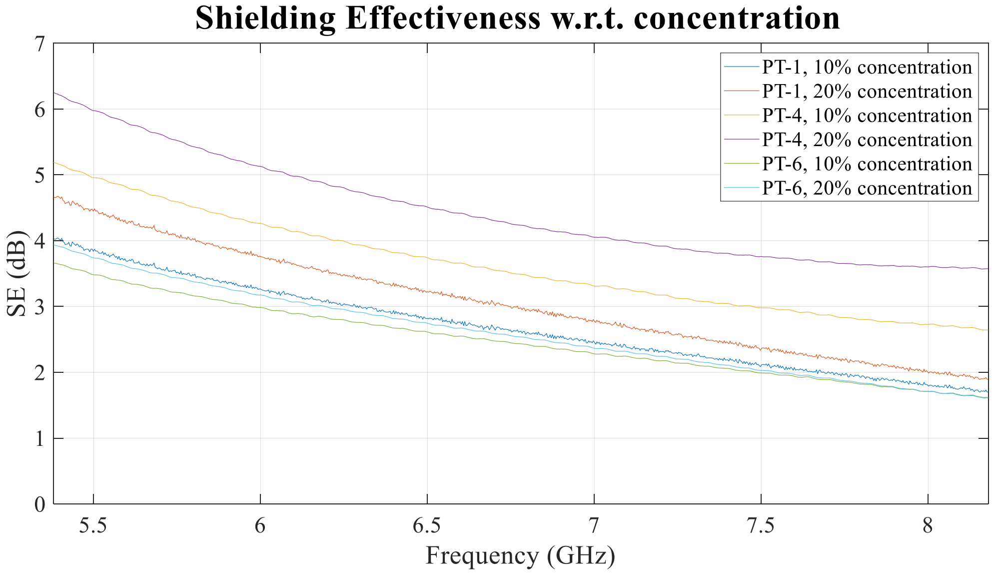

Figure 4.42: The filler concentration effect on the realized 8 mm thick specimens.

The pristine samples and the composites based on the biochar in a 20% concentration were finally compared. In Figure 4.43 the 4 mm thickness specimens were compared, while in Figure 4.44 the 8 mm thick samples measurements are reported. The shielding effectiveness increase of the 4 mm thick samples are the same showed in the X band.

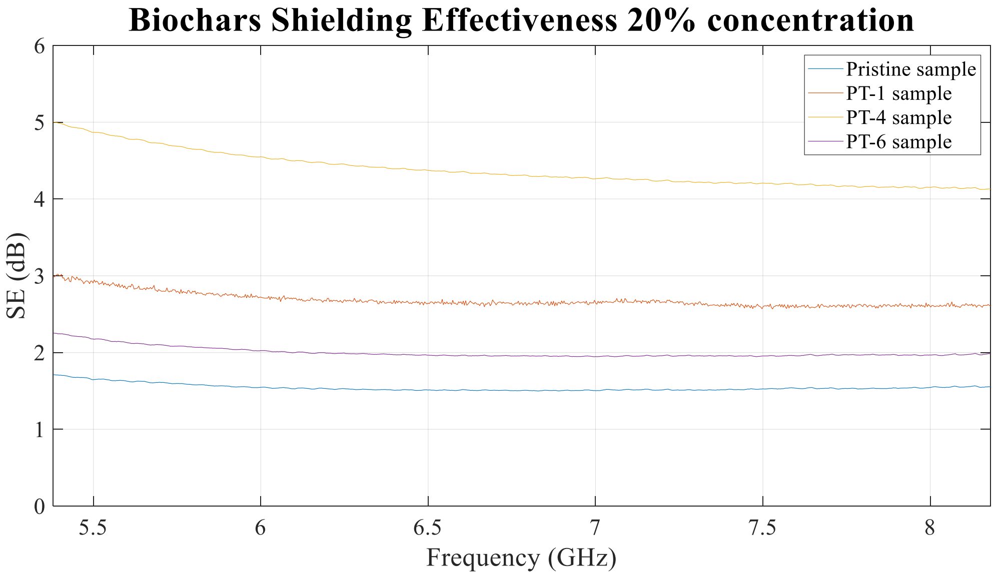

Figure 4.43: Comparison between the pristine sample and the composites specimens having $4\ \mathrm{mm}$ thickness.

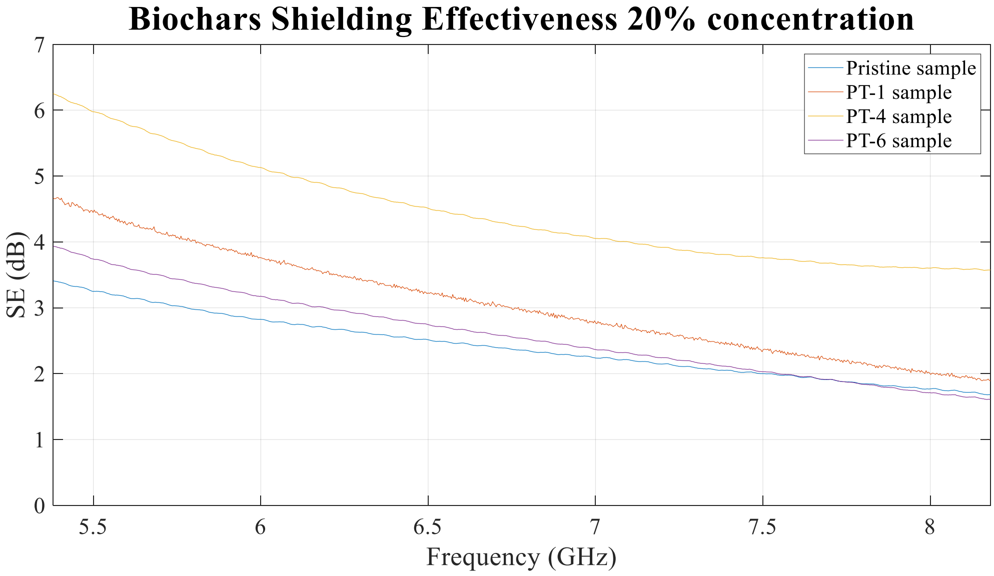

Figure 4.44: Comparison between the pristine sample and the composites specimens having $8\ \mathrm{mm}$ thickness.

Chapter 5

Conclusions

All the shielding effectiveness measurement methods, developed in the last decades, were analyzed in this thesis, in order to choose the best one for the measurement of dielectric composites shielding properties. In a preliminary phase, it was attempted to use an ASTM D4935 coaxial waveguide for the tested composites, but it was found to be unpractical with the deployed epoxy resin. The rectangular waveguide was chosen instead as the test fixture for all the analyzed specimens. They were composites materials based on a commercial epoxy resin, and two novels material, namely biochar-based composites and conductive polymers.

It was developed a procedure for the specimens realization based on:

- A cost-effective process for the samples realization, whose physical dimensions fits the inner walls of the used rectangular waveguides with a 6.6% maximum tolerance;
- A novel method to obtain composites with a homogeneous dispersion, based on a paddle mixer driven by a stepper motor.

The repeatability of the measurements of the pristine samples and of the biochar composites was verified. Moreover, it was confirmed that the setup assembly variations and the specimens physical imperfections does not affects the measurement results.

The low value of the epoxy resin shielding effectiveness (about 3 dB for each band) makes this material useful for the realization of solid supports for composite materials which can be used only to made coatings. Unfortunately, all the tested biochar shows a shielding effectiveness less than 10 dB for both frequency bands. Hence, they cannot be used to obtain epoxy resin based composite materials to be used, instead of metals, to realize efficient electromagnetic shields. The same considerations hold for the conductive polymer composites used to realize shielding coatings.

However, the shielding effectiveness of all the tested materials increases with decreasing frequency: since this trend, verified for the X band, was found to be the same also for the C band, it could be expected a further increase of the shielding effectiveness for frequencies lower than 5.38 GHz. The X band was firstly chosen for the composites testing only because of the availability of a WR90 calibration kit and the possibility to realize small dimensions specimens. This was important in order to reduce the amount of biochar used for each specimen. The developed method for the specimens preparation and shielding effectiveness measurement was found to be easily extendible from the X band to the C bands, hence all the measured materials could be tested in the microwave range for frequencies lower than the lowest measured, namely 5.38 GHz. It is not useful, instead, the testing of the purposed composites for frequencies higher than 12 GHz, which is the maximum frequency for which the showed measurements were carried out. Moreover, in the X band the shielding effectiveness dependence on the sample thickness must be explored, since all the tested materials sowed a resonance peak in this frequency range. About conductive polymers composites, the better GNP to PANI concentration ratio must be already found for the tested frequency bands.

Finally, the rectangular waveguide was found to be an optimum method for the shielding effectiveness measurement of the tested composites. Since the scientific literature shows an increasing interest about biochar and conductive polymers, it could be advisable to find a method to relate the plane wave with the rectangular waveguide field lines distribution. If this will be done, rectangular waveguide measurement method could be standardized, and the measured shielding effectiveness could be compared to the one measured with other methods, such as the ASTM coaxial holder or the reverberation chamber.

Appendix A

Epoxy resin characteristics

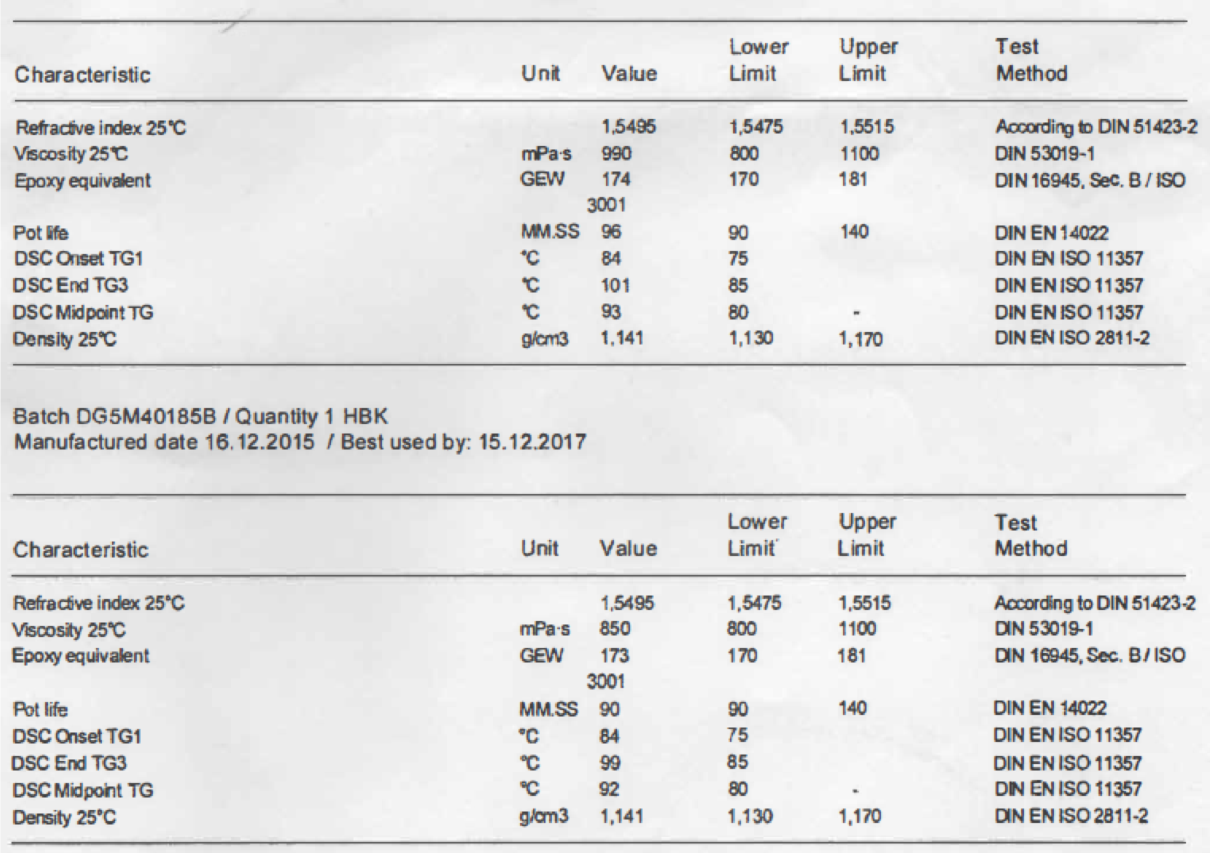

Characteristic	Unit	Value	Lower Limit	Upper Limit	Test Method
Refractive index 25°C		1,5495	1,5475	1,5515	According to DIN 51423-2
Viscosity 25°C	mPa·s	990	800	1100	DIN 53019-1
Epoxy equivalent	GEW	174	170	181	DIN 16945, Sec. B / ISO
		3001			
Pot life	MM.SS	96	90	140	DIN EN 14022
DSC Onset TG1	°C	84	75		DIN EN ISO 11357
DSC End TG3	°C	101	85		DIN EN ISO 11357
DSC Midpoint TG	°C	93	80	-	DIN EN ISO 11357
Density 25°C	g/cm3	1,141	1,130	1,170	DIN EN ISO 2811-2

Batch DG5M40185B / Quantity 1 HBK
Manufactured date 16.12.2015 / Best used by: 15.12.2017

Characteristic	Unit	Value	Lower Limit	Upper Limit	Test Method
Refractive index 25°C		1,5495	1,5475	1,5515	According to DIN 51423-2
Viscosity 25°C	mPa·s	850	800	1100	DIN 53019-1
Epoxy equivalent	GEW	173	170	181	DIN 16945, Sec. B / ISO
		3001			
Pot life	MM.SS	90	90	140	DIN EN 14022
DSC Onset TG1	°C	84	75		DIN EN ISO 11357
DSC End TG3	°C	99	85		DIN EN ISO 11357
DSC Midpoint TG	°C	92	80	-	DIN EN ISO 11357
Density 25°C	g/cm3	1,141	1,130	1,170	DIN EN ISO 2811-2

Figure 5.1: Hexion resin RIMR 135 physical characteristics [52].

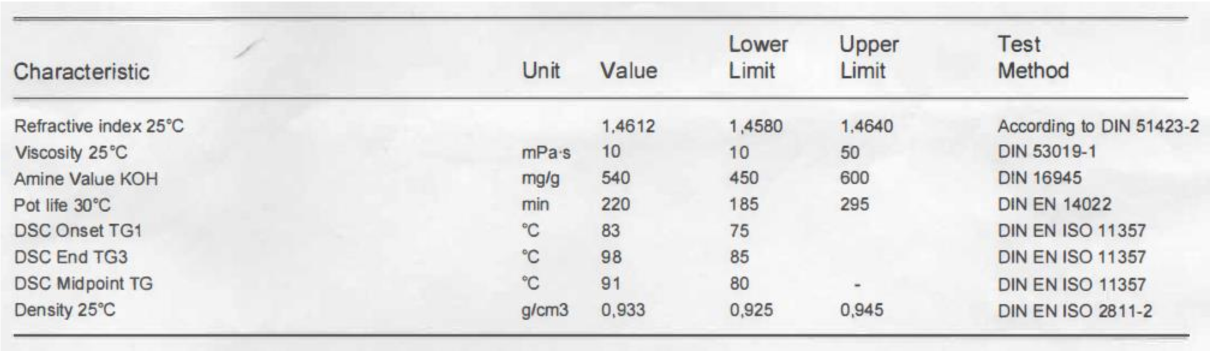

Characteristic	Unit	Value	Lower Limit	Upper Limit	Test Method
Refractive index 25°C		1,4612	1,4580	1,4640	According to DIN 51423-2
Viscosity 25°C	mPa·s	10	10	50	DIN 53019-1
Amine Value KOH	mg/g	540	450	600	DIN 16945
Pot life 30°C	min	220	185	295	DIN EN 14022
DSC Onset TG1	°C	83	75		DIN EN ISO 11357
DSC End TG3	°C	98	85		DIN EN ISO 11357
DSC Midpoint TG	°C	91	80	-	DIN EN ISO 11357
Density 25°C	g/cm3	0,933	0,925	0,945	DIN EN ISO 2811-2

Figure 5.2: Hexion curing RIMH 137 physical characteristics [52].

References

[1] C. R. Paul, Introduction to electromagnetic compatibility, second ed., Wiley, 2008.

[2] F. Canavero, "Lectures of the course Advanced Design for Signal Integrity and Compliance: Lecture 7: Shielding".

[3] P. Wilson, T. A. Mark and J. W. Adams, "Techniques for measuring the electromagnetic shielding efectiveness of materials: Part I: - Far field source simulation," *IEEE transactions on electromagnetic compatibility ,* vol. 30, no. 3, pp. 239-250, 1988.

[4] P. F. Wilson and M. T. Ma, "Techniques for measuring the electromagnetic shielding efectiveness of materials: Part II: - Near field source simulation," *IEEE transactions on electromagnetic compatibility,* vol. 30, no. 3, pp. 251-259, 1988.

[5] A. Tamburrano, D. Desideri and A. Maschio, "Coaxial waveguide methods for shielding effectiveness measurement of planar materials up to 18 GHz," *IEEE transactions on electromagnetic compatibility,* vol. 56, no. 6, pp. 1386-1396, 2014.

[6] J. Carlsson, K. Karlsson and A. Johansson, "Validation of shielding effectiveness measurement method using nested reverberation chambers by comparison with aperture theory," in *International Symposium on Electromagnetic Compatibility - EMC EUROPE*, Rome, 2012.

[7] F. B. Leferink, H. Bergsma and W. C. v. Etten, "Shielding Effectiveness measurements using a reverberation chamber," in *International Zurich Symposium on Electromagnetic Compatibility*, Singapore, 2006.

[8] C. L. Holloway, D. A. Hill, J. Ladbury, G. Koepke and R. Garzia, "Shielding effectiveness measurements of materials using nested reverberation chambers," *IEEE transactions on electromagnetic compatibility,* vol. 45, no. 2, pp. 350-357, 2003.

[9] M. Hatfield, "Shielding effectiveness measurements using mode-stirred chambers: A comparison of two approaches," *IEEE transactions on electromagnetic compatibility,* vol. 30, no. 3, pp. 229-238, 1988.

[10] C. L. Holloway, J. Ladbury, J. Coder, G. Koepke and D. Hill, "Measuring the Shielding Effectiveness of small enclosures/cavities with a reverberation chamber," in *IEEE International Symposium on Electromagnetic Compatibility*, Honolulu, 2007.

[11] IEEE Standard Method for Measuring the Effectiveness of Electromagnetic Shielding Enclosures, IEEE, 2007.

[12] IEEE Standard Method for Measuring the Shielding Effectiveness of Enclosures and Boxes Having all Dimensions between 0.1 m and 2 m, IEEE, 2013.

[13] D. Senić and A. Šarolić, "Shielding effectiveness measurements in resonant enclosure based on loaded reverberation chamber in a GTEM cell," in *International Symposium on Electromagnetic Compatibility - EMC EUROPE*, Rome. Italy, 2012.

[14] R. De Leo, T. Rozzi, C. Svara and L. Zappelli, "Rigorous analysis of the GTEM cell," *IEEE transactions on microwave theory and techniques,* vol. 39, no. 3, pp. 488-491, 1991.

[15] D. Senić, A. Šarolić and V. Roje, "GTEM cell setup and method for measuring shielding effectiveness of resonant enclosures," in *Proc. of the 10th Int. Symposium on Electromagnetic Compatibility*, York, 2011.

[16] D. K. W. Jin, T. Y. K. Roland and N. Y. Seng, "Shielding effectiveness measurement conducted in a reverberation chamber and in a GTEM cell," in *International Zurich Symposium on Electromagnetic Compatibility*, Singapore, 2008.

[17] P. Wilson, J. Adams and M. Ma, "Measurement of the electromagnetic shielding capabilities of matherials," *Proceedings of the IEEE,* vol. 74, no. 1, pp. 112-115, 1986.

[18] A. International, "www.astm.org," Copyright © 1996 - 2019. [Online]. Available: https://www.astm.org/DATABASE.CART/WITHDRAWN/ES7.htm. [Accessed 12 03 2019].

[19] Y. K. Hong, C. Y. Lee, C. K. Jeong, D. E. Lee, K. Kim and J. Joo, "Method and apparatus to measure electromagnetic interference shielding efficiency and its shielding characteristics in broadband frequency ranges," *Review of Scientific Instruments,* vol. 74, no. 2, pp. 1098-1103, 2003.

[20] A. D4935-18, "Standard Test Method for Measuring the Electromagnetic Shielding Effectiveness of Planar Materials," *American Society for Testing and Materials,* 2018.

[21] electro-metrix, "electro-metrix.com," Capital District Digital , 2019. [Online]. Available: https://electro-metrics.com/product/shielding-effectiveness-conductivity-test-em-2107a-30-mhz-1-5-ghz/. [Accessed 13 03 2019].

[22] M. Badic and M. J. Marinescu, "The failure of coaxial TEM cells ASTM standards methods in H.F. range," in *IEEE international symposium on electromagnetic compatibility*, Minneapolis, 2002.

[23] M. S. Sarto and A. Tamburrano, "Innovative test method for the shielding effectiveness measurement of conductive thin films in a wide frequency range," *IEEE transactions on electromagnetic compatibility,* vol. 48, no. 2, pp. 331-342, 2006.

[24] C. Chen, F. Lu, Yu-Sang and Quing-Cai, "A compensated flanged coaxial tester for shielding effectiveness measurement," in *International Conference on Microwave and Millimeter Wave Technology (ICMMT)*, Shenzhen, China, 2012.

[25] S. Greco, A. D. Tamburrano, R. Mufatti and M. Sarto, "Shielding effectiveness properties of carbon-fiber reinforced composite for HIRF applications," in *International Symposium on Electromagnetic Compatibility - EMC EUROPE*, Rome, Italy, 2012.

[26] R. Valente, C. De Ruijter, D. Vlasveld, S. Van der zwaaag and P. Groen, "Setup for EMI shielding effectiveness tests of electrically conductive polymer composites at frequencies up to 3.0 GHz," *IEEE Access ,* vol. 5, pp. 16665 - 16675, 2017.

[27] N. N. HOANG, J.-L. MIANE and J.-L. WOJKIEWICZ, "Modeling of electromagnetic shielding effectiveness of multilayer conducting composites in the microwave band," in *First International Conference on Communications and Electronics*, Hanoi, 2006.

[28] J. Lee, B. M. Jung, S. B. Lee, S.-K. Lee and K. H. Kim, "FeCoNi-coated glass fabric/polycarbonate composite sheets for electromagnetic absorption and shielding," in *IEEE International Magnetics Conference (INTERMAG)*, Dublin, Ireland, 2017.

[29] A. Mehdipour, I. D. Rosca, C. W. Trueman, A. R. Sebak and S. V. Hoa, "Multiwall carbon nanotube–epoxy composites with high shielding effectiveness for aeronautic applications," *IEEE transactions on electromagnetic comaptibility,* vol. 54, no. 1, pp. 28-37, 2012.

[30] A. Ferraro, Enciclopedia della radio, Vols. primo, A-L, Bari: Sansoni Edizioni Scientifiche, 1954, p. 670.

[31] W. Chen, Z. Zhang, Z. Feng, Y. Chen, K. Jiang, S. Fan and M. Iskander, "Measurement of polarized nano-material (PNM) for microwave applications," in *IEEE MTT-S International Microwave Symposium Digest*, Atlanta, 2008.

[32] S. P. Rea, D. Wylie, D. Linton, E. Om and J. n. McConnell, "EM1 Shielding of Woven Carbon Fibre Composites," in *High Frequency Postgraduate Student Colloquium*, Manchester, 2004.

[33] R. K. Challa, D. Kajfez, V. Demir, J. R. Gladden and E. A. Z., "Characterization of Multiwalled Carbon Nanotube (MWCNT) composites in a waveguide of square cross section," *IEEE microwave and wireless componentrs letters,* vol. 18, no. 3, pp. 161-164, 2008.

[34] P. F. Wilson and T. M. Ma, A study of techniques for measuring the electromagnetic shielding effectiveness of matherials, Boulder: NBS publications, 1986.

[35] A. C. Marvin, L. Dawson, I. D. Flintoft and J. F. Dawson, "A method for the measurement of shielding effectiveness of planar samples requiring no sample edge preparation or contact," *IEEE transactions on electromagnetic compatibility,* vol. 51, no. 2, pp. 255-263, 2009.

[36] D. Micheli, C. Apollo, R. Pastore, D. Barbera, R. B. Ram´on Bueno Morles, M. Marchetti, G. Gradoni, V. M. Primiani and F. Moglie, "Optimization of multilayer shields made of composite nanostructured materials," *IEEE transactions on electromagnetic compatibility,* vol. 54, no. 1, pp. 60-70, 2012.

[37] S. L. Parker, A. C. Marvin, J. F. Dawson and M. Ye, "Measurement of transmission through printed circuit boards: application to enclosure shielding," in *International Symposium on Electromagnetic Compatibility*, Angers, France, 2017.

[38] B. D. Cordill, S. A. Seguin and M. S. Ewing, "Shielding effectiveness of carbon–fiber composite aircraft using large cavity theory," *IEEE transactions on instrumentation and measurement,* vol. 62, no. 4, pp. 743-752, 2013.

[39] B. D. Cordill, S. A. Seguin and M. S. Ewing, "Shielding effectiveness of composite and aluminum aircraft, model and measurement comparison," in *IEEE International Instrumentation and Measurement Technology Conference*, Binjiang, China, 2011.

[40] R. T. Johnk, D. R. Novotny, C. A. Grosvenor, N. Canales, Camell, D. G., G. H. Koepke and R. C. Scully, "RF electromagnetic penetration of the NASA Space Shuttle endeavour performed with an ultra-wideband system," in *IEEE international symposium on electromagnetic compatibility*, Honolulu, 2007.

[41] J. Xue, X. Yin, F. Ye, L. Zhang and L. Cheng, "Theoretical prediction and experimental verification on EMI shielding effectiveness of dielectric composites using complex permittivity," *Ceramics International, ELSEVIER,* vol. 43, no. 18, pp. 16736-16743, 2017.

[42] G. Andrieu, J. Panh, A. Reineix, P. Pelissou, C. Girard, X. Romeuf and D. Schmitt, "Low-frequency characterization of composite panels from a near-field magnetic shielding effectiveness measurement," in *IEEE International Symposium on Electromagnetic Compatibility*, Long Beach, 2011.

[43] J. Ronal Moser, "Low-frequency shielding of a circular loop electromagnetic field source," *IEEE transactions on electromagnetic compatibility,* vol. 9, no. 1, pp. 6-18, 1967.

[44] J. A. Catrysse, G. M. and W. Steenbakkers, "Correlation between shielding effectiveness measurements and alternative methods for the characterization of shielding materials," *IEEE transactions on electromagnetic compatibility,* vol. 34, no. 4, pp. 440-444, 1993.

[45] F. Benyoubi, M. Feliachi, M. Bensetti, Y. Le Bihan and L. Pichon, "Fast evaluation of low frequency near field magnetic shielding effectiveness," in *IEEE International Symposium on Electromagnetic Compatibility and IEEE Asia-Pacific Symposium on Electromagnetic Compatibility (EMC/APEMC)*, Singapore, Singapore, 2018.

[46] C. Iftode and S. Miclaus, "Design and validation of a TEM cell used for radiofrequency dosimetric studies," *Progress In Electromagnetics Research,* vol. 132, p. 369–388, 2012.

[47] A. Manara, "Measurement of material shielding effectiveness using a dual TEM cell and vector network analvzer," *IEEE transactions on electromagnetic compatibility,* vol. 38, no. 3, pp. 327-334, 1996.

[48] V. Voicu, I. Patru, L.-A. Dina, P.-M. Nicolae and I. D. Sm□r□ndescu, "Shielding Effectiveness evaluation using a non-standardized method," in *International Conference on Electromechanical and Power Systems*, Iasi, 2017.

[49] M. Pocai, I. Dotto and D. Festa, "Three methods for measuring the shielding effectiveness of shielding materials: a comparidson," in *IEEE International Symposium on Electromagnetic Compatibility*, Pittsburgh, 2012.

[50] H. Jang, J. Lim, Y. Lee, H. Lee and W. Nah, "Electric and magnetic field shielding evaluation of board level shield can using TEM cell," in *IEEE Electrical Design of Advanced Packaging and Systems Symposium (EDAPS)*, Seoul, 2015.

[51] N. Modarelli, Advisors:, P. Gronchi, P. Savi and M. Goisis, Electrically conductive coatings for electromagnetic shielding applications, Milano, Italy, 2019.

[52] Hexion, "www.hexion.com," [Online]. Available: https://www.hexion.com/index.html. [Accessed 02 04 2019].

[53] A. I. Biochar, "www.ichar.org," Ichar, [Online]. Available: https://www.ichar.org/content.php?page=136. [Accessed 1 04 2019].

[54] D. Nhuchhen, M. Afzal, T. Dreise and A. Salema, "Characteristics of biochar and bio-oil produced from wood pellets pyrolysis using a bench scale fixed bed, microwave reactor," *Biomass and Bioenergy,* vol. 119, pp. 292-303, 2018.

[55] P. Savi, M. Giorcelli and A. Bayat, "Microwave characterization and shielding properties of biochar based polymers and cements," in *ECI Conference*, 2017.

[56] L. Suiyi, H. An, G. Yann-Jiun, L. Dagang and T. Lih-Sheng, "Highly filled biochar/ultra-high molecular weight polyethylene/linear low density polyethylene composites for high-performance electromagnetic interference shielding," *Composites Part B,* vol. 153, p. 277–284, 2018.

[57] "www.bioforcetech.com," Bioforcetech Corporation , [Online]. Available: http://www.bioforcetech.com/it/. [Accessed 01 04 2019].

[58] Fluke, 8845A/8846A digital multimeter, Fluke Corporation , 2006.

[59] T.-H. Le, Y. Kim and H. Yoon, "Electrical and Electrochemical Properties of Conducting Polymers," *Polymers,* p. 32, 23 April 2017.

[60] X. Xia, A. D. Mazzeo, Z. Zhong and G. J. Weng, "An X-band theory of electromagnetic interference shielding for graphene-polymer nanocomposites," *Journal of applied physics,* p. 12, 2017.

[61] Motorola, Low noise transistors, BC559, B, C, BC560C, 1996.

[62] G. Nico, Il manuale dell'IC 555, Verdellino(BG): Sandit, 2005.

[63] O. Semiconductor, MJE350 Plastic Medium Power PNP Silicon Transistor, 2007.

[64] N. Semiconductor, LM3914 Dot/Bar Display Driver, 2000.

[65] M. McComb, "Introduction to Stepper Motors, part 2," *Microchip WebSeminars,* 2007.

[66] Agilent Technologies, Agilent PNA Microwave Network Analyzers Data Sheet, USA, 2009.

[67] J. P. Dunsmore, Handbook of microwave component measurements, New Delhi, India: Wiley, 2012.

[68] M. M. Corporation, Waveguide calibration kit WR90 8.2 to 12.4 GHz Model X7005E(), 2008.

[69] J. Baker-Jarvis and M. D. Janezic, "Analysis of a two-port flanged coaxial holder for shielding effectiveness and dielectric measurements of thin films and thin materials," *IEEE transactions on electromagnetic compatibility,* vol. 38, no. 1, pp. 67-70, 1996.

[70] A. Tamburrano and M. Sarto, "Electromagnetic characterization of innovative shielding materials in the frequency range up to 8 gigahertz," in *International symposium on electromagnetic compatibility*, Silicon Valley, 2004.

[71] H. N. Nhan, M. Jean-Louis and W. Jean-Luc, "Modeling of Electromagnetic Shielding Effectiveness of Multilayer Conducting Composites in the Microwave Band," in *First International Conference on Communications and Electronics*, Hanoi, 2006.

[72] R. B. Schulz, V. C. Plantz and D. R. Brush, "Shielding theory and practice," *IEEE transactions on electromagnetic compatibility,* vol. 30, no. 3, pp. 187-201, 1988.

[73] J. Catrysse, "A new test cell for the characterisation of shielding materials in the far field," 1990.

[74] J. A. Catrysse, "Measuring thechniques for SE-values of samples and enclosures," 1992.

[75] J. A. Catrysse, M. Delesie and W. Steenbakkers, "The influence of text fixture on Shielding Effectiveness measurements," *IEEE transactions on electromagnetic compatibility,* vol. 34, no. 3, pp. 348-351, 1992.

[76] X. Huang, T. Leng, J. C. Chen, K. H. Chang and Z. Hu, "Shielding effectiveness of screen printed graphene laminate at C band," in *10th European Conference on Antennas and Propagation (EuCAP)*, Davos, 2016.

[77] B. Foulonneau, F. Gaudaire and Y. Gabillet, "Measurement method of electromagnetic transmission loss of building components using two reverberation chambers," *ELECTRONICS LETTERS,* vol. 32, no. 23, pp. 2130-2131, 1996.

[78] 3. Systems, multiJet plastic printers, 3D Systems Corporation, 2018.